THREE DIMENSIONAL SEISMIC IMAGING OF THE COSTA RICA ACCRETIONARY MARGIN

APPROVED:

Supervisor: [redacted]

Dr. Paul L. Stoffa

[redacted]

Dr. Thomas H. Shipley

[redacted]

Dr. Stephen P. Grand

THREE DIMENSIONAL SEISMIC IMAGING OF THE COSTA RICA ACCRETIONARY MARGIN

by

WALTER PAUL KESSINGER, B.S.

THESIS

Presented to the Faculty of the Graduate School of

The University of Texas at Austin

in Partial Fulfillment

of the Requirements

for the Degree of

MASTERS OF ARTS

THE UNIVERSITY OF TEXAS AT AUSTIN

May 1991

TABLE OF CONTENTS

LIST OF TABLES

LIST OF FIGURES

Chapter 1: Introduction

This thesis is a study of the imaging potential of the 3-D seismic data collected by the University of Texas Institute for Geophysics over the convergent margin of Costa Rica. It presents a partial documentation of both the data acquisition and processing, with an emphasis on three of the operations included in the processing sequence: navigation reduction, common midpoint binning, and poststack migration. As its focus, this thesis studies how measurement uncertainties, sampling limitations, and algorithm inaccuracies limited the spatial resolution achieved during processing of the 3-D Costa Rica data.

Convergent plate margins are the sites of some of the earth's most active geodynamic processes. As a by-product of subduction tectonics, massive sedimentary units are often built at these margins by the transfer of material from the subducting plate to the overriding plate. These accumulations are known as accretionary wedges or accretionary prisms.

Various active margin tectonic processes are known to contribute to the development of accretionary wedges. Likewise, a multitude of geological and geophysical parameters determine the manner in which these processes interact. This complicated interplay of factors has made it difficult to identify what circumstances will result in a particular style of accretion. To evaluate the contribution of various processes, better definition is needed of structures within modern accretionary prisms.

Worldwide, studies of modern accretionary complexes underscore that accretionary prisms exhibit complex structures at all scales. Beneath the Barbados Ridge complex, sediment subduction can be followed for at least 70 kilometers (Westbrook et al., 1988). Core samples from drilling of the lower slope of the Mid-America trench off Guatemala have revealed evidence of down-slope transportation of large blocks, as well as showing microfractured rocks at much smaller scales (von Huene et al., 1980). Offshore Mexico, Sea Beam studies of the toe of the trench have shown a dramatic variety of structural styles within that area (Moore and Shipley, 1988).

Modern prisms provide convergent margin scientists with laboratories in which they can make direct observations of accretionary wedge activities. In discussing the results of submarine outcrop measurements of the Oregon accretionary prism, however, J. C. Moore et al. (1990) stressed the necessity of integrating their results with detailed seismic reflection studies. Reflection seismic experiments are necessary in these environments because of their unique ability to densely sample the acoustic properties of the earth's crust. Other geophysical measurements that probe the properties of the solid earth do not provide the spatial resolution necessary for defining deep structures at scales of tens, hundreds and even thousands of meters. Similarly, direct sampling of sediments at outcrops and by deep sea drilling does not provide an adequate sampling density to unambiguously define structural relationships within accretionary prisms.

Despite the advantage in spatial sampling, seismic studies of accretionary prisms have had problems providing adequate definition of prism structures. The following examples are representative of problems that are often cited in the literature:

(1) In seismic studies of the Barbados Ridge (Westbrook et al., 1988) and the Nankai Trough (G. F. Moore et al., 1990), degradation of the quality of the seismic image was attributed to the occurrence of structures beneath the resolution of seismic data. (2) Scattering of the seismic signal was blamed for poor seismic images within the accretionary wedge offshore Mexico (Moore and Shipley, 1988), as well as in the Nankai Trough (G. F. Moore et al., 1990). In the case of the Nankai Trough study, it was noted that the amplitude of the signal transmitted through the wedge was strong, but few coherent reflectors could be imaged. (3) Von Huene et al. (1980) showed that incorrect seismic interpretations of structures off Guatemala were directly attributable to the use of widely spaced acquisition lines in the interpretations.

A solution to the first problem listed above would require the acquisition of higher frequency, more finely sampled data. Within the limits of present acquisition technology, this probably cannot be done in a cost-effective manner. The second and third problems are also sampling problems, but they are more directly attributable to the absence of three dimensional data coverage. As this thesis demonstrates, with 3-D coverage, the quality of the seismic image can frequently be greatly improved by proper data processing. Past seismic studies of accretionary margins have greatly influenced current models of subduction tectonics. Given a better seismic image of accretionary prisms, geologic interpretations of these environments will be further improved.

Requirements for Accurate Imaging and Interpretation

Convergent margins present structurally complex areas in which seismic imaging is a critical challenge. Competing models of offscraping and underplating predict different subsurface structures; because the structure and stratigraphy are mirrored in the seismic record, seismic data should provide the means for distinguishing among models. Unfortunately these predicted differences are sometimes subtle, necessitating excellent image quality and high spatial resolution (Coltrin et al. 1989).

This thesis is concerned with the process of imaging the three dimensional multichannel seismic data that were collected over the accretionary wedge offshore the Nicoya Peninsula of Costa Rica (Figure 1). This same area was the focus of several past seismic surveys (Shipley et al., 1979; Shipley and Moore, 1986; Moore and Shipley, 1988). In studies of data from earlier surveys, internal structures were identified within the wedge but imaging was poor; the same seismic data have been used by different authors to support conflicting interpretations (e.g., Shipley and Buffler, 1987; Silver et al., 1985). Better imaging of the accretionary prism was needed, not only to elucidate the relative importance of mechanisms which have contributed to its construction, but simply to achieve a coherent geometrical representation of the structure, so interpretation could proceed on a sound basis.

The object of the survey described here was to collect seismic data which would precisely define the internal structure of the Costa Rican accretionary wedge. In many accretionary environments, including the offshore Nicoya Peninsula area, seismic reflection studies have had difficulties revealing coherent reflections except at

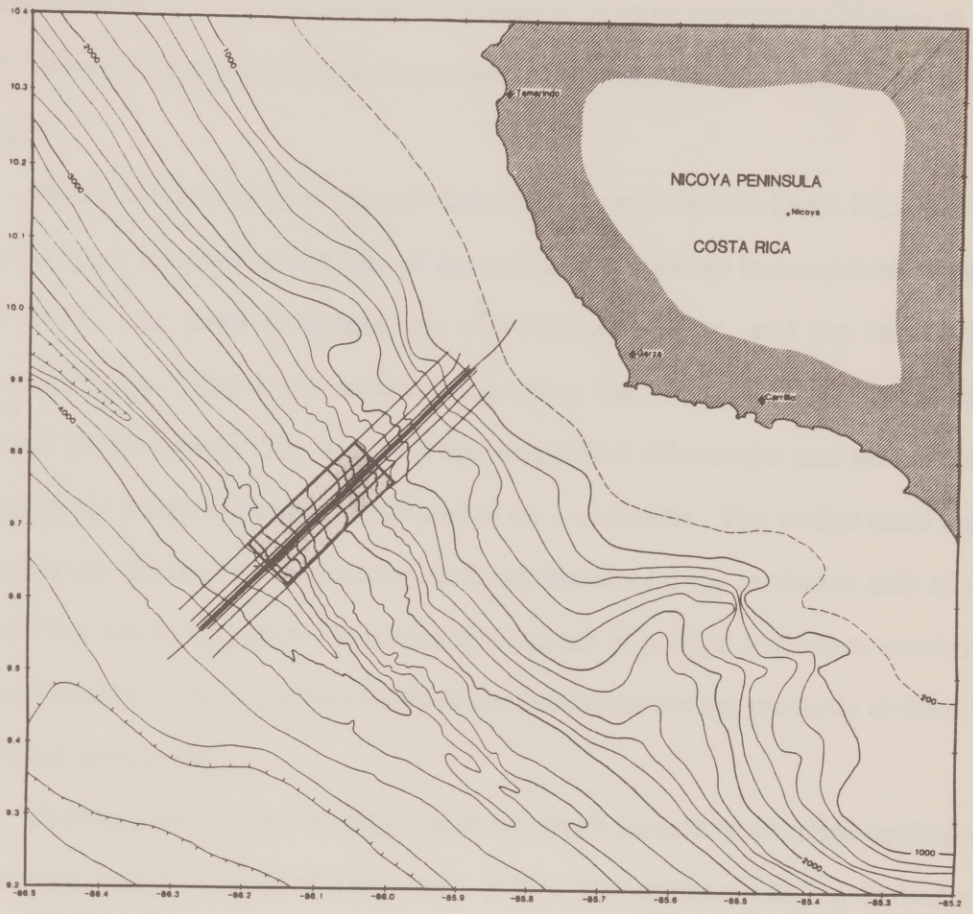

Figure 1. Map showing the location of the 3-D grid survey (stippled box) offshore Costa Rica and the 9 swath lines. The three Maxiran base stations are shown at Tamarindo, Garza, and Carrillo.

the toe of the wedge. Within the wedge, this is partially due to the inclusion of structures whose scales are below the threshold of seismic resolution (Shipley et al., 1990). Another important factor, however, is the three dimensional nature of the geology.

Figure 2 shows stacked seismic data from the most recent Costa Rica survey. The subsurface structure in the area of the accretionary wedge is composed of three major units: the slope sediment, the accretionary wedge, and the underlying subducting plate. The slope sediment covering the wedge attains a maximum thickness in the survey area of about one and a half kilometers and pinches out approximately seven kilometers landward of the trench axis. The wedge itself has a maximum thickness of approximately three kilometers on the landward side of the survey. The subducting plate contains a thin veneer of pelagic sediments overlying oceanic basement. The interfaces between the three units are not precisely defined by the stacked seismic data.

Imaging problems are mainly due to the rough surface at the slope sediment / accretionary wedge interface (Coltrin et al., 1989). This surface is highly faulted and reflector dips commonly exceed 30°. The inherent roughness of this surface is extensive in both the dip and strike directions. A highly accurate migration algorithm is needed to properly image the steep dips and fault truncations of this irregular surface.

Lateral and vertical velocity variations further complicate the migration problem. Seismic velocities range from less than 2 km/sec in the slope sediments to greater than 3 km/sec in the directly adjacent wedge material. The velocity contrast across this interface distorts the seismic wavefield during propagation.

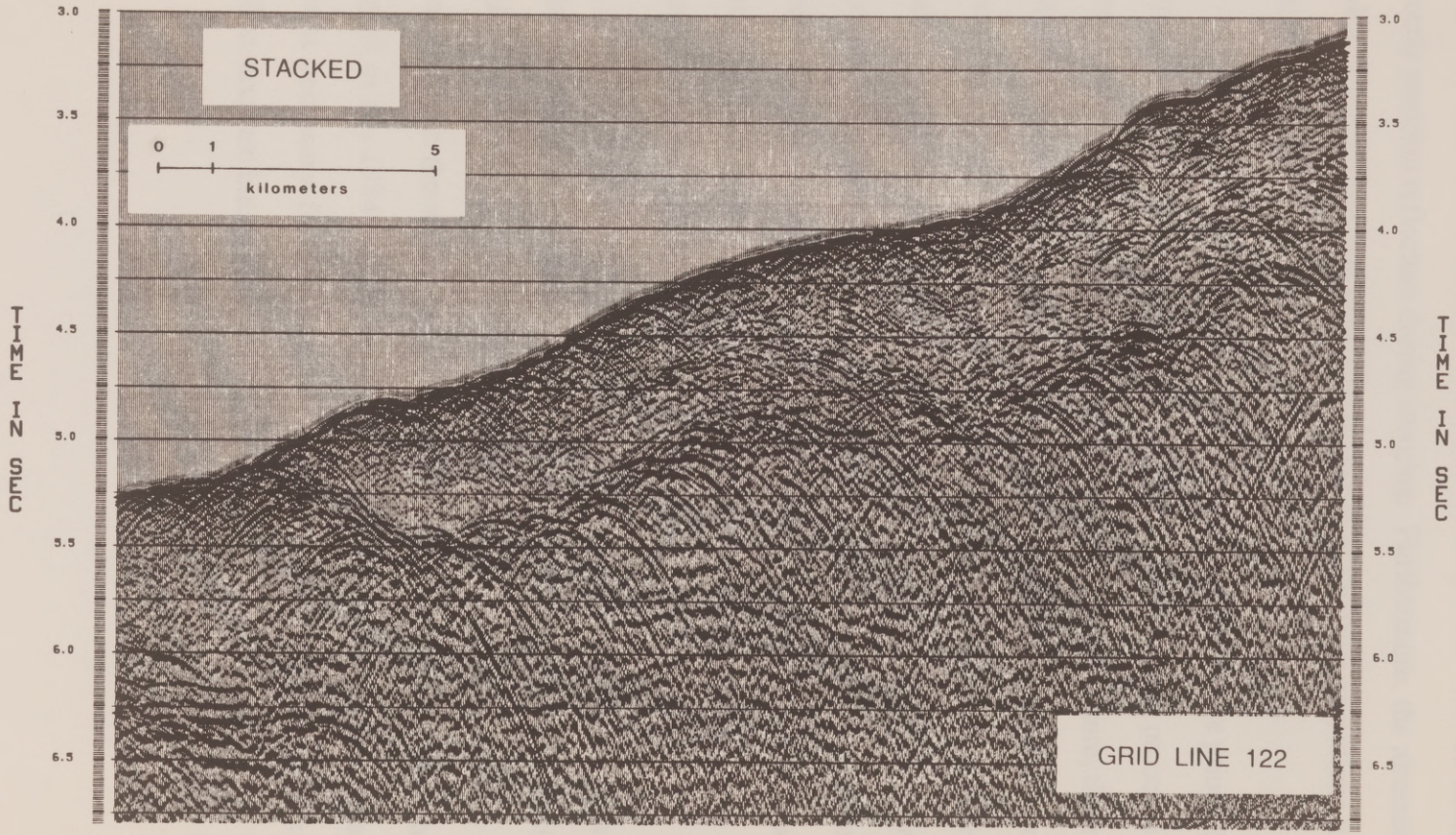

Figure 2. Stacked data from the middle bin line of the 3-D grid.

Consequently, lateral perturbations in the velocity field must be accommodated to correctly position reflectors during imaging. Furthermore, the absence of well data or wide offset seismic data necessitates the use of iterative migrations to solve for the velocity field.

The failure of earlier surveys to clearly image the wedge primarily stems from the sparse areal coverage and the absence of three dimensional processing operations. Because the geological structures are three dimensional in nature, three dimensional acquisition and processing are necessary to produce a proper representation of the subsurface. Much of the signal in two dimensional stacked seismic sections is actually generated by reflectors not within the plane of the section and should be removed during processing. Likewise, much of the energy from reflectors actually in the collection plane has traveled out of it. This problem is inherent to this environment. To solve it, dense three dimensional seismic coverage is necessary so that three dimensional migration can be performed.

In addition to providing a more accurate image, 3-D seismic data also facilitates better interpretation. In past studies of the Costa Rican accretionary margin, interpretations of widely spaced seismic data were unable to correlate structures within the wedge from one section to the next (Crowe and Buffler, 1983; Bourgois et al., 1984). The highly three dimensional nature of these structures makes it necessary for the interpreter to work in three dimensions to produce complete, accurate interpretations.

Acquisition Parameters as Imaging Constraints

In addition to environmental variables related to the geology, the quality of seismic data is also a function of field acquisition parameters. There are several ways in which the acquisition system effects the data quality. The frequency and noise content of the raw data depend on the specifications and reliability of the seismic source and recording system. The performance of the crew operating the equipment is also an important aspect of acquisition quality.

Both the precision of the navigation system and the degree to which navigation information is incorporated into the processing sequence play integral roles in determining the final data resolution. Accurate processing of source and receiver navigation is critical to the correct positioning of data during three dimensional processing. If the data collected are improperly organized, spatial smearing is introduced into the seismic image.

The density of spatial coverage is another important factor in determining spatial resolution. As part of the processing, seismic traces are summed, or stacked, to increase the data redundancy and thereby increase the signal-to-noise content. The size of the bins into which the data are sorted for stacking depends on the amount of redundancy which is required and the density with which the data were collected.

Acquisition Background

In April of 1987, the Institute for Geophysics at the University of Texas at Austin completed the acquisition of a large volume of seismic reflection data from offshore of Costa Rica's Nicoya Peninsula (Figure 1). The experiment was conducted aboard the R/V *Fred H. Moore* as part of a three dimensional seismic survey in the Middle America Trench. The greatest portion of the data comprise an areally dense grid of eighty-eight parallel seismic lines 100 meters apart and 23 kilometers long. This covered about a third of the continental margin in the dip direction. The 3-D grid comprised approximately 60,000 shots with a shot spacing of 33.3 meters (Figure 3). All data were collected with a 1065 cubic inch tuned source array. The R/V *Fred H. Moore* field system was composed of a 96-trace, 3800 meter long seismic streamer (Figure 4). The specifications of the acquisition system are listed in Appendix 1.

Nine 60 kilometer long dip lines extending from the Cocos Plate to the shelf edge off the Nicoya Peninsula were also collected, as well as twelve short strike lines. The longer lines, which form a sparse swath data set, are centered over the same area that was covered by the 3-D grid. The three inner lines are spaced 250 meters apart. From the middle swath line to the outermost swath line on either side, each line has twice the separation between it and its outward neighbor as between it and its inward neighbor.

The collection of the swath data set accomplished two specific purposes: (1) the nature of the collection allowed the *Fred Moore* to cover a larger tract of land than could be covered by a dense survey, and (2) because significantly less time was

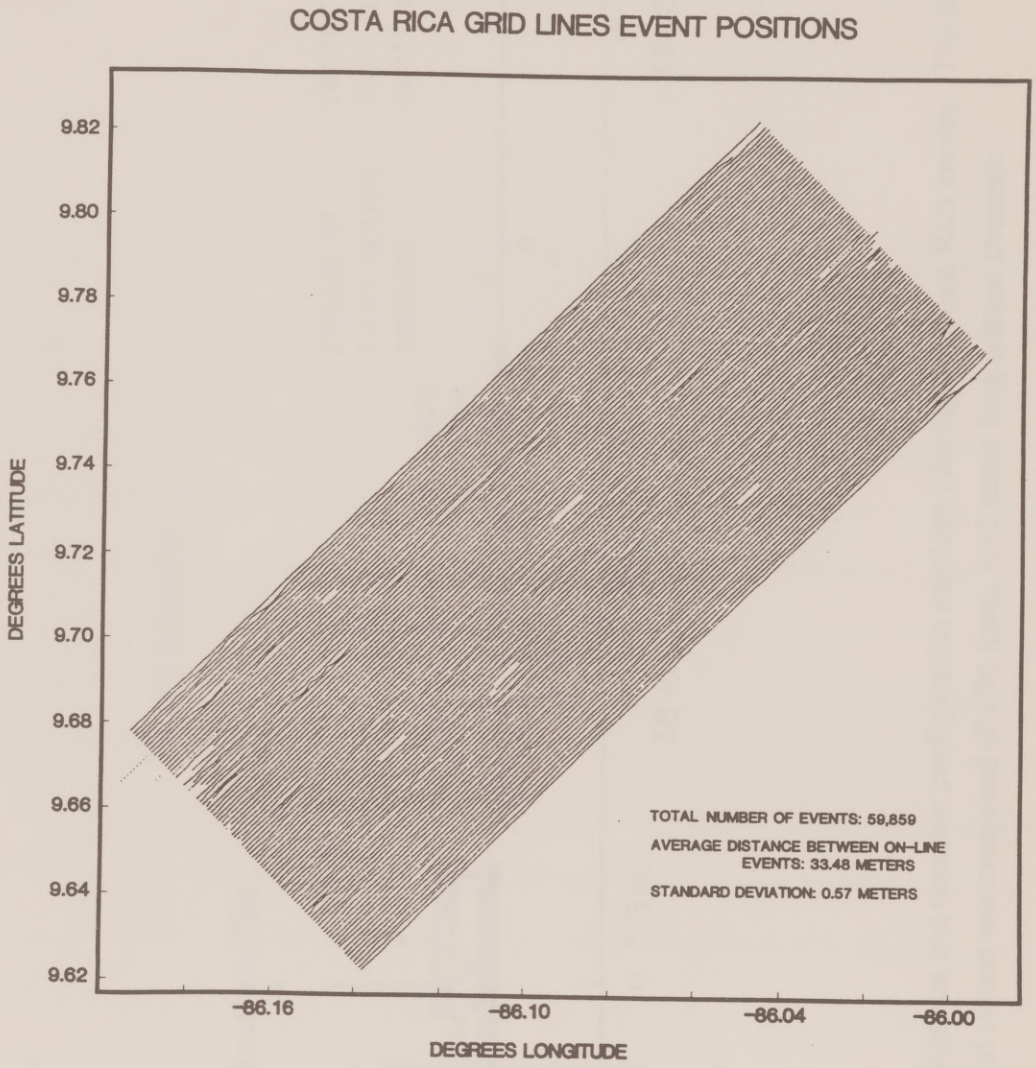

Figure 3. Ship locations for the approximately 60,000 shots comprising the 3-D grid.

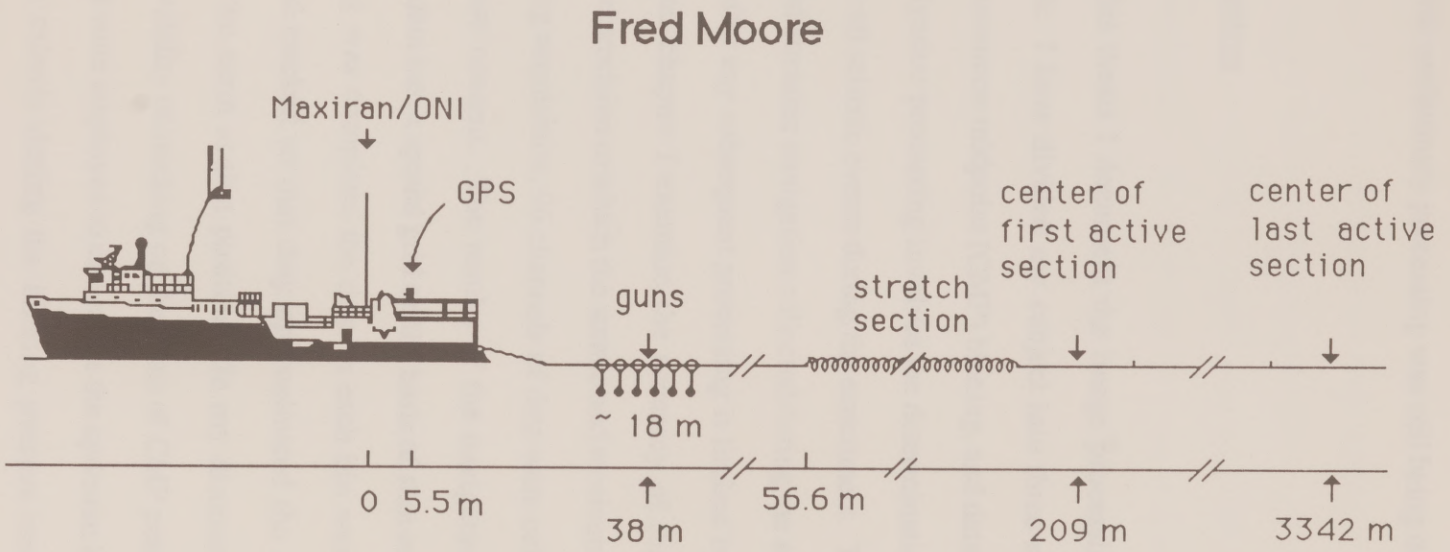

Figure 4. The navigation and streamer configuration employed during the Costa Rica survey. The R/V *Fred H. Moore* field system was composed of a 96-trace, 3342 meter long seismic streamer.

required for processing, a significant amount of research was performed using the 2-D data while preliminary processing was still being done for the 3-D grid.

Thesis Objectives

In this thesis I document the image processing of the UTIG Costa Rica seismic data. I have divided my subject into three areas of interest: navigation processing, common midpoint (CMP) binning, and data migrations.

Navigation processing involves the determination of the source and receiver positions for all seismic events during the experiment. These positions are calculated from ship and streamer navigation collected during the survey. The spatial resolution of the data after any subsequent processing is limited by the navigational precision. In the second chapter I examine the accuracy of the initial measurements and determine the precision to which the source and receivers were located.

During acquisition, 96 channels of data were collected to assure an adequate signal-to-noise content. The results of the navigation processing were used to organize the data into a spatial grid on the basis of shot-receiver midpoints. Once this CMP binning was complete, the data in each bin were normal moveout (NMO) corrected and stacked so that they approximated the zero source-receiver offset response of the earth at that position. In my discussion of data binning, I first examine the validity of stacking on the basis of CMP position. I then give the results of studies that were employed to determine the optimum bin size and grid orientation. Optimization criteria during the binning process must balance the competing

objectives of maintaining high spatial resolution (by minimizing the bin size) and obtaining a high signal-to-noise ratio in each bin (by maximizing the number of traces in each bin, i.e., the trace fold). In the final section of the third chapter I justify the dimensions chosen for the final binning grid.

In the fourth chapter I present examples of Costa Rica data after various poststack migrations. The migration process is vital to producing interpretable images of the Costa Rican accretionary wedge. Because of its importance, the initial section of this chapter presents an overview of poststack migration. I outline migration theory and compare methods by which migration can be implemented. Comparisons are included of finite difference and phase shift methods, as well as a comparison of time versus depth migrations.

In discussing imaging, I emphasize the necessity of imaging the Costa Rican accretionary wedge using three dimensional acquisition and processing. The superiority of full aperture 3-D migration over 2-D or 2-D by 2-D (Jakubowicz and Levin, 1983) methods is demonstrated. I also examine the effect of data density on the resulting migrated image. Because spatial aliasing becomes an important consideration in discussions both of data density and of highly accurate migration algorithms, I have included an appendix discussing spatial aliasing and filtering.

Both the grid and swath data were collected with the same equipment over the same area during this survey, so I had the opportunity to perform direct comparisons of the two data sets. In the final section of the fourth chapter, I discuss attempts to enhance the swath data images. These efforts included the interpolation of a regularly spaced 3-D grid of seismic data from swath lines so that a full aperture 3-D migration could be performed on the interpolated swath grid.

Chapter 2: Precision of Navigation

Accurate processing of the source and receiver navigation is critical to correct spatial positioning of the seismic data during three dimensional processing. Relative accuracy, the precision with which events in this survey are located relative to each other, is more important than absolute accuracy for the purpose of seismic imaging. Improper relative positioning of seismograms during binning introduces spatial smearing into the seismic image.

The reduction of the navigation to a final set of geographic coordinates requires a combination of field measurements and navigational models. Field measurements used in processing the Costa Rica navigation include range measurements from three land-based radio transmitters, global positioning system (GPS) navigation, ship gyrocompass measurements, and readings from ten magnetic compasses positioned within the seismic streamer. Modelling assumptions include spheroidal models of the Earth, propagation paths and velocities for radio signals, the position of the seismic source relative to the ship, geometric approximations of streamer bending, and the magnetic declination in the survey area. In this chapter I try to identify and quantify the error inherent in each component of the navigation. Schematic descriptions of each component are also included.

SHIP NAVIGATION

Offshore Navigation, Inc. (ONI) of New Orleans provided the ship navigation during the experiment. ONI continuously monitored the ship's position using a Maxiran long-range radio positioning system. The Maxiran system consisted of a shipboard unit and three land-based transponders. RECOPE, the Costa Rica national oil company, supplied ONI with the logistics and surveying of the three transmitter sites.

One factor which made the Costa Rica area a judicious choice for this survey was the proximity of the accretionary wedge to shore: the entire grid area was within 50 kilometers of the shoreline, and therefore within line of sight of the base stations. The resulting navigational accuracy allowed UTIG to collect the data using real-time navigation of the ship position. During periods of acquisition, seismic events were triggered whenever the system calculations indicated an advance in position of 33.33 meters. At that time, the current range and system data were recorded. GPS satellite based information was also available approximately one-fourth of each day. When available, GPS ranges and system positions were updated each second. When a shot command was issued and an extrapolated Maxiran position was recorded, the last available GPS measurements were also recorded. Figure 5 illustrates the interrelation of the navigational systems, the navigation recording system, and the seismic source.

The shipboard Maxiran unit interrogated the base stations with a signal, and the base stations responded immediately. The unit then determined the range to each transponder using the time lapse between the signal transmission and reception. An

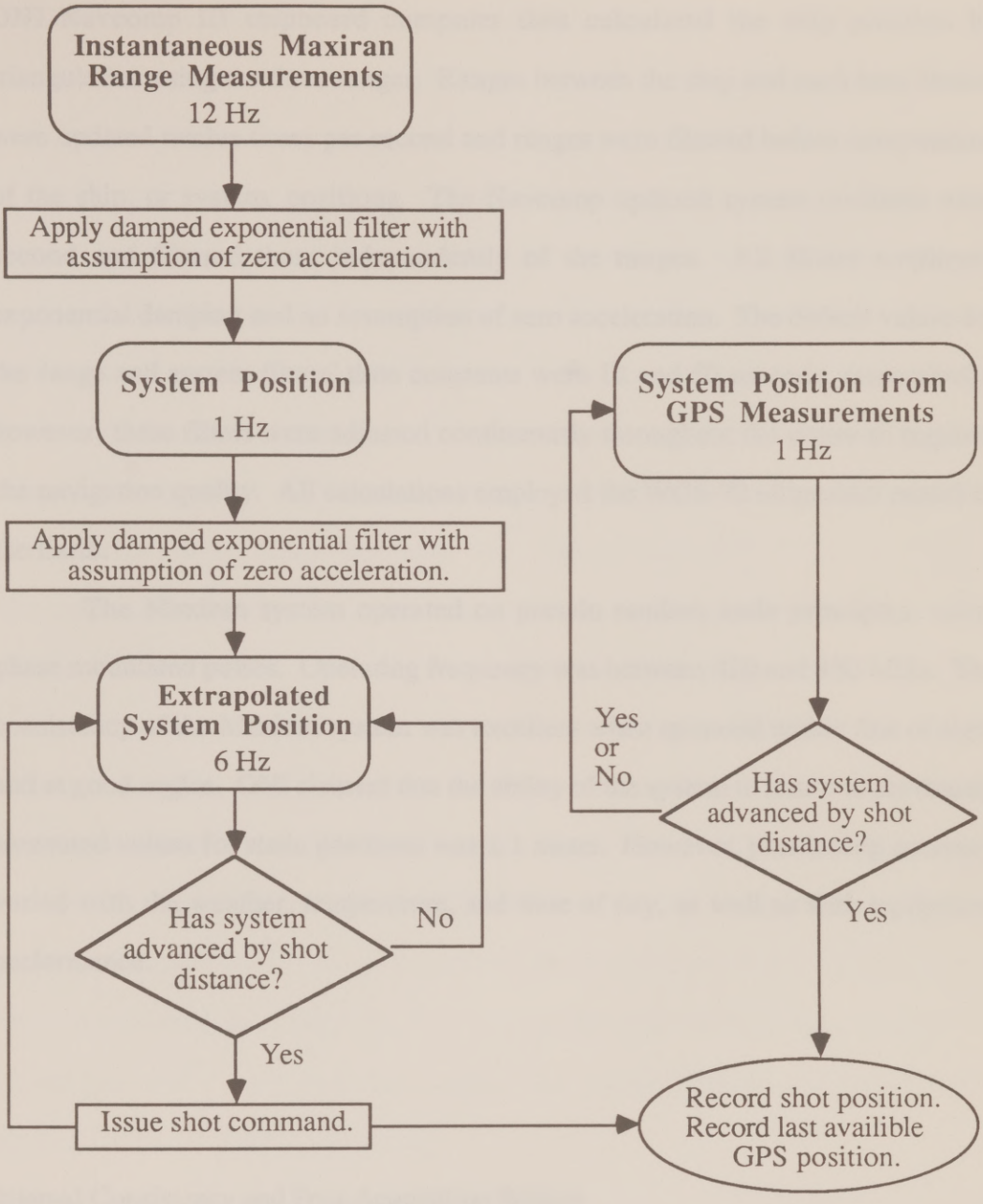

Figure 5. Phase and timing diagram for the navigation systems, the navigation recording system, and the seismic source.

ONI Navcomp III shipboard computer then calculated the ship position by triangulation using the three ranges. Ranges between the ship and each base station were updated twelve times per second and ranges were filtered before computation of the ship, or system, positions. The Navcomp updated system positions each second and filtered them independently of the ranges. All filters employed exponential damping and an assumption of zero acceleration. The default values for the range and system filters' time constants were 12 and 50 seconds, respectively; however, these filters were adjusted continuously throughout the cruise to regulate the navigation quality. All calculations employed the WGS-72 ellipsoidal model of the Earth.

The Maxiran system operated on pseudo random code principles, using phase modulated pulses. Operating frequency was between 420 and 450 MHz. The consistency of the Maxiran system was excellent when operated within line of sight and at good angles. ONI claimed that the ability of the system to return to previously measured values for static positions was ± 1 meter. However, positioning accuracy varied with the weather, temperature, and time of day, as well as with equipment performance.

Internal Consistency and Post-Acquisition Editing

When I reviewed the Costa Rica navigation for bad data values, I used the between shot acceleration as my primary measure of internal consistency. The shot

acceleration was calculated by taking the first backward derivative of the shot velocity. The shot velocity is the distance traveled by the ship between adjacent shots, and has units of meters per shot. After computing shot accelerations for a line, they were plotted to obtain a visual presentation of the navigation quality (Figure 6). Seismic events were triggered using predictive filtering of the Maxiran navigation, so the average Maxiran shot velocity for the experiment should have equalled the target shot velocity, 33.33 meters per shot. When the constant velocity model used for filtering was an accurate description of the ship's movement, and when the navigational quality was relatively consistent, the RMS deviation of the shot velocity values should have been low. For the acquisition of the dense Costa Rica data set, the average distance between on-line events was 33.48 meters per shot with a standard deviation of 0.57 meters. Bar graphs detailing these statistics for individual swath and grid acquisition lines are shown in Figures 7 and 8, respectively. Shot velocities related to missed shots and intervals of missed shots were not included in these averages; such inclusions would have deceptively raised the average shot velocities and their associated RMS deviations. The shot accelerations were usually close to zero, except where missed shots occurred. There the shot accelerations usually showed a positive and then negative jump of about 33 meters per shot^2. Selecting these jumps was straightforward, and gaps in data coverage were located in this manner.

The discrepancy between the target shot velocity of 33.33 meters per shot and the average value of 33.48 meters per shot results from the timing resolution of the navigational computer system. The Navcomp computer used has a timing resolution of 0.17 seconds. The average time between events was approximately 19

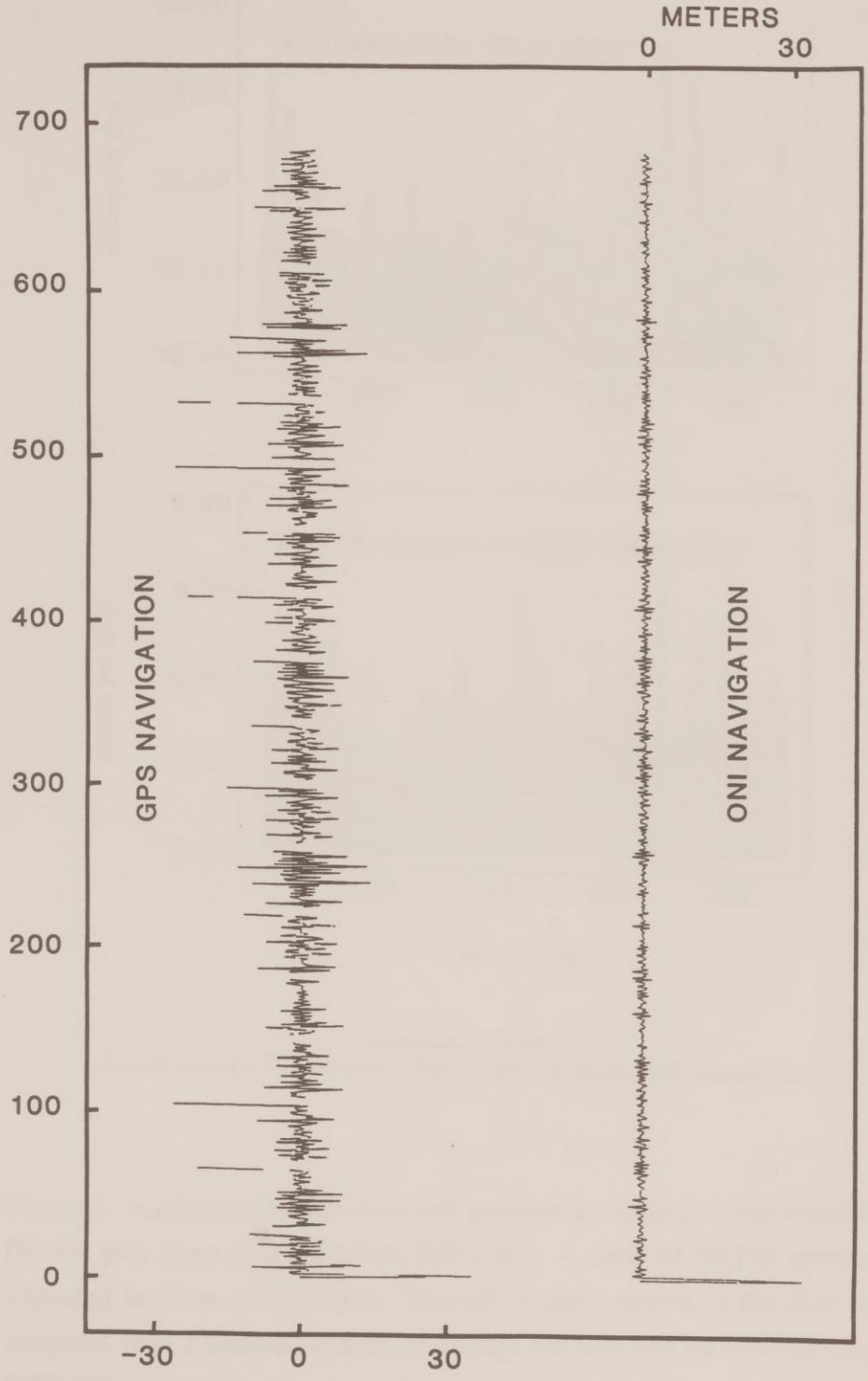

Figure 6. The between shot acceleration for one grid acquisition line using GPS (upper) and Maxiran (lower) navigation. The GPS data are not filtered and data gaps are present.

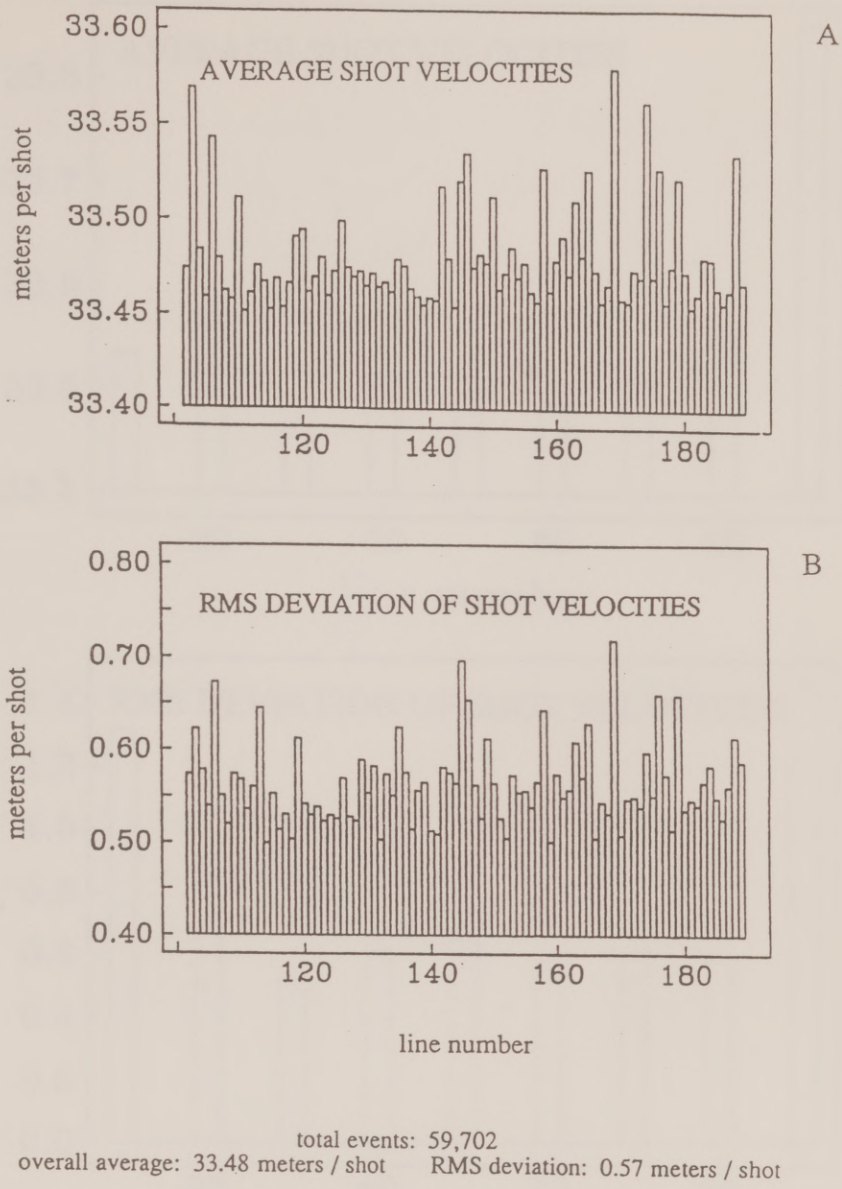

Figure 7. Average shot velocities and standard deviations of shot velocities for the 88 grid lines (line numbers 102-189). A total of 59,702 events were included in these calculations. Overall, seismic events in the 3-D data set occurred with a frequency of 33.48 meters per shot and an RMS deviation of 0.57 meters per shot.

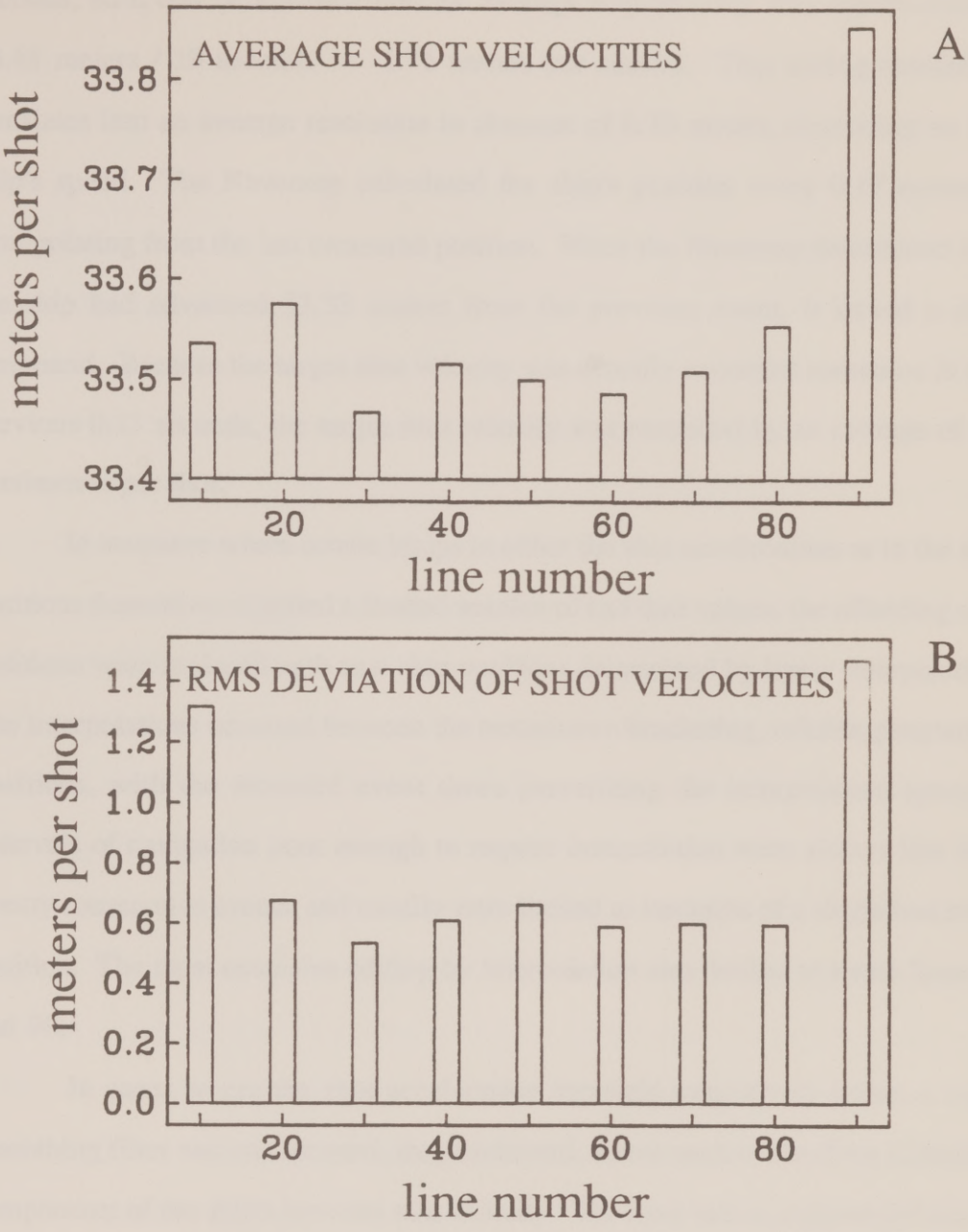

Figure 8. Average shot velocities and standard deviations of shot velocities for the 9 swath lines (line numbers 10-90). A total of 15,285 events were included in these calculations. Seismic events were acquired with an average frequency of 33.55 meters per shot and an RMS deviation of 0.90 meters per shot.

seconds, so it can be assumed that the average ship velocity was approximately 33.48 meters / 19 seconds = 1.76 meters per second. This timing resolution translates into an average resolution in distance of 0.30 meters, depending on the ship's speed. The Navcomp calculated the ship's position every 0.17 seconds, extrapolating from the last measured position. When the Navcomp determined that the ship had advanced 33.33 meters from the previous event, it issued a shot command. Because the target shot velocity was actually exceeded sometime in the previous 0.17 seconds, the target shot velocity was exceeded by an average of 15 centimeters per shot.

In instances where erratic jumps in either the shot accelerations or in the ship positions themselves signaled a limited number of bad data values, the offending ship positions were replaced with new ship positions determined by linear interpolation. The interpolations occurred between the nearest two bracketing, reliable geographic positions, with the recorded event times prescribing the interpolation spacing. Intervals of navigation poor enough to require interpolation were always less than twenty consecutive events, and usually were limited to instances of a single bad event position. The most extensive editing by interpolation was limited to swath lines 10 and 90.

In cases where the shot acceleration appeared excessively noisy, a mild smoothing filter was run forward, then backward, across each of the three Cartesian components of the ship's between shot velocity. The filter had an exponential decay of 0.62 per shot (i. e., $\exp[^{-1}/_{0.62}] = 20\%$). This gave the shot velocity variance for the offending periods the same character as that exhibited during most of the experiment. For the grid data, this filtering was necessary in two areas and involved

less than 1000 of the total 60,000 shots. For the swath lines, filtering was required on six of the nine lines where the ship was beyond the line of sight of the navigation stations.

Degradation of Navigation with Distance

Approximately the far shore third of the swath lines was beyond line of sight of the base stations, and the Maxiran navigational system works best when used within line of sight. When the ship's antenna is no longer within line of sight, the signal is carried over the horizon within a narrow radio propagation "duct" above the air / sea interface. This introduces uncertainties in the propagation path geometry and multipath interference. The effect on the navigation quality is demonstrated by the RMS deviations of the swath line shot velocities, which were larger than for the 3-D acquisition lines.

To document the effect of multipathing on navigational precision, the calculations described above were repeated for the third of the swath lines farthest from shore. The resulting averages were compared to those for the near shore two-thirds of the swath data set in Figure 9A. Figure 9B illustrates the differences in the standard deviations. The statistics for the near shore two-thirds of the swath lines were almost identical to those for the grid lines: an overall average velocity of 33.48 meters per shot with a standard deviation of 0.58 meters. For the far shore third of the data set, the analysis revealed an average velocity of 33.63 meters per shot with a standard deviation of 0.92 meters.

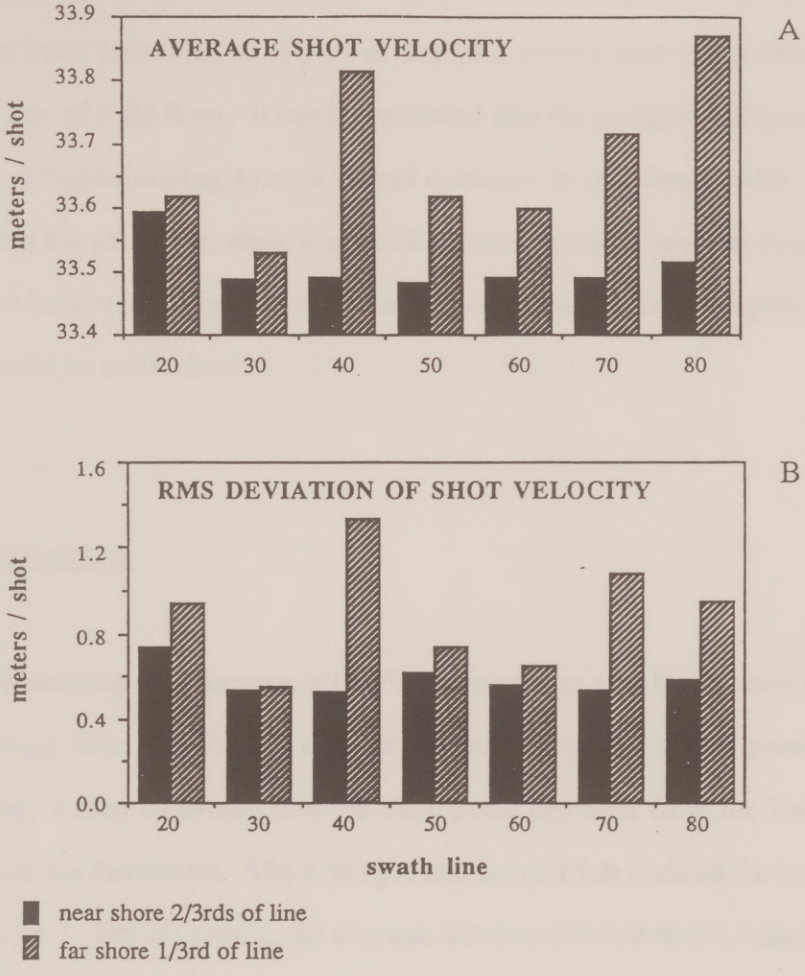

	near shore events	far shore events
number of events:	7882	4372
overall average:	33.48 meters / shot	33.63 meters / shot
RMS deviation:	0.58 meters / shot	0.92 meters / shot

Figure 9. Study documenting degradation of navigational accuracy with increasing distance from shore. Navigational statistics are shown for 7 swath lines. The near shore two-thirds of each line was within line-of-sight of the land based navigation stations, while the far shore two-thirds of each line was just beyond the horizon.

This study clearly illustrates the degradation in navigational precision which would have been encountered if part of the grid survey had fallen even slightly beyond the line of sight limit. It can be predicted that the navigational quality of any land-based radiopositioning system would continue to deteriorate with increasing distance from the shoreline, since multipath problems would become more extreme and it would be increasingly difficult to locate base stations such that good angles of operation could be maintained.

Ship Maneuverability

To determine how accurately the *Fred Moore* was able to maintain its position on the shooting line, I performed a linear regression analysis on the event positions for each line. I then measured how far each event deviated from the linear model, and averaged the deviations. The averages and standard deviations for each line are listed in Table 1. For all events, the average distance off-line was 5.2 meters, with a standard deviation of 5.5 meters. This implied that two-thirds of all shots fell within 11 meters of the acquisition "centerlines" defined by my linear analysis. On the basis of these results, the acquisition lines probably could have been collected with a 50 meter spacing without producing gaps in the acquisition grid. The shot-to-shot variability in the off-line deviation was 0.0 meters with a standard deviation of 1.6 meters (Table 2).

I next calculated the distance of each line from its northwest neighbor, using the centerline models of the acquisition lines and the perpendicular to the average

Table 1: Average offline distance and associated standard deviations by line.

LINE	AVERAGE OFFLINE DISTANCE (meters)	RMS DEVIATION (meters)	LINE	AVERAGE OFFLINE DISTANCE (meters)	RMS DEVIATION (meters)
102	4.9	4.4	147	5.9	6.2
103	11.7	11.7	148	3.6	2.8
104	6.0	4.5	149	6.9	6.0
105	3.7	2.3	150	5.4	4.8
106	6.7	6.3	151	4.2	3.0
107	5.0	4.3	152	4.7	3.6
108	5.3	4.3	153	4.4	2.9
109	4.6	3.8	154	4.9	4.4
110	9.4	11.8	155	3.5	2.6
111	3.2	2.8	156	4.2	3.1
112	3.1	2.1	157	5.3	4.3
113	4.0	3.0	158	5.0	3.3
114	3.7	2.7	159	6.6	4.7
115	2.2	1.8	160	5.0	4.4
116	5.1	4.1	161	4.5	3.6
117	3.4	3.1	162	3.7	2.9
118	6.0	6.1	163	8.0	6.2
119	7.2	6.6	164	5.1	4.1
120	6.1	5.1	165	7.6	6.1
121	5.9	4.8	166	4.0	3.1
122	6.2	5.4	167	3.9	3.0
123	6.6	5.4	168	3.1	2.7
124	3.9	3.1	169	5.5	6.0
125	4.2	4.0	170	3.2	2.5
126	6.9	8.4	171	4.3	3.1
127	6.8	5.6	172	3.6	2.9
128	4.9	4.5	173	3.7	2.7
129	4.6	3.6	174	7.4	5.8
130	6.1	6.9	175	5.8	4.2
131	4.1	3.6	176	6.3	13.1
132	3.6	3.0	177	4.4	3.4
133	4.3	3.1	178	3.4	2.4
134	4.5	4.1	179	4.1	3.6
135	5.7	4.3	180	3.6	3.0
136	3.4	2.7	181	6.7	5.6
137	7.7	7.3	182	5.1	4.5
138	3.4	2.4	183	5.5	5.0
139	3.0	2.3	184	4.9	4.1
140	3.1	2.5	185	5.3	4.0
141	5.2	4.1	186	4.9	5.5
142	4.9	3.5	187	5.3	3.9
143	6.0	5.9	188	12.7	16.4
144	5.7	4.1	189	5.7	4.0
145	8.6	7.2			
146	3.8	2.7	Overall	5.2	5.5

Table 2: Shot-to-shot change in offline deviation.

LINE	NUMBER OF EVENTS	RMS DEVIATION (meters)	LINE	NUMBER OF EVENTS	RMS DEVIATION (meters)
102	683	1.4	147	681	1.5
103	649	2.8	148	683	1.6
104	683	1.6	149	664	1.5
105	142	1.3	150	683	2.1
106	681	1.8	151	683	1.3
107	683	1.5	152	682	1.4
108	683	1.3	153	123	1.6
109	683	1.2	154	683	1.4
110	673	2.1	155	683	1.4
111	682	0.9	156	683	1.2
112	682	1.2	157	683	1.1
113	492	1.2	158	149	1.8
114	683	1.2	159	683	1.3
115	683	0.9	160	227	2.1
116	679	1.3	161	677	1.7
117	685	1.0	162	683	1.4
118	661	1.3	163	683	2.1
119	683	1.8	164	156	2.4
120	644	1.8	165	683	2.3
121	670	1.2	166	682	1.4
122	683	1.4	167	683	1.1
123	676	1.6	168	683	1.2
124	682	1.2	169	683	3.1
125	673	1.5	170	464	1.2
126	670	2.0	171	683	1.1
127	683	1.5	172	683	1.5
128	683	1.4	173	683	1.4
129	683	1.4	174	683	3.0
130	680	1.4	175	682	1.4
131	683	1.4	176	681	2.4
132	683	1.3	177	683	1.1
133	683	1.3	178	683	1.5
134	682	1.2	179	683	2.3
135	683	1.5	180	682	1.4
136	682	1.4	181	683	1.1
137	683	1.4	182	679	1.2
138	679	1.3	183	683	1.5
139	681	1.1	184	683	1.6
140	301	0.9	185	683	1.3
141	683	1.1	186	683	1.0
142	662	2.0	187	681	1.3
143	681	1.6	188	664	2.5
144	689	1.1	189	683	1.4
145	683	2.2	---	---	-----
146	289	1.7	Overall	56059	1.4

trend of acquisition. The purpose of this measurement was to determine how well the ship was able to use the navigation to define each acquisition line. The centerlines averaged a distance of 99.5 meters apart, with a standard deviation of 4.5 meters (Table 3). The above statistics demonstrate that the consistency of the navigation was much better than the actual ability of the ship to hold a straight line.

GPS Navigation

In addition to the land-based navigation system, the experiment had access to GPS-NAVSTAR satellite navigation. With GPS, the navigation unit determines its position from broadcast values of the positions and velocities of several navigation satellites. The navigation satellites also transmit a signal which the navigation unit compares to a self-generated reference signal to measure the phase difference and determine, not the range to each satellite, but the relative differences in the satellite ranges. (The use of range differences as navigational parameters rather than ranges avoids problems related to a lack of strict synchronization between the satellite and user generated signals.) The range difference relative to two satellites specifies a hyperbolic position surface which includes the user position. The user position can be determined from the intersection of three such surfaces.

A complete position solution using the GPS system requires the input from four satellites. Marine users, however, know that their position lies on the surface of the sea-level geoid. By assuming that the ellipsoidal Earth model is an accurate

Table 3: The average distance of each line from its neighboring line to the northwest.

LINE	DISTANCE FROM NW NEIGHBOR (meters)	LINE	DISTANCE FROM NW NEIGHBOR (meters)
103	106.1	147	99.7
104	93.4	148	99.9
105	80.6	149	99.0
106	115.6	150	96.9
107	103.5	151	103.0
108	99.7	152	97.7
109	96.9	153	115.7
110	104.2	154	84.5
111	95.2	155	100.2
112	100.2	156	97.9
113	100.6	157	102.4
114	97.5	158	102.7
115	99.3	159	96.3
116	99.5	160	89.2
117	101.0	161	108.5
118	98.1	162	97.6
119	102.8	163	103.0
120	97.3	164	97.0
121	97.5	165	98.8
122	103.5	166	99.5
123	98.4	167	99.7
124	97.1	168	100.3
125	101.5	169	96.8
126	100.5	170	101.2
127	96.8	171	98.2
128	97.0	172	99.3
129	104.9	173	99.8
130	94.3	174	99.3
131	103.4	175	100.9
132	98.0	176	97.9
133	99.6	177	101.2
134	100.6	178	98.9
135	99.4	179	98.4
136	99.5	180	99.0
137	101.4	181	99.8
138	96.3	182	98.8
139	98.3	183	102.3
140	99.3	184	97.0
141	100.0	185	99.9
142	101.4	186	98.8
143	100.7	187	100.6
144	99.4	188	99.9
145	94.5	189	98.3
146	101.9	Overall	99.5

description of the geoid, this a priori vertical position information can be used to reduce the number of unknowns in the problem. This makes the solution an overdetermined one, and allows navigation acquisition to continue in periods when only three satellites are available. Because the vertical component of the navigation is the most sensitive to increases in the geometric dilution of precision (DOP) (Ligon, 1985), applying a priori vertical knowledge significantly lowers the variance of the navigation. One should be aware, though, that systematic errors can arise from an incorrect assumption about the vertical position.

Another advantage of using a priori vertical information is that, by desensitizing the navigation to geometry effects, the frequency of constellation changes necessary to maintain adequate DOP is reduced. This is desirable because significant position discontinuities sometimes occur when the satellite set selection is changed. Frequent satellite switching could have an untoward effect on the consistency of acquisition for a survey trying to operate by GPS navigation. Unfortunately, since satellite positions are dynamic, the navigation operator usually has little or no control over where constellation changes occur. Most of the GPS fixes acquired during this experiment were made using three satellites, although some fixes used input from four satellites. Height above the ellipsoid was provided using the last available position determination made with four satellites.

When it is completed, the NAVSTAR-GPS space-based radionavigation system will operate using eighteen NAVSTAR satellites. During this experiment, GPS navigation constellations could only be constructed from the six available and healthy satellites. As a result, reliable GPS navigation was available for approximately one-fourth of each day. GPS fixes were considered reliable if they

were made using a constellation composed of three or more satellites and having reasonable horizontal DOP. Although the GPS coverage was not continuous, 13,500 measurements incorporating reliable GPS navigation were obtained over the course of the cruise. These data were used to evaluate the systematic and absolute accuracy of the land-based Maxiran system.

GPS - Maxiran Comparison

GPS positions were recorded with each seismic event. These positions were only updated each second, and at shot time the last available GPS position was recorded without attempting to extrapolate for the interval between when the fix was made and when the shot command was issued. The GPS time at which each fix was made was also recorded, but the GPS clock was not synchronized with the shot clock, so accurate position reconciliations were not possible during post-acquisition processing. On average, however, the ship moved only 0.9 meters between the time the recorded GPS fix was made and the time a shot command was issued. Taking this into consideration, I made a rough comparison of the positions provided by the two systems.

An immediate discrepancy was apparent in the absolute positions of the two systems. The GPS system showed an average apparent offset of 355.8 meters at an azimuthal angle of 139.7° with respect to the Maxiran system. The standard deviations of these values were relatively small (approximately 10 meters and 2.1°) and I observed no significant trends in these offsets with respect to either time of

acquisition or position within the data set. (Any rotation which might have been present would not be noticeable at this scale.) GPS and Maxiran positions for the same acquisition line are shown in Figure 10, and the averages and RMS deviations of the shot velocities for the grid acquisition are listed.

The offset between the two systems is probably primarily due to the use of different datums in establishing the local coordinate grid. Although the ONI system calculated ship positions using the WGS-72 ellipsoid, the ONI base stations were surveyed into position using a Clarke spheroid and a local datum. To correct for the large offset between the two systems, I translated all land-based navigation by a constant range of 356 meters and an azimuth of 140 degrees so that it adhered to the GPS standard.

In addition to the coarse datum comparison, I was able to conduct a finer scale study of relative system accuracy by assuming the difference in the drift rates of the two system clocks was negligible. GPS positions and times were used to estimate the average ship velocity over two shot intervals. Using the shot time interval provided by the shot clock, a GPS estimate of the shot velocity was obtained. Figure 11 shows scaled histograms of all shot velocities obtained during acquisition of the grid data for both the Maxiran and GPS systems. The average GPS-derived shot velocity was 33.45 meters per shot with a standard deviation of 2.56 meters per shot. Table 4 compares the system statistics on a line-by-line basis for events with both land-based and GPS navigation.

Several considerations justify the use of the shot velocity as the measure of the ship's navigation accuracy. Because the primary concern is with relative

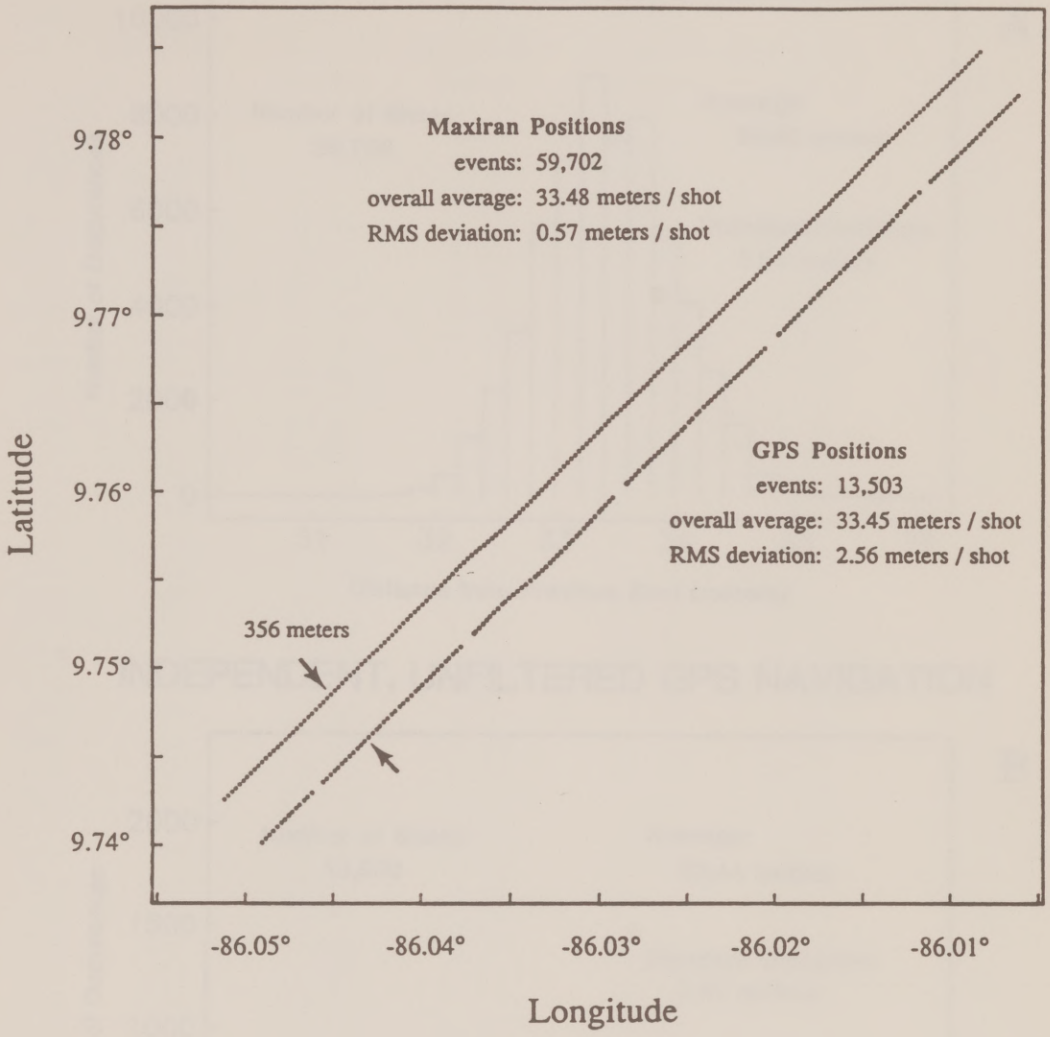

Figure 10. Maxiran and GPS positions for 200 consecutive events during seismic acquisition. There is an apparent offset of 356 meters at an azimuthal angle of 320° from north for the Maxiran positions with respect to the GPS positions. The data drop-outs in the GPS navigation occurred approximately every 15 minutes throughout the course of the survey. These gaps in coverage were not included in the calculations of statistical information.

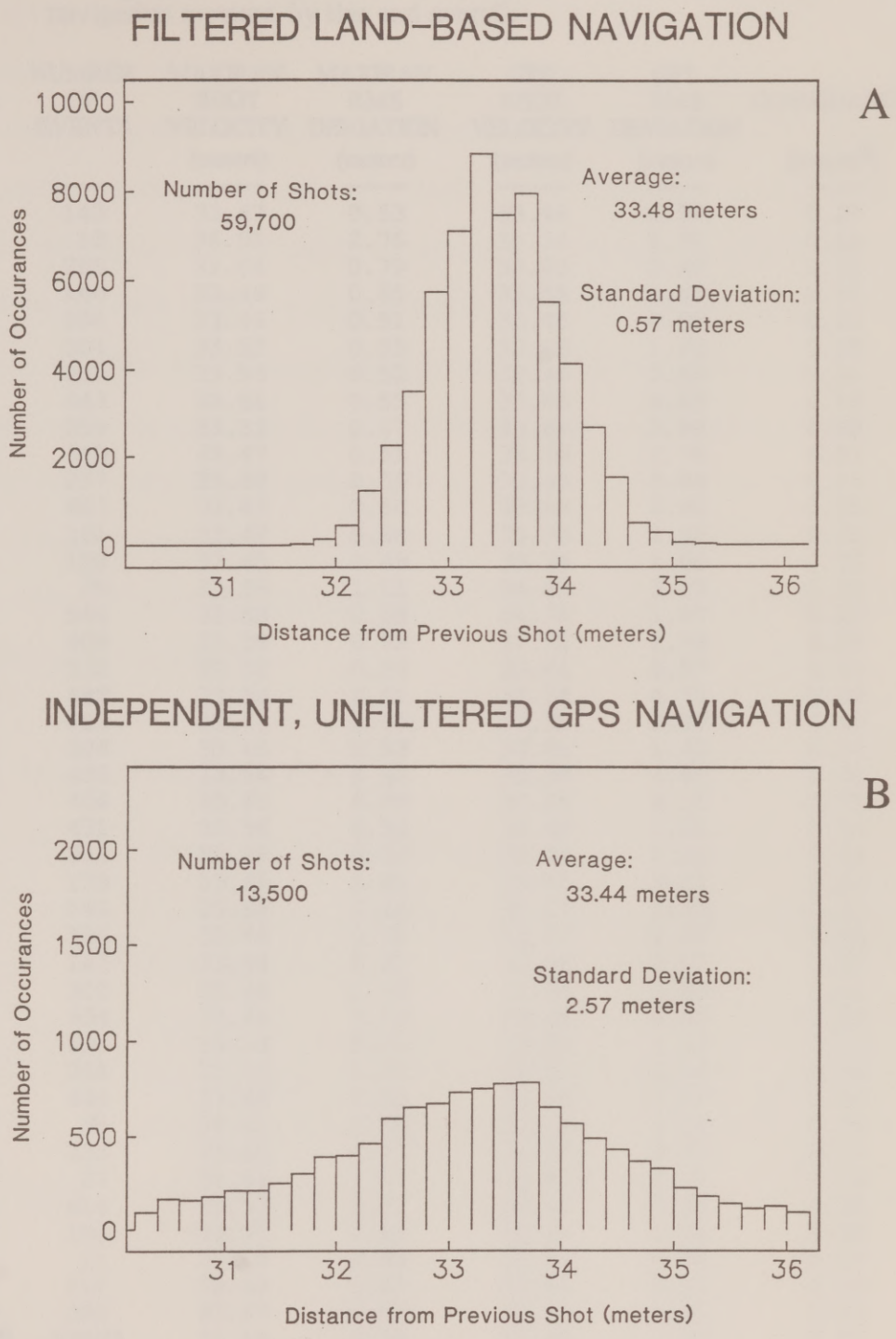

Figure 11. Scaled histograms of all shot velocities obtained during acquisition of the grid data for both the Maxiran and GPS systems.

Table 4: Average shot velocities, RMS deviations, and covariances for the two ship navigation systems, by line and overall.

LINE	NUMBER OF EVENTS	MAXIRAN SHOT VELOCITY (meters)	MAXIRAN RMS DEVIATION (meters)	GPS SHOT VELOCITY (meters)	GPS RMS DEVIATION (meters)	COVARIANCE ($meters^2$)
102	143	33.47	0.53	33.46	0.97	0.27
103	13	36.01	2.76	33.34	1.91	0.32
106	256	33.64	0.79	33.83	2.42	0.22
111	166	33.46	0.55	33.55	1.47	0.25
114	594	33.46	0.51	33.45	0.92	0.20
115	504	33.52	0.55	32.65	1.93	0.26
116	551	33.53	0.52	32.49	2.10	0.21
117	543	33.51	0.53	33.86	4.80	0.14
119	259	33.53	0.67	33.64	3.98	0.08
123	340	33.47	0.51	33.38	2.74	0.17
124	237	33.58	0.55	33.48	0.84	0.14
132	607	33.47	0.50	33.44	0.90	0.18
134	161	33.47	0.54	33.36	1.92	0.21
140	158	33.45	0.49	33.38	1.06	0.10
141	35	34.36	1.11	34.95	3.23	0.30
142	566	33.58	0.58	34.74	1.97	0.21
143	408	33.58	0.62	31.71	1.59	0.28
144	532	33.52	0.56	33.44	0.97	0.25
145	442	33.58	0.71	33.24	4.78	0.28
146	213	33.65	0.59	33.58	1.37	0.15
148	506	33.48	0.53	33.45	1.42	0.24
149	455	33.54	0.65	35.98	4.80	0.30
150	400	33.60	0.58	34.26	4.55	0.15
151	431	33.54	0.52	33.48	1.11	0.15
152	341	33.58	0.52	33.71	1.31	0.24
153	179	33.66	0.61	35.43	3.17	0.22
154	149	33.68	0.66	31.17	1.25	0.31
155	195	33.68	0.61	30.57	1.27	0.28
157	143	33.44	0.53	32.48	1.97	0.20
159	502	33.46	0.48	32.18	2.60	0.14
162	554	33.46	0.56	33.49	0.89	0.23
164	135	33.53	0.55	33.48	1.12	0.21
170	258	33.45	0.51	33.61	2.24	0.19
172	444	33.46	0.55	33.44	0.97	0.24
173	35	34.41	1.18	33.13	3.26	0.39
175	233	33.46	0.53	34.58	3.70	0.12
177	27	34.63	1.47	34.43	4.71	1.23
178	616	33.53	0.52	33.46	0.96	0.22
179	155	33.77	0.65	33.27	1.64	0.25
186	11	33.40	0.42	33.61	0.54	0.13
187	611	33.50	0.61	33.48	0.91	0.25
189	395	33.47	0.57	33.43	1.45	0.23
Overall	13503	33.48	0.56	33.45	2.56	0.22

uncertainties, a measurement is needed that directly couples individual position uncertainties; the shot velocity provides such a measurement. Also, a large ship holds a steady heading relatively well, so erratic sideways movements have a small effect on the overall shot velocity. As a result, the shot velocity can be considered as a scalar variable which can be easily manipulated. A more formal study would have to include all three spatial components of the position measurements and their variances; as a first order approximation I assumed that all uncertainties are spatially homogeneous. By assuming that positional errors are not angularly biased, 2-D generalizations of RMS uncertainties can be made later.

The shot velocity, SV, is a discrete, random variable associated with a finite set of values. It can be considered as a linear function of other discrete, random variables defined as follows:

SV: True shot velocity.

SV_M: Maxiran / Navcomp measurement of the shot velocity.

TSV_M: Maxiran / Navcomp measurement of the target shot velocity, 33.33 meters per shot.

DV_M: Residual between the Maxiran shot velocity SV_M and the Maxiran target shot velocity TSV_M. This is an internal measurement of the performance of the Maxiran / Navcomp predictive filter.

DX_M: Residual between the Maxiran shot velocity SV_M and the true shot velocity SV.

SV can then be written as

$$SV = TSV_M + DV_M - DX_M. \quad (1)$$

Because the target shot velocity, TSV_M, remained unchanged throughout the experiment, its variance is zero. By the definition of DV_M, its variance is equal to the variance of the Maxiran shot velocity. The earlier estimate of internal consistency, then, was a measure of $\sigma_{SV\text{-}M}$, the square root of the variance of the Maxiran shot velocity. What is desired, however, is some knowledge of $\sigma_{DX\text{-}M}$, the standard deviation of the navigation error. The difference in the information contained in these two values can be illustrated by allowing the mean Maxiran shot velocity to equal the Maxiran target shot velocity. If the predictive component of the Maxiran radionavigation system had been able to trigger all the events on exactly the target value, DV_M would always be zero, and SV_M would be always equal to TSV_M. There would then be no variance in the measured shot velocity. But while the Maxiran shot velocity measurements would be perfectly repeatable, this statistic would not provide any information about the accuracy of those measurements. The variance of the system reliability ($\sigma_{DX\text{-}M}^2$) is coupled to the variance of the true shot velocity, so neither can be determined independently.

To obtain an estimate of the navigation accuracy, GPS measurements of the shot velocity can be brought into the problem. The GPS shot velocity can also be considered as a discrete random variable which is a linear function of other random variables. It is represented as

$$SV_G = SV + DX_G. \quad (2)$$

DX_G is the residual between the GPS measurement of the shot velocity and the elusive "true" shot velocity. After combining this with (1), the description of SV_M, the result is

$$SV_G = TSV_M + DV_M - DX_M + DX_G. \quad (3)$$

In terms of the accuracy of the Maxiran system,

$$DX_M = TSV_M + DV_M - SV_G + DX_G. \quad (4)$$

The variance of DX_M can be stated in terms of the variances and covariances of the random variables on the right of (4):

$$\begin{aligned} \sigma_{DX\text{-}M}^2 = {} & \sigma_{TSV\text{-}M}^2 + \sigma_{DV\text{-}M}^2 + \sigma_{SV\text{-}G}^2 + \sigma_{DX\text{-}G}^2 \\ & + 2\,\mathrm{Cov}(TSV_M, DV_M) - 2\,\mathrm{Cov}(TSV_M, SV_G) \\ & + 2\,\mathrm{Cov}(TSV_M, DX_G) - 2\,\mathrm{Cov}(DV_M, SV_G) \\ & + 2\,\mathrm{Cov}(DV_M, DX_G) - 2\,\mathrm{Cov}(SV_G, DX_G). \end{aligned} \quad (5)$$

Since, by definition, the variance of TSV_M is zero, the first, fifth, sixth and seventh terms are zero. If we assume no correlation between the performance of the predictive Maxiran filter and the accuracy of the GPS system, the ninth term is also zero. This reduces the expression to

$$\sigma_{DX\text{-}M}^2 = \sigma_{DV\text{-}M}^2 + \sigma_{SV\text{-}G}^2 + \sigma_{DX\text{-}G}^2 - 2\,\mathrm{Cov}\,(DV_M, SV_G) - 2\,\mathrm{Cov}\,(SV_G, DX_G). \quad (6)$$

Unfortunately, no direct knowledge of DX_G is available. One method of collecting a reasonably good estimate of DX_G would have been to position a stationary GPS system at a known position and record position fixes simultaneously with the system positions recorded on the ship. [This is the operation principle behind differential GPS schemes, which use two GPS systems to provide excellent dynamic navigation (Sil'vestrov, 1986).]

Because the covariance between the GPS-measured shot velocity and the GPS reliability is unknown, the above equation cannot be solved directly. However, it follows from (2), and from the assumption that $\sigma_{DX\text{-}G}^2$ is uncorrelated with σ_{SV}^2, that

$$\sigma_{SV\text{-}G}^2 = \sigma_{SV}^2 + \sigma_{DX\text{-}G}^2, \quad (7)$$

and therefore $\sigma_{DX\text{-}G}^2$ cannot be larger than $\sigma_{SV\text{-}G}^2$. If $\sigma_{SV\text{-}G}^2$ is used as an upper limit for $\sigma_{DX\text{-}G}^2$, upper and lower bounds can be placed on $\sigma_{DX\text{-}M}^2$. The overall values in Table 4 provide the following values:

$$\sigma_{DV\text{-}M} = 0.56 \text{ meters per shot},$$

$$\sigma_{SV\text{-}G} = 2.57 \text{ meters per shot},$$

$$\mathrm{Cov}\,(DV_M, SV_G) = 0.22 \text{ (meters per shot)}^2.$$

By assuming the covariance between SV_G and DX_G varies between none and absolute, it follows that that $\sigma_{DX\text{-}M}$ falls between 0.0 and 3.6 meters per shot. The associated 2-D RMS uncertainty is $\sqrt{2}\ \sigma_{DX\text{-}M}$, which, for the high estimate, equals 5.1 meters per shot. (For an isotopic probability distribution, the relation between two dimensional and one dimensional variances is given by $\sigma_{2D}^2 = 2\ \sigma_{1D}^2$.)

Anyone familiar with static studies of the accuracy of instantaneous GPS measurements may be disturbed by the low standard deviation obtained for the GPS measurements. To understand why this uncertainty seems so small, I will briefly examine the process by which the GPS shot velocities were acquired. The manufacturer of the Trimble Model 4000A GPS Locater claims that with low horizontal DOP and a priori altitude information accurate to one meter, the positioning accuracy of GPS fixes is better than seven meters. This value represents a two dimensional RMS uncertainty.

One reason for the low RMS uncertainty observed here is that this study involved velocity measurements. Two GPS positions were used to calculate the ship's velocity, so the confidence of the velocity measurement was higher than that of either individual fix. Assuming no acceleration, and neglecting clock error, the relation between this estimate and the true velocity is given by

$$v_{true} = v_{gps} + \varepsilon_v = \frac{P1_{gps} - P2_{gps}}{\Delta t} + \frac{\varepsilon_{P1\text{-}gps} - \varepsilon_{P2\text{-}gps}}{\Delta t}, \qquad (8)$$

where P1 and P2 are two independent GPS fixes. The error terms $\varepsilon_{P1\text{-}gps}$ and $\varepsilon_{P2\text{--}gps}$ are the 1-D, along-line projections of the GPS position errors. Because each

measurement was calculated from two GPS measurements, the inherent uncertainty of the measurement was reduced by a factor of $\sqrt{2}$. Another factor contributing to the low GPS uncertainty was the use of overlapping positions to determine the ship's velocity. Increasing the time period between the measurements decreased the uncertainty of the velocity estimate. This was equivalent to smoothing the velocity measurements.

Up to this point, all error measurements have been specified in units of meters per shot. This notation was actually only a means of identifying these errors as relative positional errors between a set of two events rather than as absolute position errors. If the quality of the navigation remained consistent throughout acquisition and if the navigation grid did not wander with respect to absolute coordinates, then the RMS deviation is a measurement of the certainty with which individual event locations are known relative to the navigation grid. The assumption of no grid wandering is reasonable for the static, land-based system; the Maxiran positions, therefore, can be considered known (relative to the Maxiran coordinate grid) to an RMS uncertainty of 5.1 meters. Distortions of the coordinate grid which might have occurred because of weather and temperature fluctuations have been neglected in making this generalization.

SOURCE NAVIGATION

No real-time navigation monitoring was performed on the seismic source array during the survey. The centerline distance from the Maxiran antenna to the

center of the source array was 38 meters. During navigation reduction, it was assumed that the cable dragging the source array was directly behind the ship and fully extended. The ship orientation was provided by the ship gyro. Because of the relatively small distance involved, it is unlikely that either assumption contributed significantly to the overall error.

RECEIVER NAVIGATION

To locate the receiver positions, I determined the configuration for the 96 channel, 3.3 km receiving array (the ship "streamer") using the smoothed readings of ten magnetic compasses positioned along the array. These readings provided the magnetic heading at locations along the streamer. The compasses were Syntron model 831 remote compass units with exponential time averaging. Real time electronic averaging was performed continuously within each compass to increase the confidence of the readings and reduce the magnetic error effects associated with acceleration of the streamer. The specifications for the compasses indicated a theoretical resolution of 0.1°. The positions of the source and the receivers were calculated relative to the ship position and were also translated to geographic coordinates. Between adjacent compasses, the streamer configuration was reconstructed by modelling it as a circular arc. Figure 12 illustrates the reconstructed streamer configurations for two consecutive shots which occurred before the ship was well on-line and the streamer had straightened.

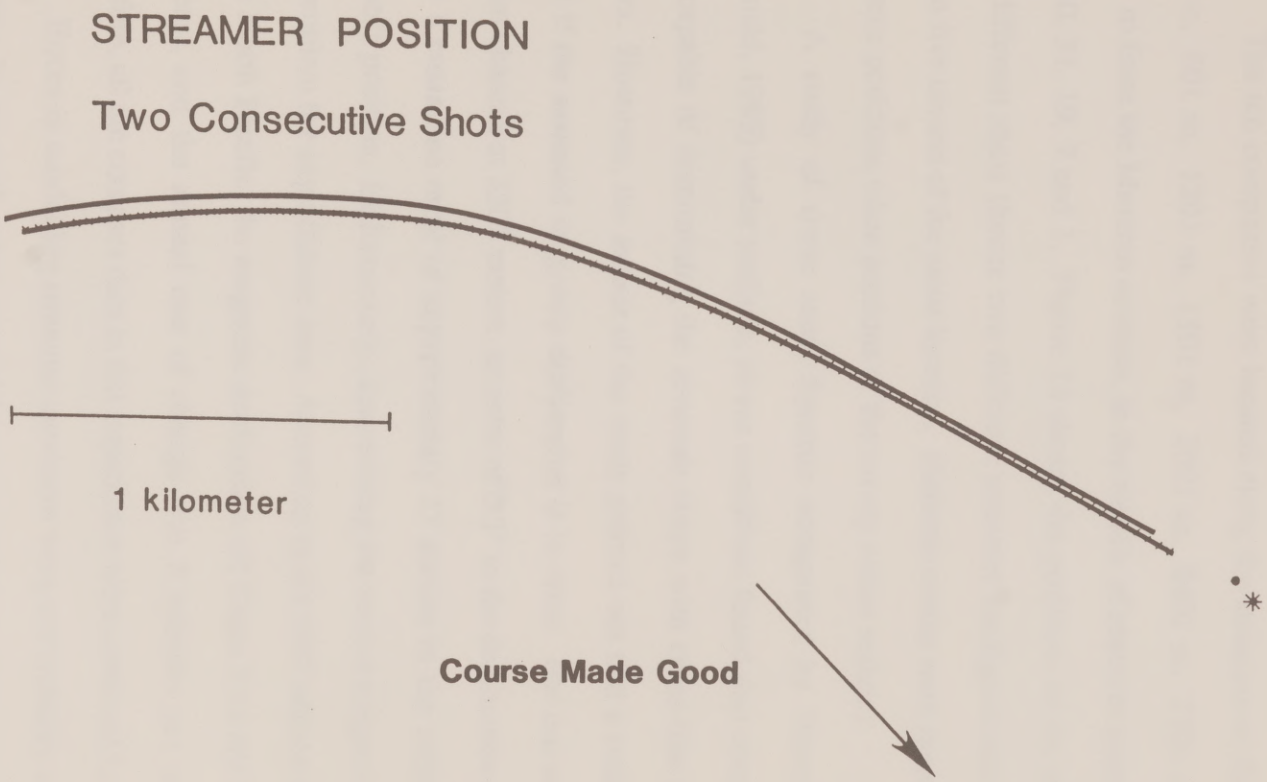

Figure 12. An example of streamer configuration, as determined by magnetic compasses, for two consecutive seismic events. The streamer had not yet straightened because the events occurred as the ship was coming on-line.

Compass Error

The ten compasses were located along the streamer at distances of 201 m, 401 m, 801 m, 1201 m, 1501 m, 2001 m, 2401 m, 2701 m, 3201 m, and 3301 m from the Maxiran antenna, in the middle of receiver groups 94, 91, 76, 67, 55, 40, 31, 19, 7 and 1. Figure 13 shows the positions of the ten compasses for two different shots (hence two different streamer configurations) which occurred within five meters of the same location. (Seismic events were recorded at essentially the same positions when portions of the survey where reshot.)

A study of these same Syntron compasses by Western Geophysical (Jubinski, 1985) under realistic, at-sea conditions found that compass information was capable of determining the streamer shape with cross-line errors of 5 to 10 meters. However, the author of the study pointed out that a serious problem will result if the assumed magnetic declination is in error. For our streamer, with the farthest channel at 3300 meters, an error of 0.3° in the declination correction would cause a cross-line error of approximately 17 meters in the estimation of the far channel's position. Unfortunately, determining the correct magnetic declination can be a problem for any offshore area. According to the 1987 edition of the Pilot Chart of the North Pacific, the magnetic declination off Costa Rica for Epoch 1985 was 3.6° east, and the annual rate of change was 8 minutes per year to the west. Therefore, all the compass data in this experiment were corrected by +3.3°.

Errors in modelling streamer curvature were not typically a major source of concern. In general, once acquisition was under way, the streamer was fully

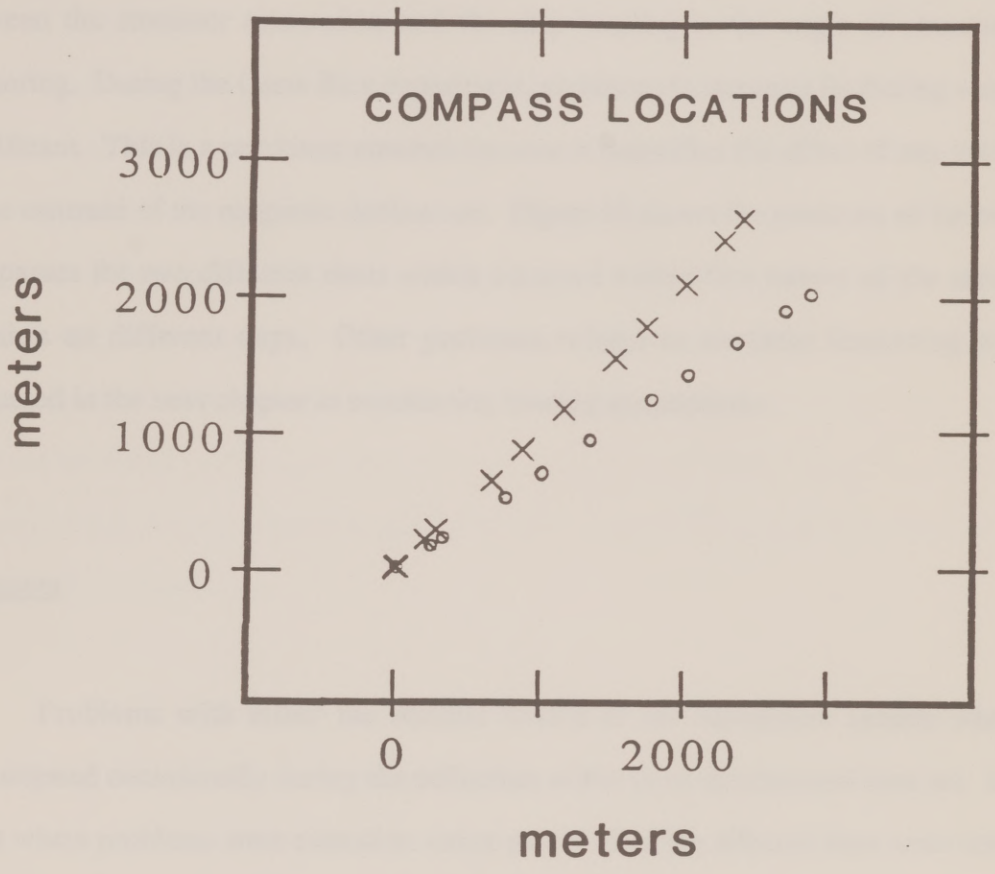

Figure 13. The ten compass locations, relative to the ship position at (0,0), for two seismic events. The second event, represented by the open circles, occurred three days after the first event, during an acquisition reshoot. The two events occurred within 5 meters of one another. The variation in the angle of streamer feathering is due to variations in the local current.

extended. When the range to the far receiver was calculated for the on-line events, streamer curvature was found to have shortened the range by an average of only 1.4 meters, with a standard deviation of 10 meters. However, the streamer was not necessarily extended parallel to the ship's path due to local currents. The angle between the streamer orientation and the ship heading is the angle of streamer feathering. During the Costa Rica experiment, variations in streamer feathering were significant. This is a persistent concern because it magnifies the effect of any error in the estimate of the magnetic declination. Figure 13 shows the positions of the ten compasses for two different shots which occurred within five meters of the same location on different days. Other problems related to streamer feathering are discussed in the next chapter in considering binning assumptions.

Reshoots

Problems with either the seismic source or the navigation system were encountered occasionally during the collection of the three dimensional data set. In areas where problems were extensive, either part or all of the affected lines were later reshot to insure the data quality. Where the entire acquisition line was reshot, the data from the first run was discarded and no further processing was required. In four instances, however, seismic collection was repeated for only some section of the line. In all four reshoots, the collection continued to the end of the line, so only one splice was required to replace the original data.

Two concerns arose when splicing together line segments which were not time sequential. The first was whether the ship positions for the original and reshot lines were actually coincident. For all four cases, the navigation records recorded the ship positions at the location of the splice as differing by less than 10 meters in the cross-line direction and less than 5 meters along the direction of acquisition.

The second concern dealt with discontinuities of seismic fold at the splice points due to differences in the angle of streamer feathering. Plots of the streamer positions at the splices (Figure 13) graphically display these tears. The far offset receivers in Figure 13 display a separation of approximately 800 meters. The effective displacement at any offset was approximately half of the apparent offset since only source-receiver midpoints were actually of concern. Streamer feathering affected the CMP fold at more than just these four splice points. Variations in the streamer feathering throughout acquisition affected the CMP fold of the whole data set, as will be shown later.

SUMMARY

This chapter documented the navigation systems for the Costa Rica survey and presented a through analysis of the navigational precision. The comparison of the independent land-based and GPS systems demonstrated that each shot was located relative to other shots in the grid with a 2-D RMS uncertainty of not more than 5.1 meters. The location of the 3-D survey area within line-of-sight of the shoreline was the single most important aspect in achieving this high level of

precision. By combining this excellent navigation with good ship maneuverability, seismic events were located using real-time ship navigation in accordance with the survey plan. During the post-acquisition processing, locations were assigned to the receiver and CMP positions. Given the proven reliability of magnetic compass measurements, it can be assumed that receiver positions relative to the ship were located to within 20 meters of their true cross-line positions. The next chapter will show that other processing assumptions were more significant sources of spatial smearing than errors in the navigation.

Chapter 3: Common Midpoint Binning

The final step in the navigation processing was assigning each seismic trace to a common midpoint, or CMP, bin. In the course of processing the raw navigation, I assigned geographical positions to the source and all receivers for all seismic events. Based on these positions, every seismogram collected during the Costa Rica experiment was assigned a source-receiver midpoint coordinate. In this way, each seismic trace was associated with a single geographic location for subsequent processing. It was then possible to define a regular two dimensional grid over the survey area and sort the seismograms into bins on the basis of their midpoint coordinates. Normal moveout (NMO) corrections were then applied to all traces in the data set. NMO corrections were made on the basis of the source-receiver offset of each trace and the RMS velocity function at its CMP position. After NMO corrections had been applied, all traces within a CMP bin approximated the zero-offset acoustic response of the Earth at that location. Those traces were then summed to produce a single seismogram with an excellent signal-to-noise ratio. A NMO corrected CMP gather from the Costa Rica grid data is shown in Figure 14.

For a three-dimensional survey, the choice of bin size has a direct influence on the fold coverage and the spatial resolution of the resulting image. The bin size must be small enough to provide adequate spatial resolution during stacking and subsequent processing, but there must be a sufficient number of traces in each bin to ensure an adequate signal to noise ratio in the final processed data. Also, a reasonable range of source-receiver offsets must be included in each bin. All six

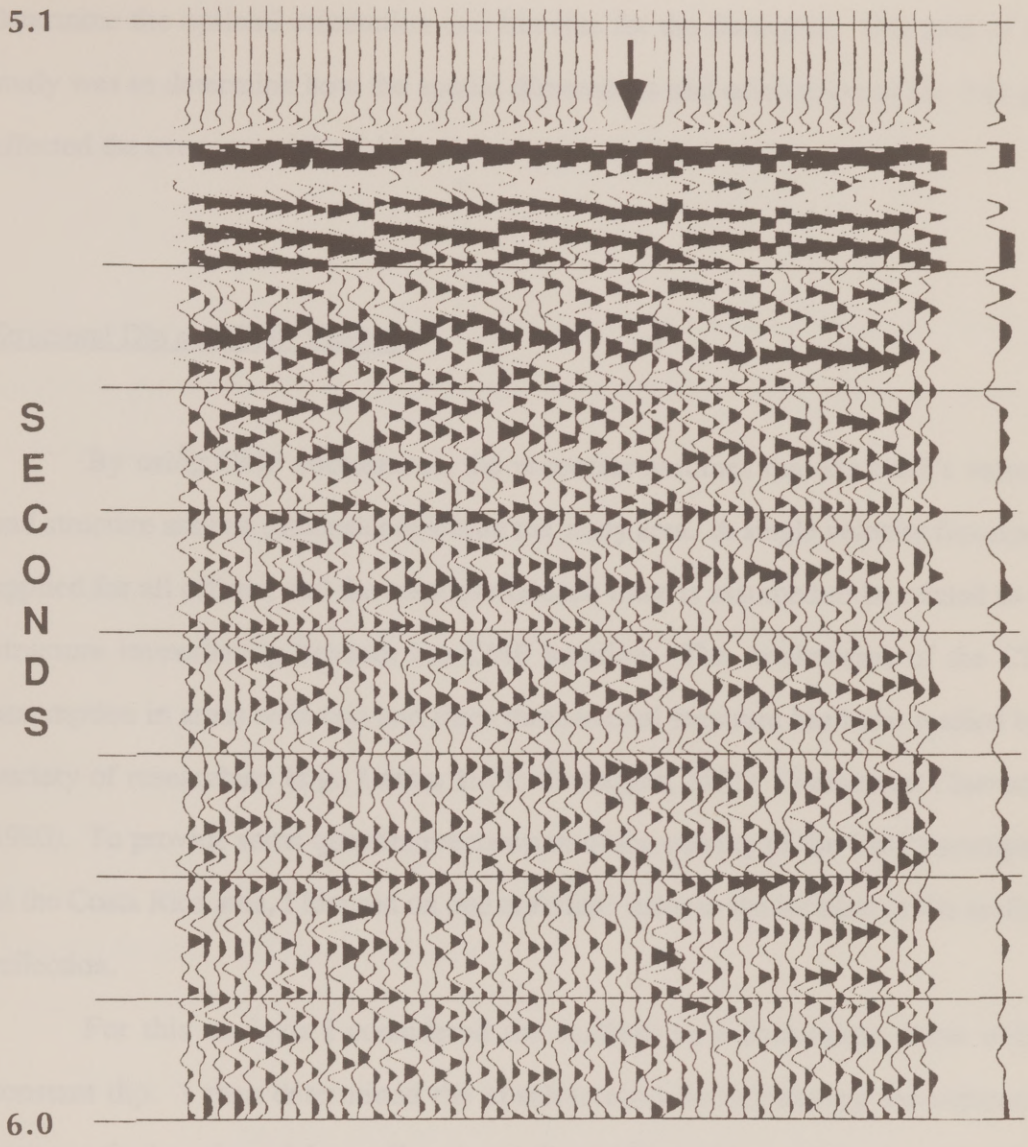

Figure 14. CMP gather from bin line 122, CMP bin 203. Seismograms are ordered by offset, with near offsets on the left, and are displayed after NMO. The checkered appearance of the seafloor is due to the intermingling of seismograms with similar offsets from different acquisition lines. The far right trace is the CMP stack.

million shot-receiver midpoint positions were binned into a variety of trial grids to determine the optimal orientation and bin size for the final grid. The goal of this study was to determine how the spatial dimensions and orientation of the 3-D grid affected the evenness of the fold.

Structural Dip and CMP Validity

By using CMP coordinates, the processor assumes that the earth's velocity and structure are one dimensional within the study area. A single velocity function is applied for all offsets, and the response of each trace is assumed to be related to the structure immediately beneath the CMP location. The weaknesses of the CMP assumption in areas with two and three dimensional structure has been studied by a variety of researchers (e.g., Levin, 1971; Sattlegger, 1975; Yilmaz and Claerbout, 1980). To provide some quantitative measure of the validity of the CMP assumption in the Costa Rica area, I focused on one criterion: error in the location of the seafloor reflection.

For this analysis I considered the seafloor as a featureless plane with a constant dip. I then determined the absolute error by calculating the separation between the location of the seafloor beneath a CMP position and the location of the seafloor reflection point for a source-receiver pair with that CMP position. The relative error was determined by observing the way this absolute separation changed with source-receiver offset and streamer configuration. I first assumed that all source-receiver pairs fell along a line parallel to the dip of the seafloor. For a single

dipping reflector, Jain and Wren (1980) described the horizontal offset between the source-receiver midpoint and the reflection point by

$$X_{OFF} = \frac{X}{2} - Z \tan\left(\frac{1}{2}\left\{\tan^{-1}\frac{X}{2Z} + \sin^{-1}\left[\sin\left(\tan^{-1}\frac{X}{2Z}\right)\cos 2\alpha\right]\right\} - \alpha\right), \quad (9)$$

where X was the source-receiver offset, Z was the depth at the source-receiver midpoint, and α was the dip of the seafloor (Figure 15). The offset X_{OFF} is always in the up-dip direction.

Reflector Dip	CMP - Reflection Point Offsets		Difference
1.5°	86.5 m	108.0 m	21.5 m
3.0°	173.0 m	216.0 m	43.0 m
4.5°	259.9 m	324.1 m	64.3 m
6.0°	347.0 m	432.4 m	85.3 m
Source-Receiver Offset:	170 m	3330 m	

Table 5: CMP - reflection point offset for dipping plane reflectors. The depth to each reflector at the CMP position is 3.3 km.

Table 5 includes calculated values of X_{OFF} for a range of parameter values. In this demonstration, I used a depth Z of 3.3 km, which fell midway between 2.2 km and 4 km, the extreme values for the seafloor depth in the Costa Rica grid area.

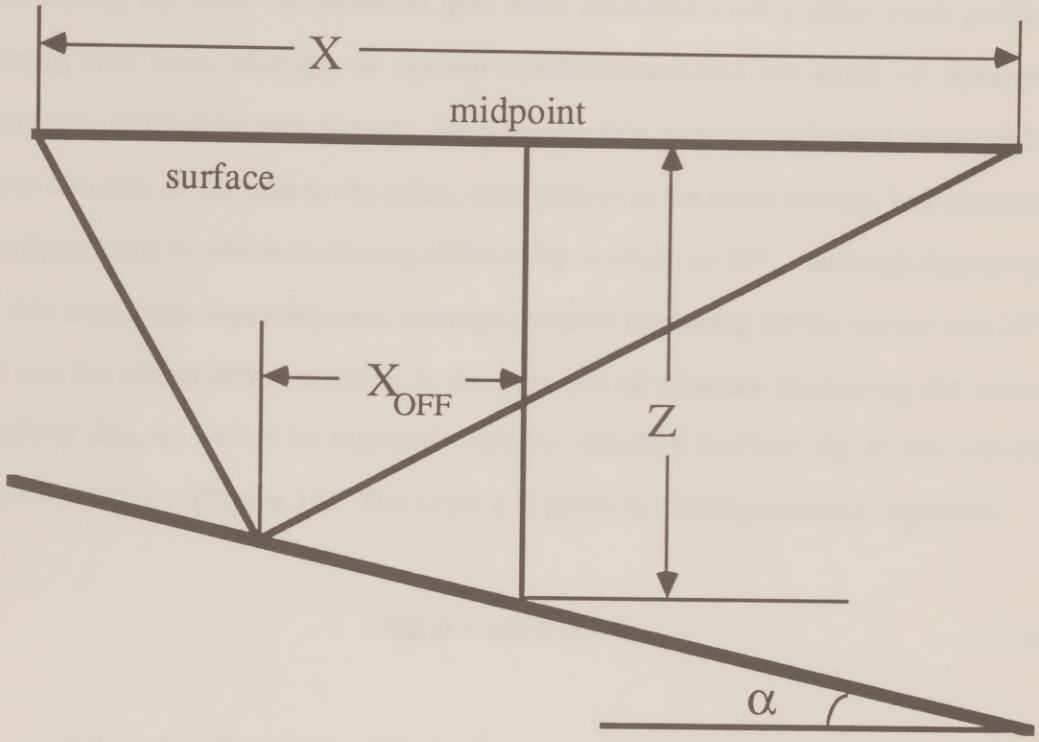

Figure 15. Definition of variables used in equation (9). After Jain and Wren (1980).

The source-receiver offsets used, 0.17 and 3.33 km, were representative of the near and far offsets collected. Four different seafloor dips were used. In the vicinity of the Costa Rica survey, the dip of the seafloor averages 4.5°.

Streamer feathering introduced an additional complication. (Feathering is the deviation of the streamer from the acquisition profile line.) The seismic data comprising the three-dimensional grid were collected over a three week period. During that time, changes in current conditions caused the angle of streamer feathering behind the ship to vary. Because the data were not collected sequentially from one side of the grid to the other, shot gathers in the same vicinity had streamer configurations in which feathering differed by as much as 25°. Although feathering of this magnitude was fairly rare, average streamer feathering for the survey was 13°. To use the above offset equation in the presence of streamer feathering, the actual seafloor dip, α, had to be replaced with the apparent seafloor dip in the source-receiver plane, ρ (Figure 16). The angle ρ is given by the trigonometric equation:

$$\tan \rho = \tan \alpha \cos \phi. \qquad (10)$$

When the effect of streamer feathering was considered, the horizontal offsets between CMP positions and reflection point positions contained both strike and dip components. This greatly increased the spatial smearing over the case where no feathering was present. A "worst case" scenario for the Costa Rica data is shown in Figure 17. Seafloor reflection points were calculated for four traces which shared a common source-receiver midpoint. Streamer feathering angles of 0° and 25° were

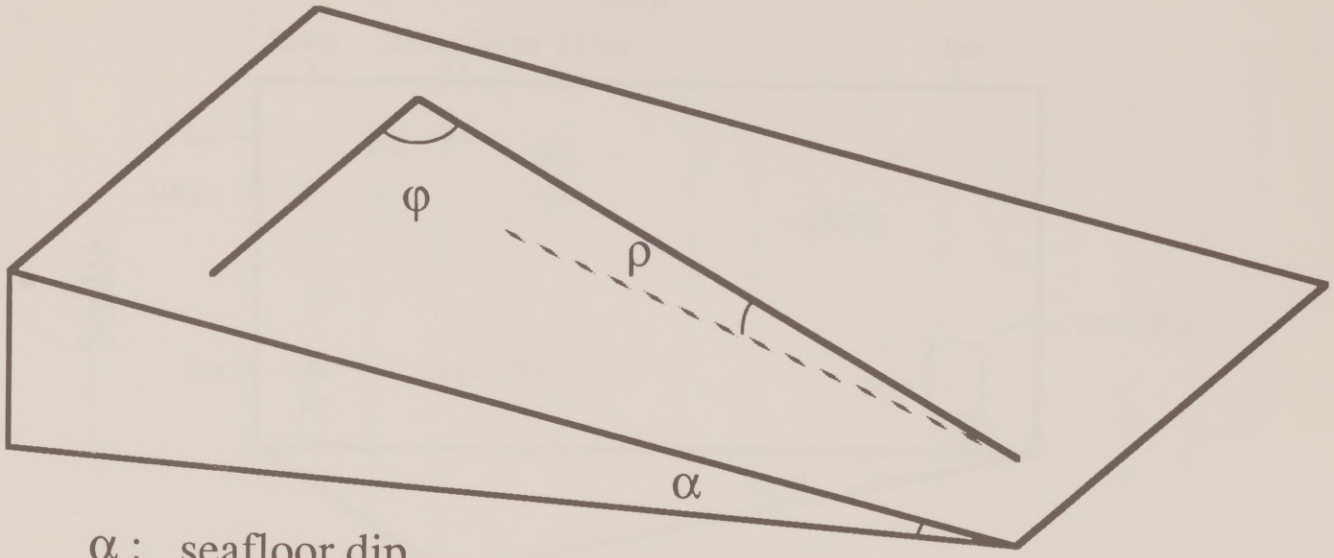

α : seafloor dip

φ : acute angle between strike and streamer

ρ : apparent dip

Figure 16. Relation between apparent dip (ρ) and actual dip (α).

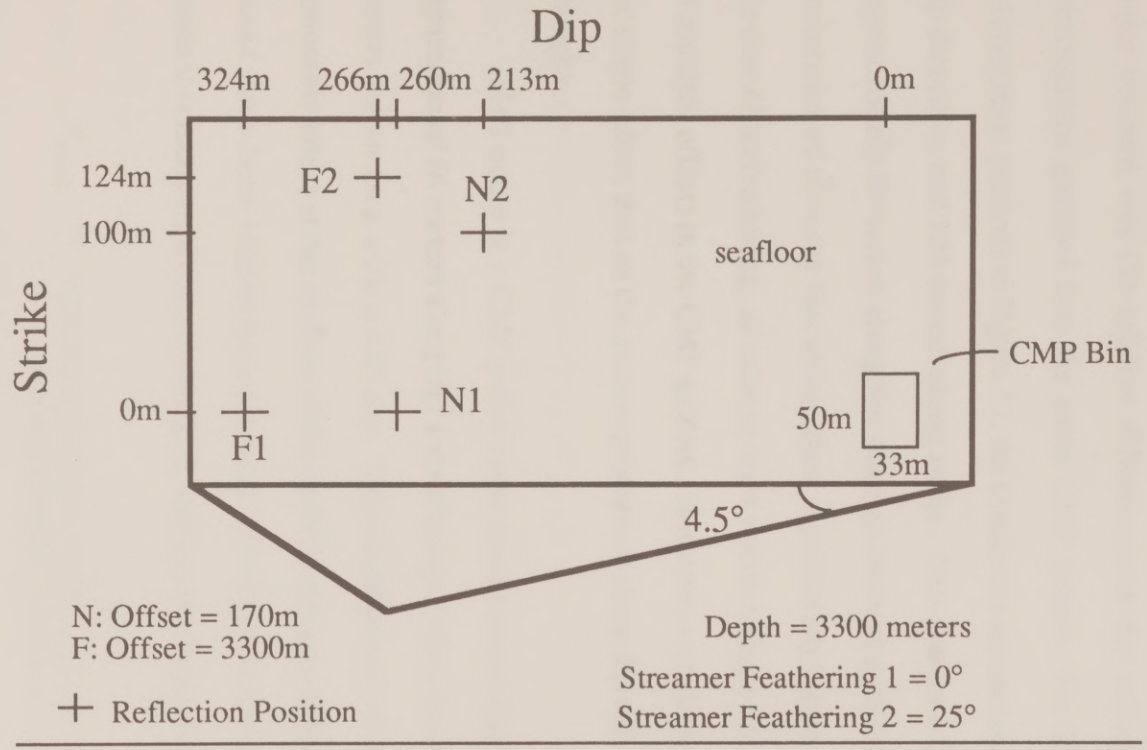

Figure 17. Horizontal offsets between CMP positions and reflection point positions. This simplified geometry models the seafloor as a featureless plane with a 4.5° dip, overlain by a constant velocity medium. The positions indicated are reflection points for source-receiver pairs whose CMP positions are all centered in the CMP bin at the right. For source-receiver pairs with reflection points at N1 and F1, the streamer was oriented parallel to the dip of the plane. For source-receiver pairs with reflection points at N2 and F2, the streamer was skewed 25° from the dip orientation.

used. For both orientations, source-receiver offsets of 0.17 kilometers and 3.33 kilometers were investigated.

Because the goal of this survey was to image a three dimensional data set, the major concern was the relative differences in the reflection point positions of seismograms grouped into the same CMP gather. For the locations of the four seismograms pictured in Figure 17, the maximum separations were 111 meters in the dip direction, and 124 meters along strike. This compared to a maximum value of approximately 64 meters along dip when no feathering effects were considered. The occurrence of streamer feathering, then, significantly increased spatial smearing. In the case of no feathering, all relative error within a single bin was due to the inclusion of multiple offsets in the CMP gathers. However, a gradational smearing does occur for single-offset data as the section progresses along dip and the depth to the seafloor changes.

If all traces in a CMP gather came from a single acquisition line, a horizontal separation of 64 meters along dip would be equivalent to a difference in height of 5 meters for an area with a 4.5° dip. This discrepancy would not have produced a noticeable effect at the seafloor if the seafloor dip was relatively constant because it would have been hidden by a stacking velocity correction (Levin, 1983). For a constant velocity medium, this stacking velocity is related to the true velocity by

$$v_{stack} = \frac{v}{\sqrt{1 - \sin^2\alpha \cos(\pi-\phi) \left[2\cos(\phi-\pi) - \cos(\pi-\phi) \right]}} , \qquad (11)$$

where the angle (π-ϕ) was the angle of streamer feathering. (α and ϕ are still the actual seafloor dip and the apparent seafloor dip, respectively.) Equation (11) assumes that the direction of acquisition is parallel to the direction of dip.

To extend this analysis to the subsurface, several effects must be considered. Inspection of equation (9) shows that the CMP-reflection point separation decreases as the source-receiver offset to reflector depth ratio decreases. The relative separation between reflection points for near and far offsets also decreases, so the CMP assumption introduces more errors into shallow structures than deep structures for similar geometries. In addition, deeper structures are usually defined by a relatively low frequency content, and therefore a relatively low seismic resolution. Reflection mislocations at the base of the prism complex, then, probably were not as severe as at the seafloor. Even if the errors had been as severe, they would have had a less pronounced impact because of the relatively coarser resolution. In this region, poor velocity constraints were a more significant concern than CMP smearing because velocity errors may have introduced structural distortions during poststack migration.

By contrast, the top of the prism is less than a kilometer beneath the seafloor in most of the survey region, and the frequency content of its reflections are still relatively high; the above arguments are not valid for this surface. Furthermore, the high incidence of both normal and thrust faulting have produced significant variations in the dip of the prism surface. Because its surface is much rougher than that of the seafloor, there is less validity in modeling it as a simple plane. However, given the structural variability and the inclusion of significantly higher dips than are present at the seafloor, it is intuitive that reflection point mislocations were at least as great at the prism surface as at the seafloor, and were probably more severe.

The foregoing discussion helps explain the statics problems displayed by the moved-out CMP gather in Figure 14. The "checker board" appearance of the seafloor, as indicated by the arrow, occurred where adjacent seismograms with similar offsets were from different acquisition lines with different angles of streamer feathering. In the stacked data, these static shifts resulted in broader reflectors with a lower frequency content than before stack. This problem is an inherent shortcoming of the CMP assumption in areas with structural dip. Because trace-by-trace statics solutions proved ineffective in improving the data, no systematic static corrections were applied before stack.

Bin Size and CMP Fold

Three-dimensional histograms provided a visual representation of how the fold distribution varied with the choice of bin size for both the full ninety-six and the near six channel data. The results of trial binnings with four bin sizes are shown in Figures 18 and 19. The first dimension of each of the bin sizes is along the direction of dip, and the second dimension is in the cross-line direction. The fold histograms can best be explained with an example using the six channels comprising the near offset subset of the seismic data. The six receiver subset of the data was comprised of approximately 350,000 seismograms, each of which had been assigned a CMP. The result of binning these positions within a grid comprised of 16 $^2/_3$ meter by 50 meter bins is shown by the back row of Figure 18. 71,000 bins contained three

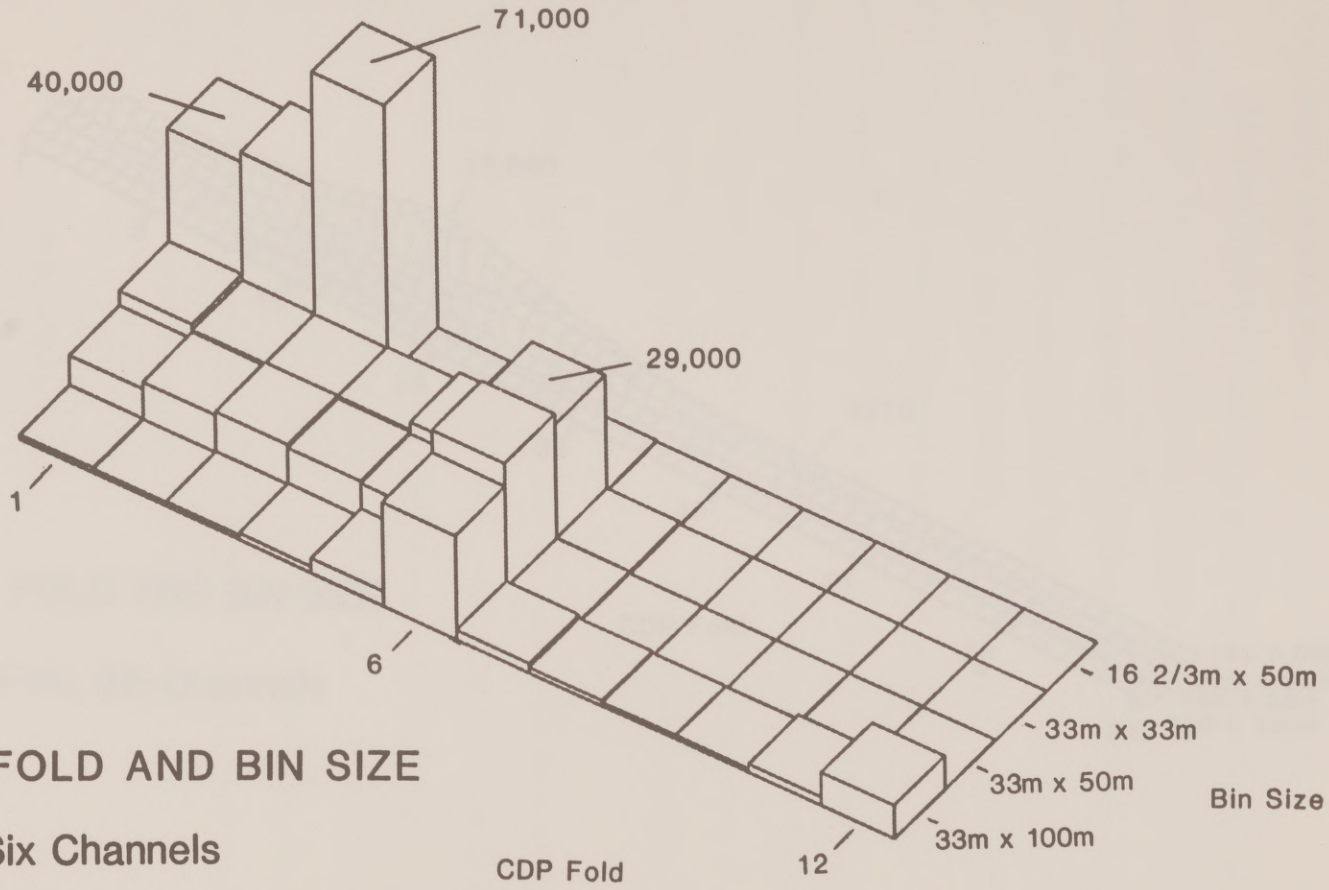

Figure 18. Three-dimensional histogram illustrating the theoretical folds for trail binnings of the near 6 offsets of the 3-D data set. The histogram shows the occurrence of particular folds for various bin sizes. All grids were aligned parallel to the direction of acquisition.

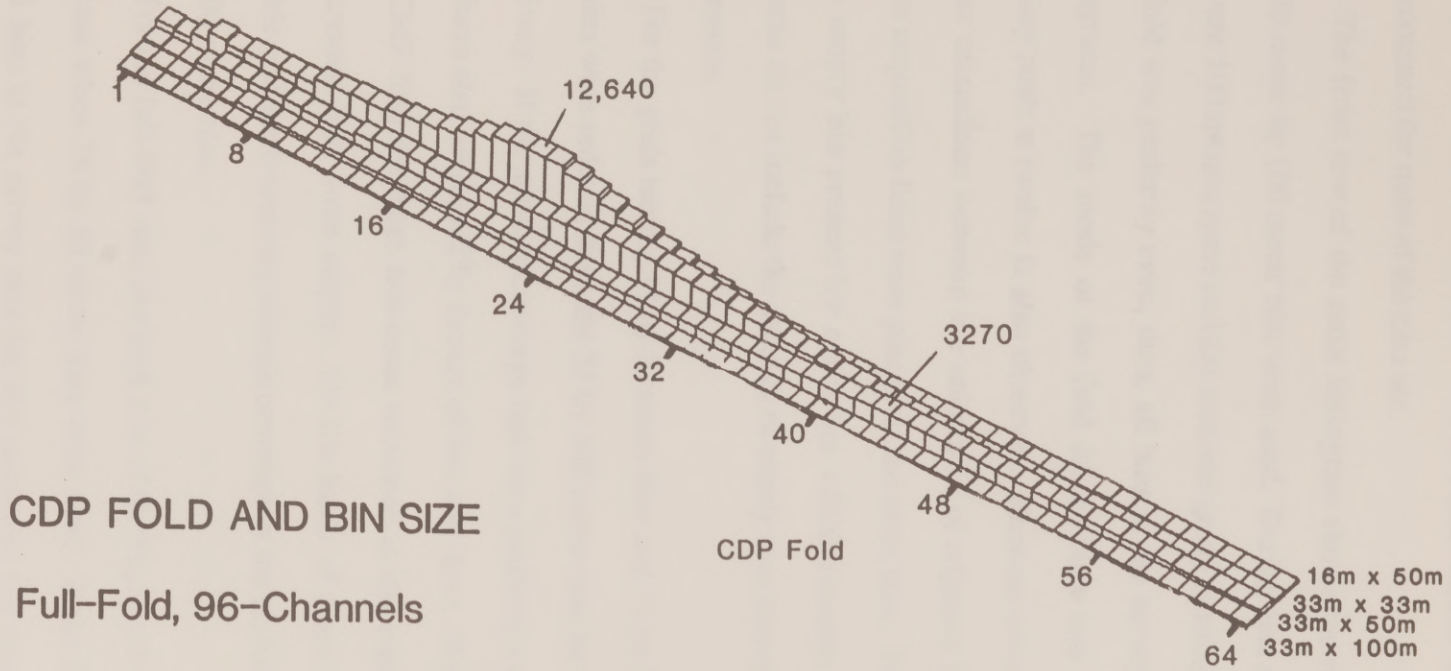

Figure 19. Three-dimensional histogram illustrating the theoretical folds for various trail binnings of the approximately 6 million traces composing the 3-D data set. The histogram illustrates the variation in fold for various bin sizes, with all grids aligned parallel to the direction of acquisition.

CMP's, 43,000 bins contained two CMP's and 40,000 bins contained one CMP. This accounted for most of the data set.

The front row of the same histogram shows the resulting fold distribution when 33 meter by 100 meter bins were used. During data collection, the acquisition lines were 100 meters apart and the receiver group spacing was 33.3 meters. If the CMP fold was perfectly even, then, all bins in the survey area would contain six seismograms. The mode of the fold distribution was six, as expected, but a secondary peak at twelve is also observed. Because oceanic currents changed the streamer orientation between the collection of adjacent lines, seismograms from adjacent acquisition lines were placed in the same bins. Within the grid area, there was an empty bin present for every bin which contains a fold of twelve. The histograms do not include the number of empty bins that occurred within each grid configuration.

For the grids having 33 by 50 meter bins and 33 by 33 meter bins, the widths of the bins were reduced from the 33 by 100 meter case by factors of two and three, respectively. If the seismic coverage had been perfectly even, the theoretical folds should have also decreased by factors of two and three. However, the actual modes of the CMP fold for these two cases remained at six, signifying that most of the newly created bins were empty. On the basis of these observations, the most reasonable grid for preserving seismic coverage in the six fold case was the grid with 33 by 100 meter bins.

For the full-fold case, the back row of the Figure 19 shows the resulting fold distribution when 16 by 50 meter bins were used. If the CMP fold was perfectly even, all bins in the survey area for this particular bin size would have contained

twenty-four seismograms. The mode of the theoretical fold distribution was actually twenty-two. Once again, the deviation of the theoretical fold from its expected value was the result of changes in streamer feathering. The average theoretical bin fold varied from 22 (for 16 by 50 meter bins) to 80 (for 33 by 100 meter bins). A 33 by 50 meter bin size was used for the final binning of the full-fold data set.

Grid Orientation

For the Costa Rica survey, the average orientation of acquisition was 44.9° northeast. To determine the sensitivity of fold to grid orientation, navigation positions were binned into six grids, with the CMP axis at angles of -5°, -1°, 0°, +1°, +5°, and +30° to the average orientation. For all six orientations, a bin size of 33 by 33 meters was used. Figure 20 shows that there was no significant difference in the character of the fold for any of the grid orientations between -5° and +5°. Even for the grid orientated along +30°, there were only slight changes in CMP fold. This observation was not limited to the full-fold data set; it also applied to groups of sixteen consecutive offsets. This attested to the evenness already inherent in the three dimensional multichannel coverage because of streamer feathering. The angle between the ship track and the streamer orientation varied from 0° to more than 20°. For an orientation of 10°, the difference in the off-line distance between the front and the end of a 500 meter section of the streamer (sixteen channels with a 33 meter group spacing) was 87 meters, which was practically equal to the line spacing.

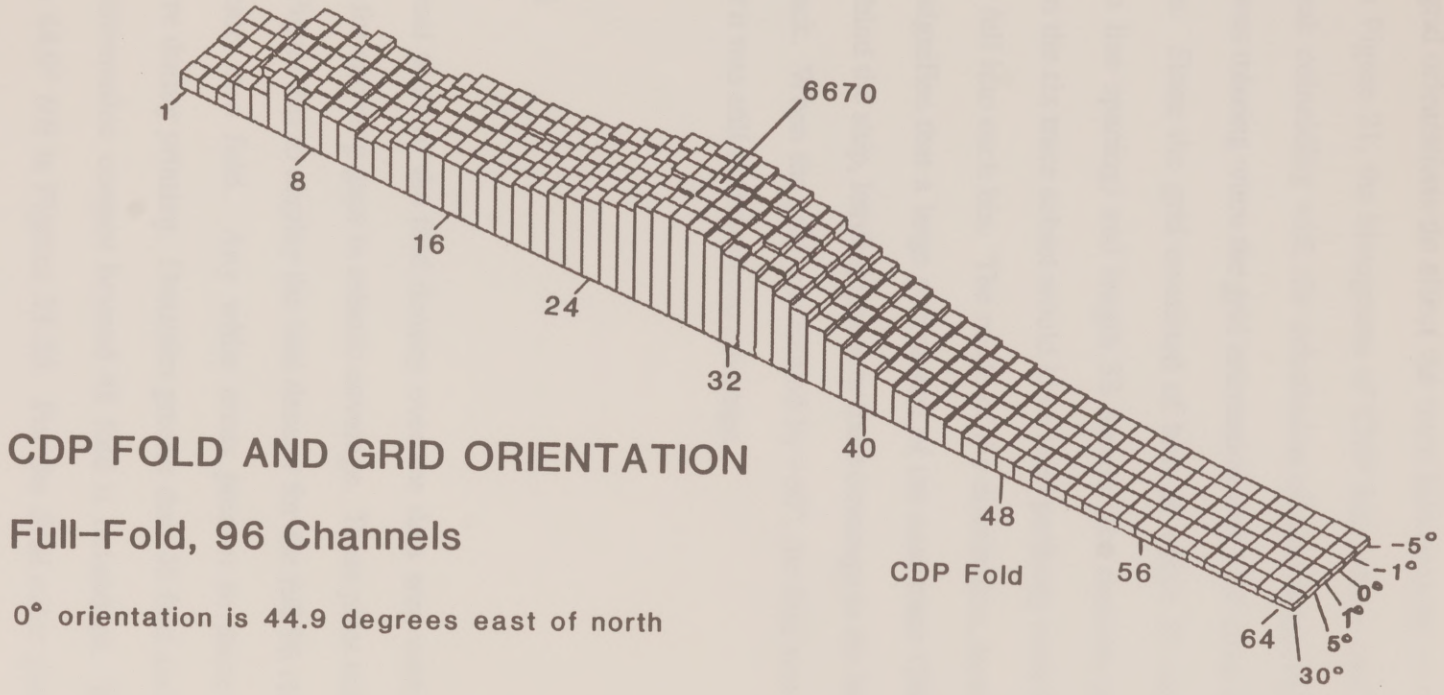

Figure 20. Three-dimensional histogram showing the occurrence of particular theoretical folds for trail grid orientations of the full fold 3-D data set. A constant bin size of 33 meters by 33 meters was used, and the grid was oriented at various angles oblique to the direction of acquisition, as indicated.

When the fold contribution of only the near six channels was considered, different grid orientations do affect the trace fold because of the shorter streamer length. In Figure 21, the histograms of CMP fold verses grid orientation show a distinct peak coinciding with the orientation of data acquisition. This unimodal character was missing when the grid orientation was +30° from the direction of data acquisition. Since the grid consisted of bins of width 33 meters (one third the acquisition line spacing) and length 33 meters (the receiver group spacing), the coverage in the six trace subset would have been perfectly even for the entire grid if two traces fell into each bin. The mode of the distribution, however, was a fold of six. This signifies that a large percentage of the near trace CMP's fell in the bins directly behind the ship, leaving less near trace coverage in the bins on either side of the ship track. When the grid was rotated by +30°, the fold was smoothed to some degree; but it was still far from even coverage.

Color Plots

Actual plots of the fold density over the data area were more useful than histograms for showing gaps in seismic coverage. These plots utilize the color scale provided (Figure 22) to display the fold density for the full 96 channel data. Black areas indicate zero fold. Any white areas present in these plots are due to overexposure during printing. Densities greater than 48 fold are not differentiated, since the information content beyond 48 fold is redundant. The positive CMP direction is 44.9° NE in Figures 23-26. For the final color plot (Figure 27), the

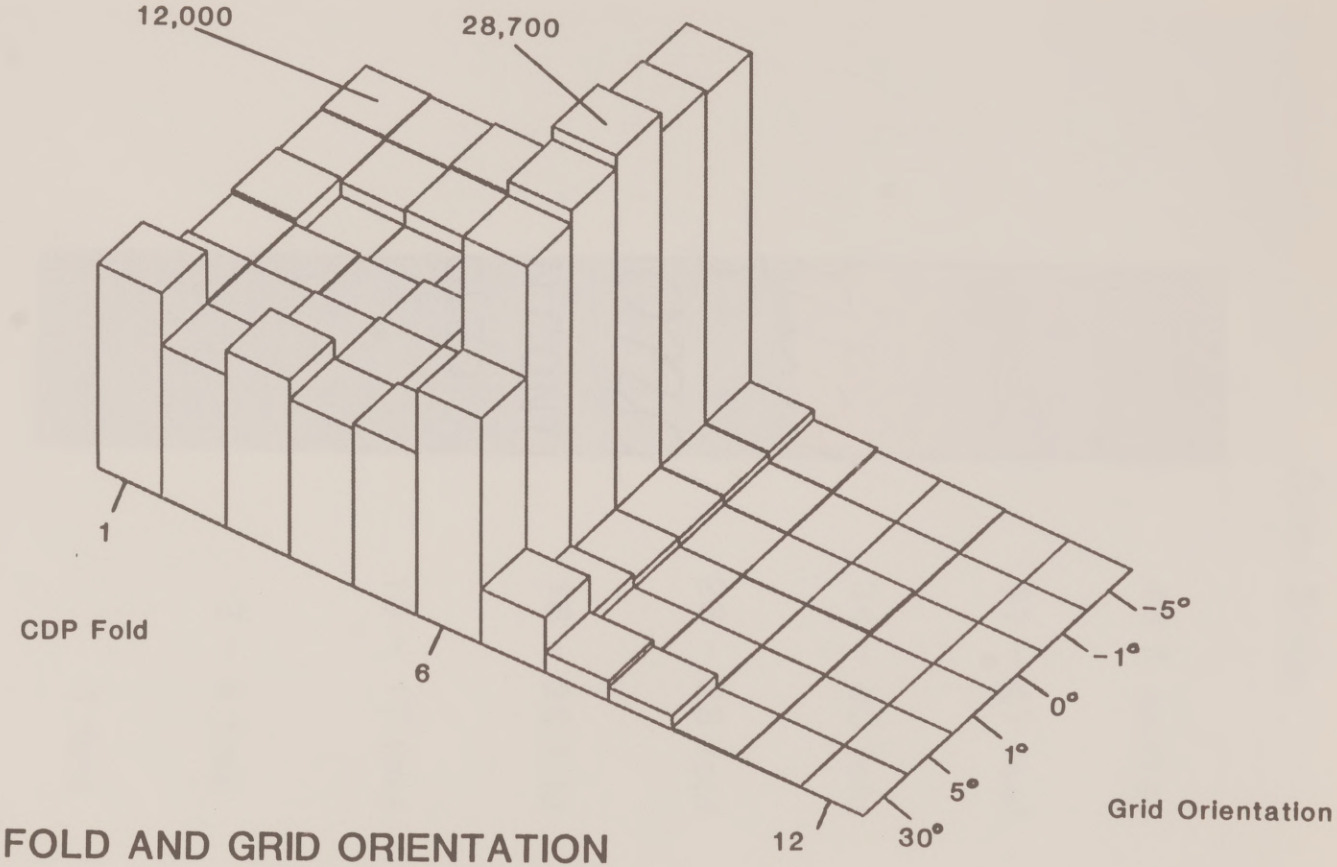

Figure 21. Three-dimensional histograms illustrating the theoretical folds for various trail grid orientations using the near six offsets of the 3-D data set. A constant bin size of 33 meters by 33 meters was used, and the grid was oriented at various angles oblique to the direction of acquisition, as indicated.

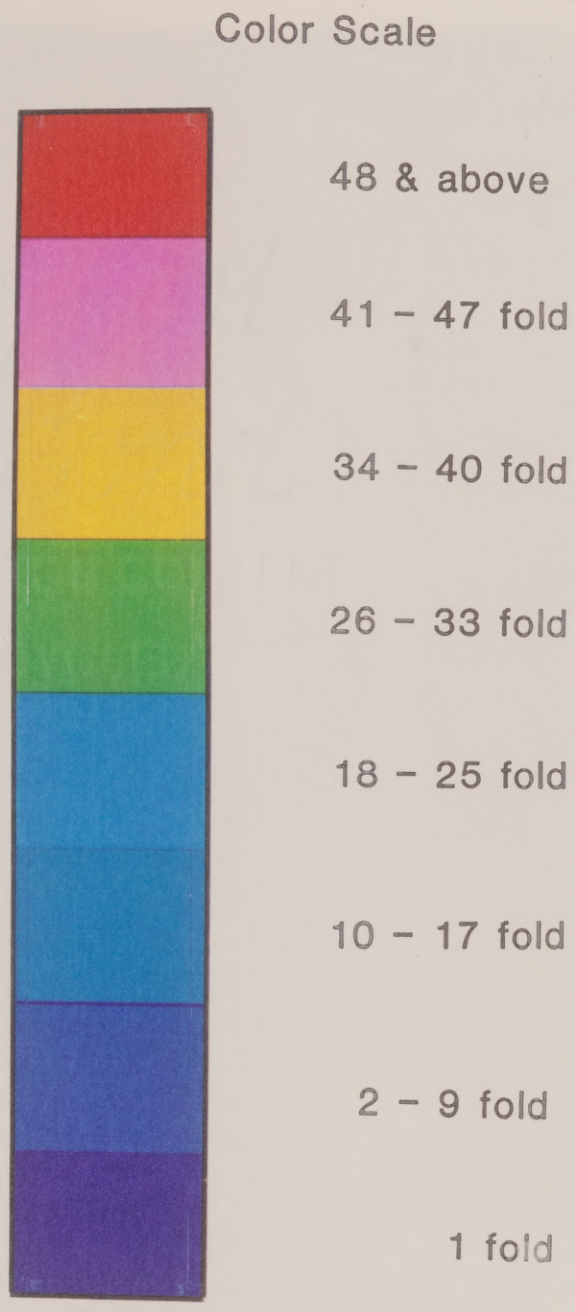

Figure 22. Color scale utilized to display fold densities for Figures 23-27. Densities greater than 48 fold were not differentiated.

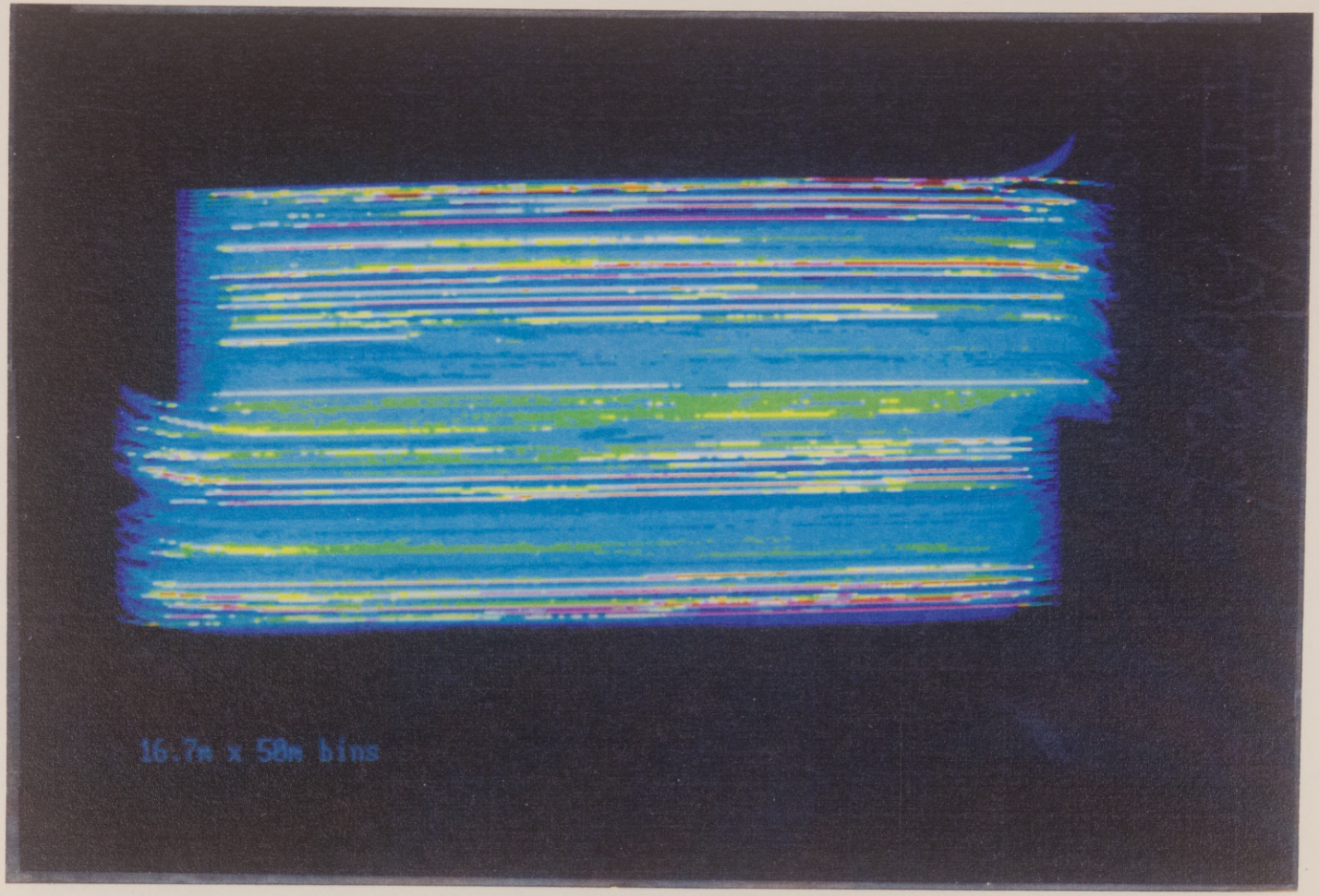

Figure 23. Fold density plot for trial grid using 16.7 meter by 50 meter bins. The grid orientation was 44.9° NE.

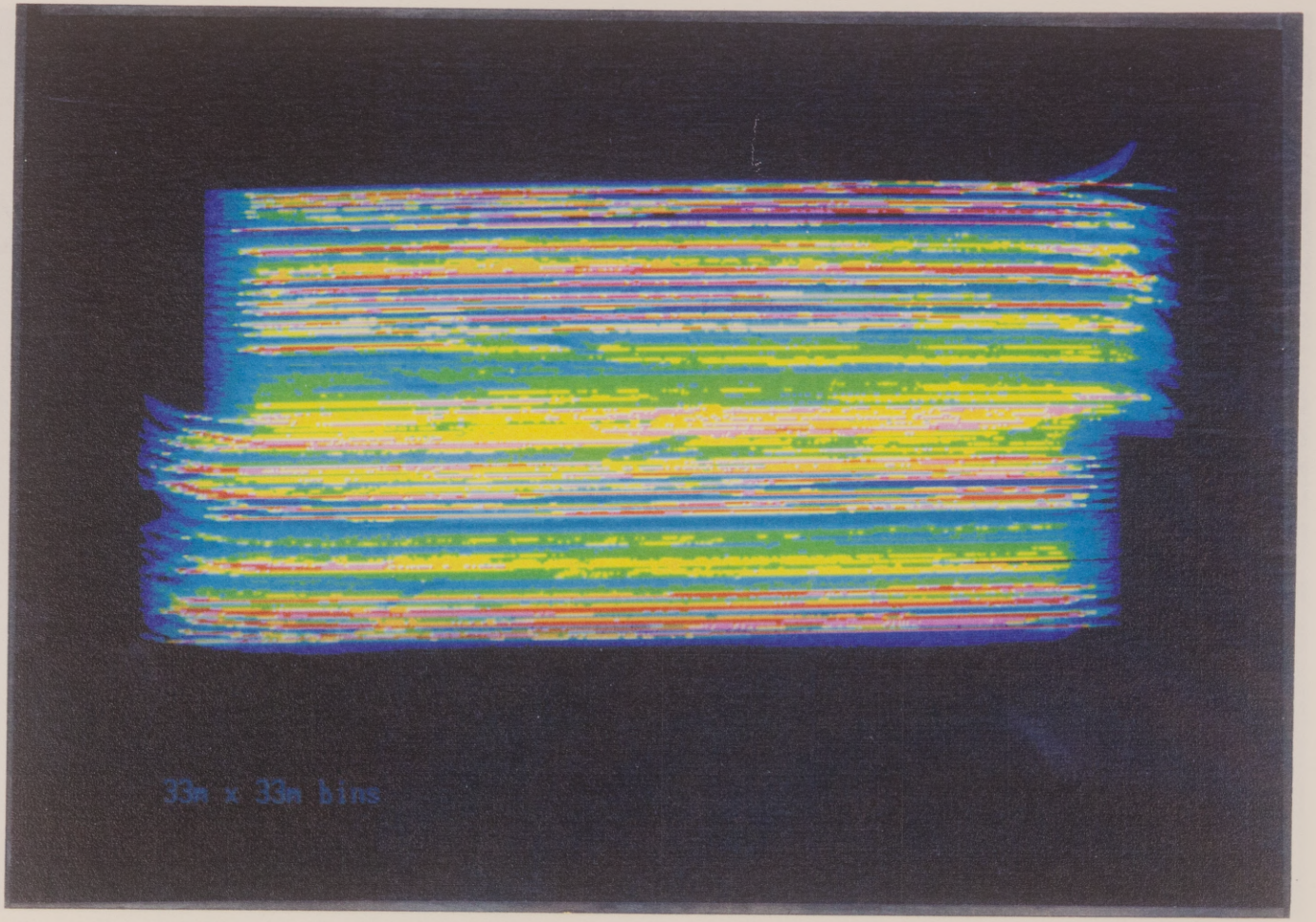

Figure 24. Fold density plot for trial grid using 33 meter by 33 meter bins. The grid orientation was 44.9° NE.

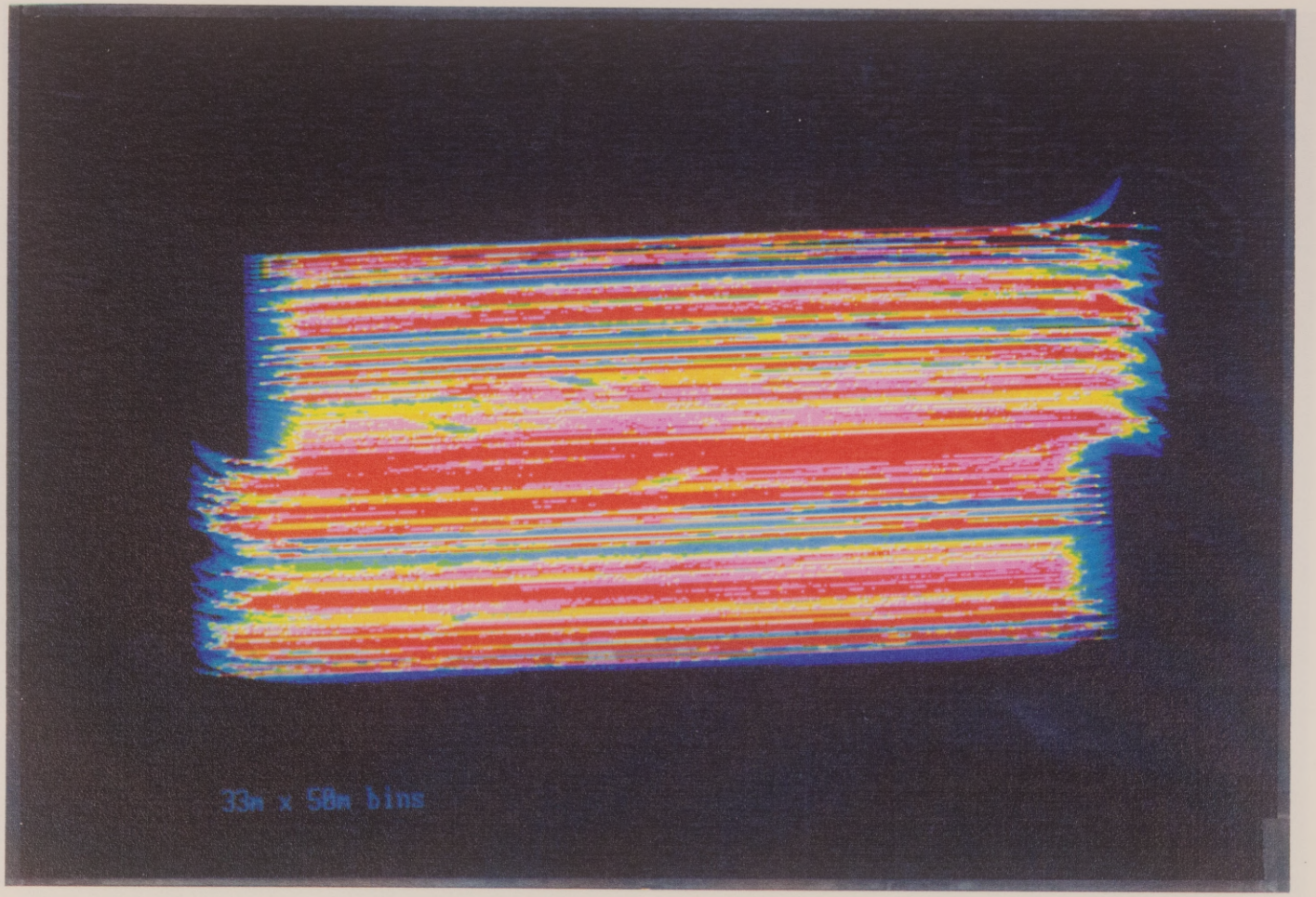

Figure 25. Fold density plot for trial grid using 33 meter by 50 meter bins. The grid orientation was 44.9° NE. This grid configuration was used for the final data binning.

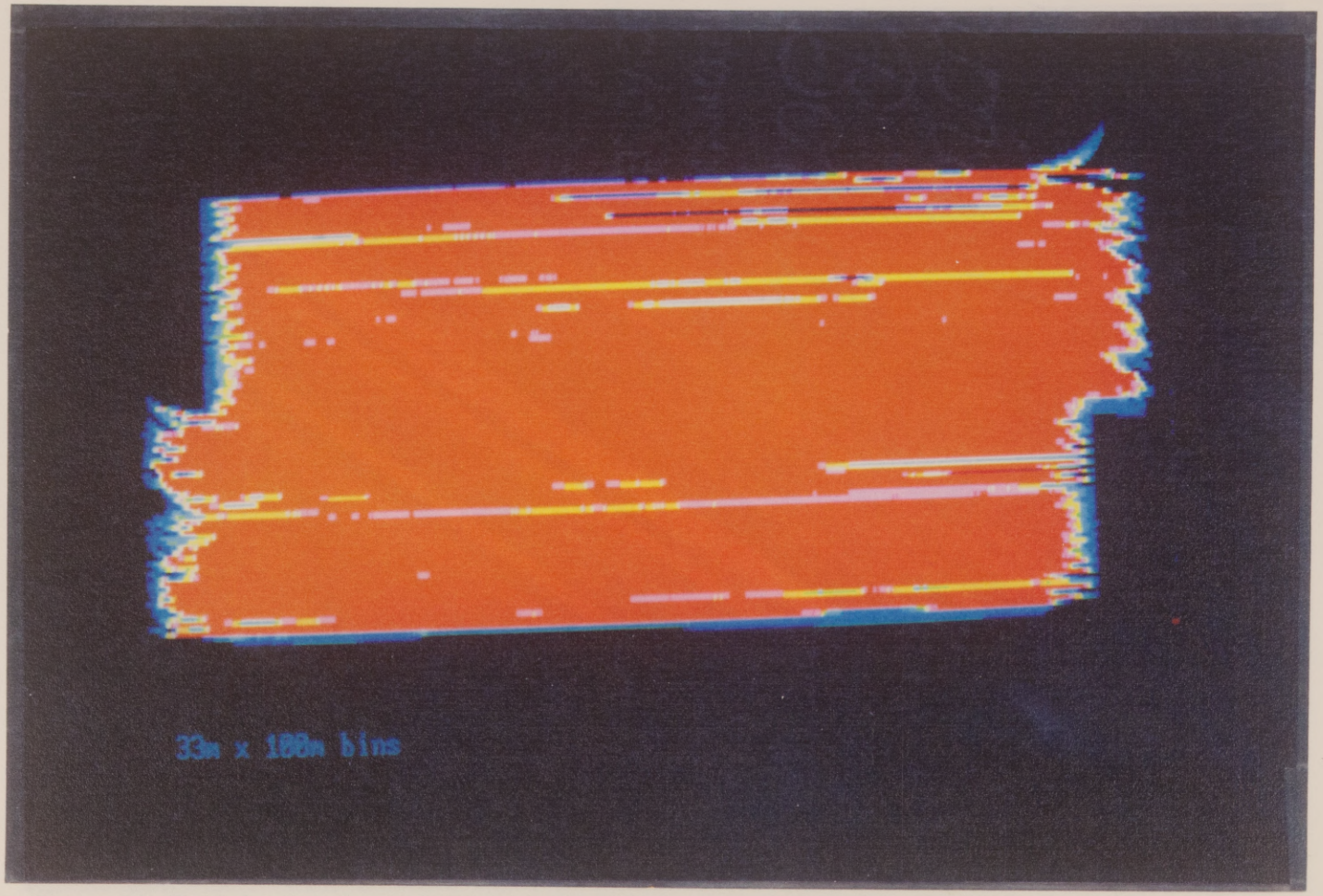

Figure 26. Fold density plot for trial grid using 33 meter by 100 meter bins. The grid orientation was 44.9° NE.

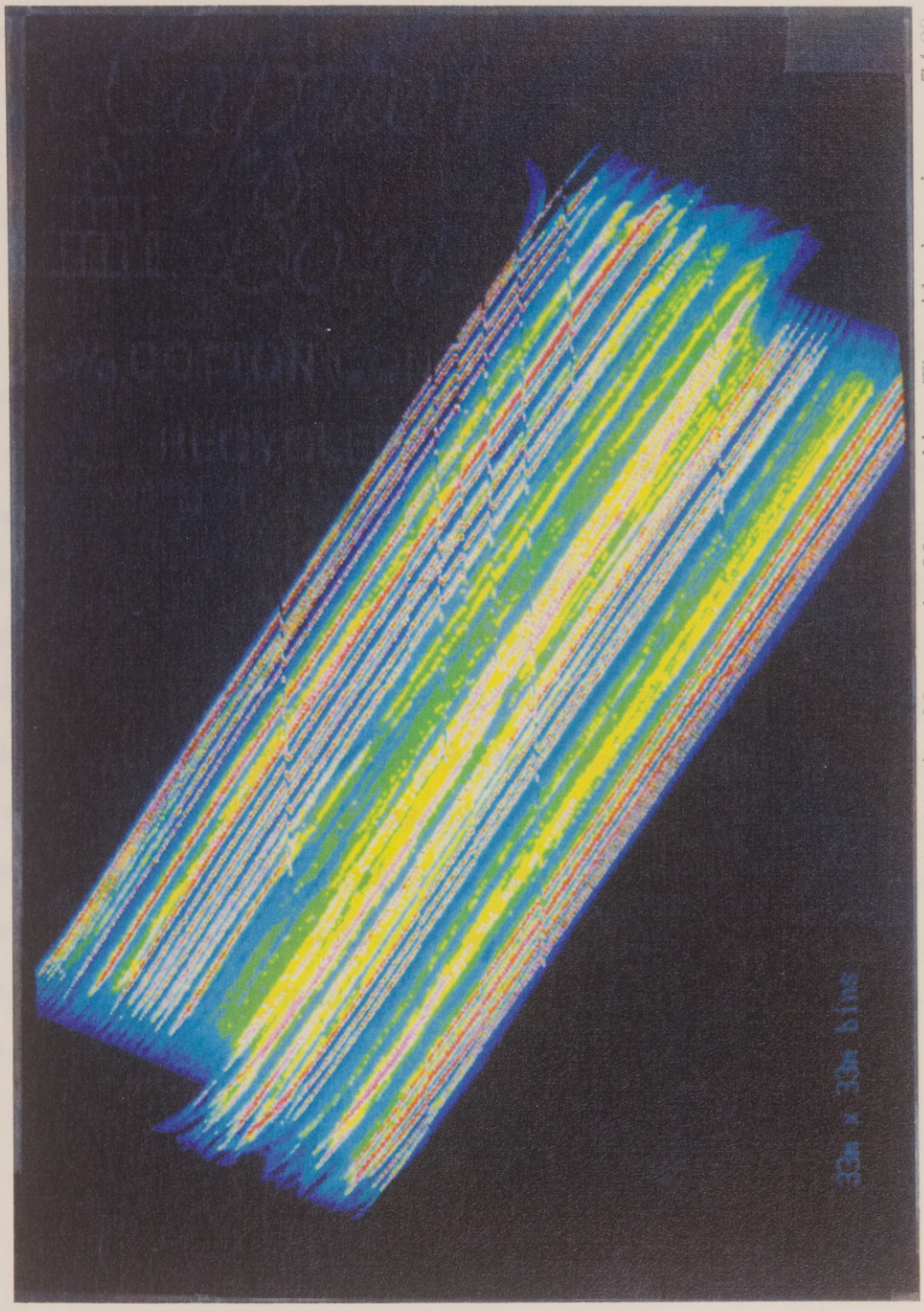

Figure 27. Fold density plot for trial grid using 33 meter by 33 meter bins. The grid orientation was 74.9° NE.

positive CMP direction is 74.9° NE. A visual comparison of the skewed grid with the other 33 by 33 meter bin size plot (Figure 24) demonstrates once again that grid orientation made a negligible difference in the full-fold case.

Bin Size and Image Resolution

For the final binning and stacking of the Costa Rica grid data, a grid with bin dimensions of 33 by 50 meters was used. The study of bin size and CMP fold found that this choice resulted in a CMP fold distribution with a mode of 43 (Figure 21). Examination of Figure 25 shows that this choice of bin size, though producing a reasonable average fold, left large areas of the grid with coverage less than 18 fold. (Figure 26 reveals that there are areas with cross line widths of 100 meters with zero fold.) A more extensive problem was the uneven offset coverage. Even bins with high fold were sometimes missing any representation of near, far, or middle offsets. To ensure that all areas had adequate fold and offset coverage, trace duplications were made during binning. Although the actual bin width was 50 meters, a fifty percent overlap was applied in the cross line direction, making the effective bin width 100 meters. This process spatially smeared the data, but the average fold of the grid was increased to 80.

Chapter 4: Migration and Imaging in Two and Three Dimensions

After 3-D binning of the seismic traces was completed, move-out analyses were performed to determine what velocities would achieve the best NMO and stack of the data. Stacking after NMO reduces the data in each bin to a single seismic trace which approximates the zero-offset acoustic response of the earth at that bin position. An advantage of stacking is that it greatly improves the signal-to-noise ratio of the data, bringing it closer to a form which can be easily interpreted. A velocity model for stacking was derived using both semblance analyses and constant velocity stacks (CVS's) of the data. Semblance displays were useful to the surface of the prism, beneath which CVS results were more easily interpreted. A semblance analysis was performed using 4 adjacent in-line bins every 2 km in the in-line and cross-line directions. CVS was performed on complete lines at 2 km intervals. Velocities were chosen which produced the best stack of the data, and little consideration was given to the geologic implications of the velocity model. As I discussed in the last chapter, these "best stack" velocities are not simply related to the geologic velocities.

In the present chapter, I am concerned with the imaging of the stacked data. The most important component of the poststack imaging process is wave equation migration. The first section of this chapter, therefore, is a discussion of the principles of poststack migration and an overview of the migration operation. In the next section, I show how some common numerical implementations are related to the acoustic wave equation, and I compare their advantages and disadvantages. I will

then introduce the Costa Rica data and demonstrate why poststack migration is necessary to improve its interpretability.

The structural complexity of this area makes proper imaging a difficult task. Migration methods which collapse diffracted energy can be classified as either time or depth migrations. In the fourth section of this chapter, I demonstrate why depth migration is required for imaging this accretionary environment by comparison to an equivalent time migration. The foremost emphasis of this chapter, however, is to compare and evaluate various aspects of 2-D and 3-D imaging. Towards this end, I survey the imaging advantages of 3-D acquisition and processing over 2-D techniques, and I describe various processing schemes that incorporate three dimensional information. The relative merits of all techniques are illustrated with examples from the Costa Rica data. I also examine 3-D migrations of the data performed with differing spatial resolutions and discuss how density of coverage affects the resolution of the migrated image.

Poststack Migration of Seismic Data

In exploration seismology, the presence of diffractions in the seismic data denote structural complications. The principles of physical optics stipulate that diffractions are created by changes in the velocity of the wavefront as it propagates through a region (Waters, 1987). The strength of the diffraction depends on the rate of change in the angle of reflection experienced by the wavefront along a reflection event. Either strong lateral variations in the velocity field or structures with sharp

edges will create diffractions. Consequently, diffractions are good indicators of complicated velocity gradients and non-planer geological structures. However, diffractions also obscure underlying and surrounding structures. They confuse the relation between neighboring reflectors, making it difficult to interpret reflection data collected over complex structures.

In addition to diffractions, the wavefield suffers other distortions as it propagates through structures with curvature and variable dip. From the perspective of a structural geologist, it is difficult to ascertain the significance of a reflection event which is not correctly positioned relative to other events in the data volume. To produce data that are more readily interpretable, it is possible to transform the CMP stacked data (which are assumed to be zero-offset) by means of a poststack migration operator. Migration improves the interpretability of seismic data by properly positioning dipping reflectors, by correcting distortions due to reflector curvature, and by collapsing diffractions to their apex. That the migration operation acts to collapse diffractions is an indication of its ability to exploit the spatial coherence and improve the resolution of seismic data.

All poststack migration procedures can be derived from the Helmholtz equation (e.g., Larner and Hatton, 1977). The Helmholtz equation, also known as the constant-density acoustic wave equation, is the second order partial differential equation given by

$$\frac{\partial^2}{\partial z^2}\psi + \frac{\partial^2}{\partial x^2}\psi - \frac{4}{v^2}\frac{\partial^2}{\partial t^2}\psi = 0 \, . \tag{12}$$

In equation (12), $\psi = \psi(x, z, t)$ represents the seismic wavefield and v is the velocity structure of the medium through which it propagated. Equation (12) could be easily generalized to the 3-D case by adding to the left hand side an additional second partial derivative of the wavefield with respect to y. For notational simplicity, I will only work with the 2-D case here.

The factor of two squared in the third term of (12) is a consequence of the use of the exploding reflector model (Lowenthal et al., 1976), which forms the basis of most poststack migration algorithms. The primus of this model is that stacked data can be treated as measurements collected at the surface after an explosion of all subsurface reflectors at time t=0. In the exploding reflector model, the distance between the "source" and receiver is half the distance for the zero-offset case, so exploding reflector velocities are defined as half the actual seismic velocities. Adopting this model greatly simplifies the development and implementation of poststack migration algorithms, since it is only necessary to correct for one-way wave propagation during migration.

Poststack migration translates $\psi(x, z=0, t)$, the recorded measurements, into $\psi(x, z, t=0)$, the measurements which would have been recorded at time zero if recording planes had been distributed within the earth rather than only at its surface. Different migration methods extrapolate the wavefield to depth by implementing different numerical solutions to equation (12). In this thesis, I am primarily concerned with migrations which can be classified as either phase shift implementations or finite difference implementations. In the next section, I will briefly describe both implementations, and I will discuss some of the advantages and disadvantages associated with each.

Some knowledge of the Fourier transform (Bracewell, 1976) is necessary for discussing phase shift methods, and it will also simplify the discussion of finite difference implementations. The frequency representation of a series f(t) is given by its Fourier transform as

$$F(\omega) = \int_{-\infty}^{\infty} dt\ e^{-i\omega t}\ f(t) \quad . \tag{13}$$

Given $F(\omega)$, it is possible to find f(t) by the inverse Fourier transform:

$$f(t) = \frac{1}{2\pi} \int_{-\infty}^{\infty} d\omega\ e^{i\omega t}\ F(\omega) \quad . \tag{14}$$

Phase Shift and Finite Difference Migration Implementations

The dispersion relation can be derived by substituting the plane wave $\psi\ (x, z, t) = e^{(-i\omega t + ik_x x + ik_z z)}$ into equation (12) (Claerbout, 1985). After cancelling common terms, the result is

$$k_z^2 + k_x^2 - \frac{4\,\omega^2}{v^2} = 0 \quad . \tag{15}$$

The plane wave specified by (15) has a temporal frequency of ω and spatial frequencies of k_x and k_z. The spatial frequencies are usually referred to as the

horizontal and vertical wavenumbers. Solving (15) for k_z yields a square root which may be chosen either positive or negative; the two solutions describe upgoing and downgoing waves, respectively. In a stacked seismic section, it is usually assumed that only upgoing reflections are present; this assumption is applied by choosing the positive square root as the dispersion relation:

$$k_z = \sqrt{\frac{4\ \omega^2}{v^2} - k_x^2} \quad . \tag{16}$$

The spectral representation of the wavefield, denoted by $\tilde{\Psi} = \tilde{\Psi}\ (k_x, z, \omega)$, can be constructed by performing Fourier transformations of $\psi\ (x, z, t)$ over the coordinate variables x and t. If (16) is inverse Fourier transformed over k_z and then multiplied by $\tilde{\Psi}\ (k_x, z, \omega)$, the resulting equation is

$$\frac{\partial}{\partial z}\ \tilde{\Psi} = i \sqrt{\frac{4\ \omega^2}{v^2} - k_x^2}\ \tilde{\Psi} \quad . \tag{17}$$

Equation (17) is a homogeneous first order differential equation. Both phase shift and finite difference poststack migrations can be derived from it. Before discussing finite difference implementations, I will show the derivation of recursive phase shift migration as described by Gazdag (1978). I am beginning with this method because other phase shift implementations can easily be described by using recursive phase shift as a foundation.

Phase shift migration operates in the spectral domain by implementing the analytical solution to equation (17). It is a fundamental advantage of phase shift migration that it is possible to implement the exact solution to (17) in the spectral domain. However, it is a fundamental disadvantage of phase shift migration that it is necessary to assume that the velocity function, v, varies with depth only. Because the solution is formulated with no reference to lateral spatial coordinates, a laterally invariant velocity function must be substituted into (17) (i.e., $v = \bar{v}(z)$). Usually $\bar{v}(z)$ is chosen as some horizontal average of an interpreted laterally varying velocity function. Under this restriction, the solution to (17) is given by

$$\tilde{\Psi}(k_x, z, \omega) = A\, e^{i z \sqrt{4\omega^2 / \bar{v}^2(z) - k_x^2}} . \tag{18}$$

A solution for the coefficient A can be found by reformulating (18) as a recursive problem. After rewriting (18) twice, once with $z = z_n$ and once with $z = z_{n+1}$, the two expressions are combined to obtain the recursive solution

$$\tilde{\Psi}'(k_x, z_{n+1}, \omega) = \tilde{\Psi}(k_x, z_n, \omega) \cdot e^{i z_{n+1} \sqrt{4\omega^2 / \bar{v}^2(z_{n+1}) - k_x^2} - i z_n \sqrt{4\omega^2 / \bar{v}^2(z_n) - k_x^2}} . \tag{19}$$

By stipulating that the interval from z_n to z_{n+1} is small enough to approximate $\bar{v}(z_n)$ by $\bar{v}(z_{n+1})$, (19) becomes

$$\tilde{\Psi}'(k_x, z_{n+1}, \omega) = \tilde{\Psi}(k_x, z_n, \omega)\, e^{i (z_{n+1} - z_n) \sqrt{4\,\omega^2 / \bar{v}^2(z_{n+1}) - k_x^2}} \quad . \qquad (20)$$

I am denoting the downward continued wavefield with a prime symbol to indicate that a laterally invariant velocity function was used in the calculation.

Equation (20) defines recursive phase shift migration. The operation is initialized at $z_n = 0$, the horizontal level at which the data was collected. Solving (20) for some non-zero value of z_{n+1} effectively moves all coincident source and receiver positions down to that level. After inverse transform of $\tilde{\Psi}'(k_x, z_{n+1}, \omega)$ to $\psi(x, z_{n+1}, t)$, the image of the energy sources, or reflectors, at (x, z_{n+1}) is given by $\psi(x, z_{n+1}, t=0)$. (In practice, only the part of the wavefield corresponding to time zero has to be inverse transformed to extract the image at z_{n+1}. This means that a single sum over all frequencies is all that is required.) To image the subsurface at the next depth step, this process is repeated using the wavefield at z_{n+1} to extrapolate the wavefield at z_{n+2}.

I used the split-step Fourier migration (Stoffa et al., 1990) to produce the majority of the migrated sections in this thesis. This algorithm is similar to the phase shift migration described above. The two migrations differ in that the split-step migration is able to accommodate lateral velocity variations. In split-step, each depth interval is migrated in two steps. First, a global phase shift, as described by (20), is implemented using a constant reference velocity. This is followed by an inverse Fourier transformation of $\tilde{\Psi}'(k_x, z_{n+1}, \omega)$ to $\Psi'(x, z_{n+1}, \omega)$. Local adjustments can then be applied to the phase shift migration using the difference between the local velocity and the reference velocity; that is:

$$\Psi (x, z_{n+1}, \omega) = \Psi' (x, z_{n+1}, \omega)\ e^{\,i (z_{n+1} - z_n) \frac{2\omega}{v - \bar{v}(z_{n+1})}} . \qquad (21)$$

After the migrated image at z_{n+1} is extracted, $\Psi (x, z_{n+1}, \omega)$ is forward transformed to $\tilde{\Psi} (k_x, z_{n+1}, \omega)$ so that the data can be migrated to the next depth level. In split step Fourier migration, equation (20) provides a global phase shift operator that acts to collapse diffractions using the reference velocity $\bar{v}(z_n)$. Equation (21) can be considered as the thin lens correction which properly positions the data in depth (Claerbout, 1976).

The Costa Rica data presented here which were not migrated by the split step method were migrated by one of a variety of finite difference algorithms. Migrations based on finite difference approximations to equation (17) were first introduced by Claerbout (1970). The majority of migration algorithms in use today are finite difference implementations, but the implementations are usually more sophisticated than Claerbout's original algorithm. In equations (22) and (23), I will present finite difference migration in terms of the 45° approximation.

If the dispersion relation given by equation (17) was reformulated in the horizontal space domain, the diffraction operator in the corresponding migration could utilize a laterally varying velocity model. However, inverse Fourier transform of (17) over k_x creates a differential operator under the square root; the square root of a differential operator does not have a numerical representation. In finite difference implementations, the square root in (17) is approximated by a series expansion before inverse Fourier transformation. This is the primary shortfall of all finite

difference migration implementations. These methods all use an approximation to (17) rather than the actual dispersion equation.

If the Muir square root expansion (Claerbout, 1985) is used to generate the series expansion of (17), and the series is truncated after the second term, the result is the so-called 45° migration equation:

$$\frac{\partial}{\partial z}\tilde{\Psi} = i\left[\frac{2\omega}{v} - \frac{k_x^2}{\frac{4\omega}{v} - \frac{v k_x^2}{4\omega}}\right]\tilde{\Psi} \quad . \tag{22}$$

Equation (22) can be inverse Fourier transformed over k_x, so that the migration problem can be formulated in the space domain. However, to allow a tractable solution, the differential equation must now be replaced by two separate differential equations. Applying this assumption of separability, known as splitting (Hatton et al., 1981), produces a diffraction equation, given by

$$\left[\frac{4\omega}{v} + \frac{v}{4\omega}\frac{\partial^2}{\partial x^2}\right]\frac{\partial}{\partial z}\Psi = i\frac{\partial^2}{\partial x^2}\Psi \quad , \tag{23a}$$

and a thin lens equation, given by

$$\frac{\partial}{\partial z}\Psi = i\frac{2\omega}{v}\Psi \quad . \tag{23b}$$

The diffraction equation can be solved by finite difference methods in either the space-frequency domain or, after inverse transformation of (23a) over ω, in the space-time domain. Interestingly, the analytical solution of the thin lens equation produces an operator almost identical to the thin lens operator in the split-step migration. One of the advantages of constructing finite difference depth migration algorithms in the space-frequency domain is that the thin lens correction can be applied exactly in that domain, instead of by a finite difference approximation.

It is worth noting that the thin lens operator is the same no matter which truncation of the Muir square root expansion is used. This indicates that the error in truncating the series expansion is absorbed by the diffraction term in the resulting differential equation. The dilemma presented by finite difference migration, then, is that although the diffraction operator utilizes a laterally varying velocity function, it does not necessarily correctly collapse the diffractions that would be generated by that function.

Both split step and finite difference 3-D depth migrations of the Costa Rica data were performed using the identical velocity model. Figures 28 (split step) and 29 (finite difference) are the middle dip sections taken from each migrated data volume. The vertical axis of the displays have been converted to two-way travel-time by linear interpolation of the depth migrated output using the input velocity model. Based on comparisons of the results, two qualitative observations may be made. First, despite the use of an approximation of the velocity model in its diffraction operator, the split step migration did a better job in removing diffraction tails from the data than did the finite difference migration. Second, the migrated split step results contained a higher level of noise than the results of using the finite difference

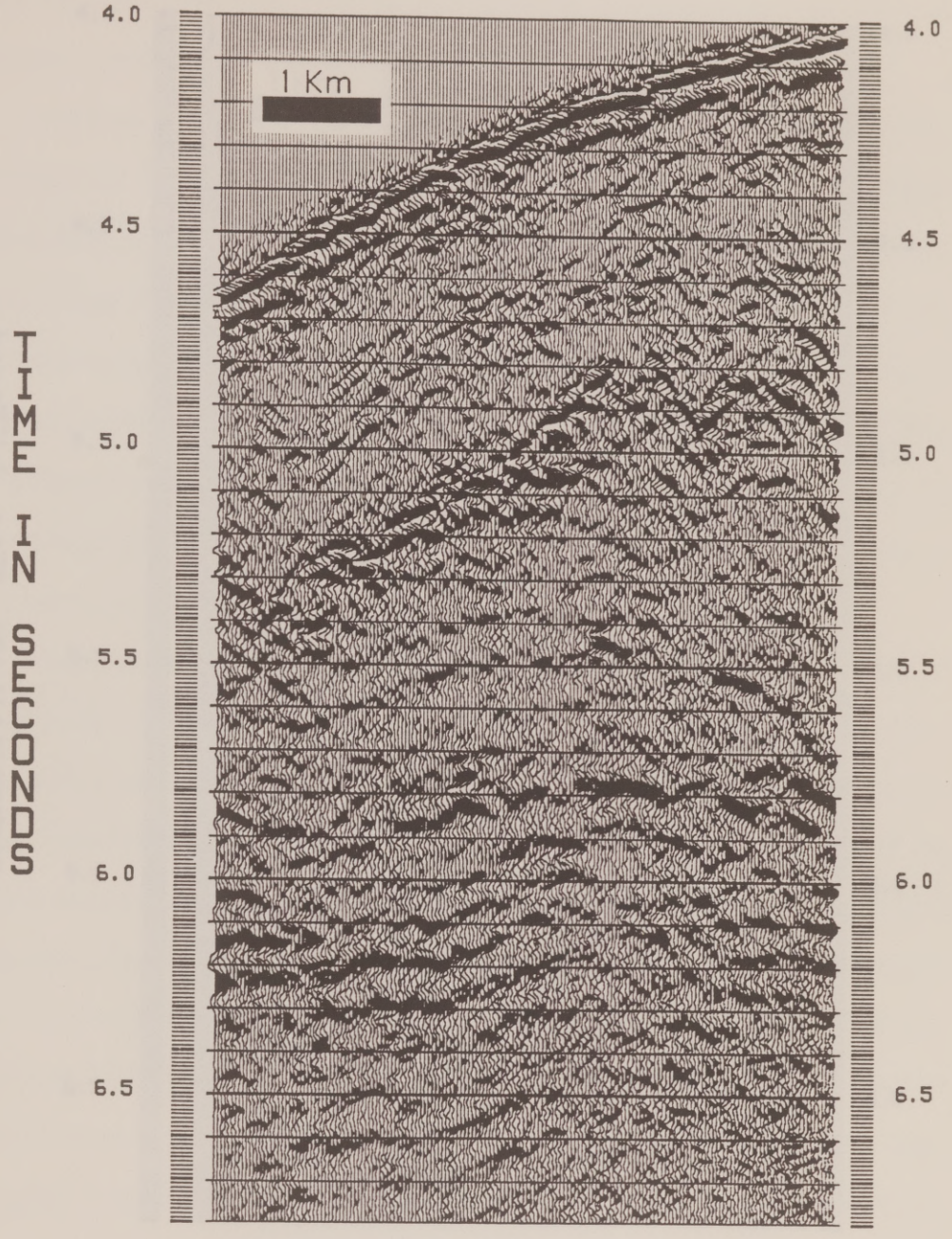

Figure 28. Costa Rica seismic data after 3-D split-step Fourier depth migration. Frequencies from 8-48 Hz were migrated using 80 meter migration intervals and 8 meter sampling intervals. The data were subsequently converted to two-way travel-time.

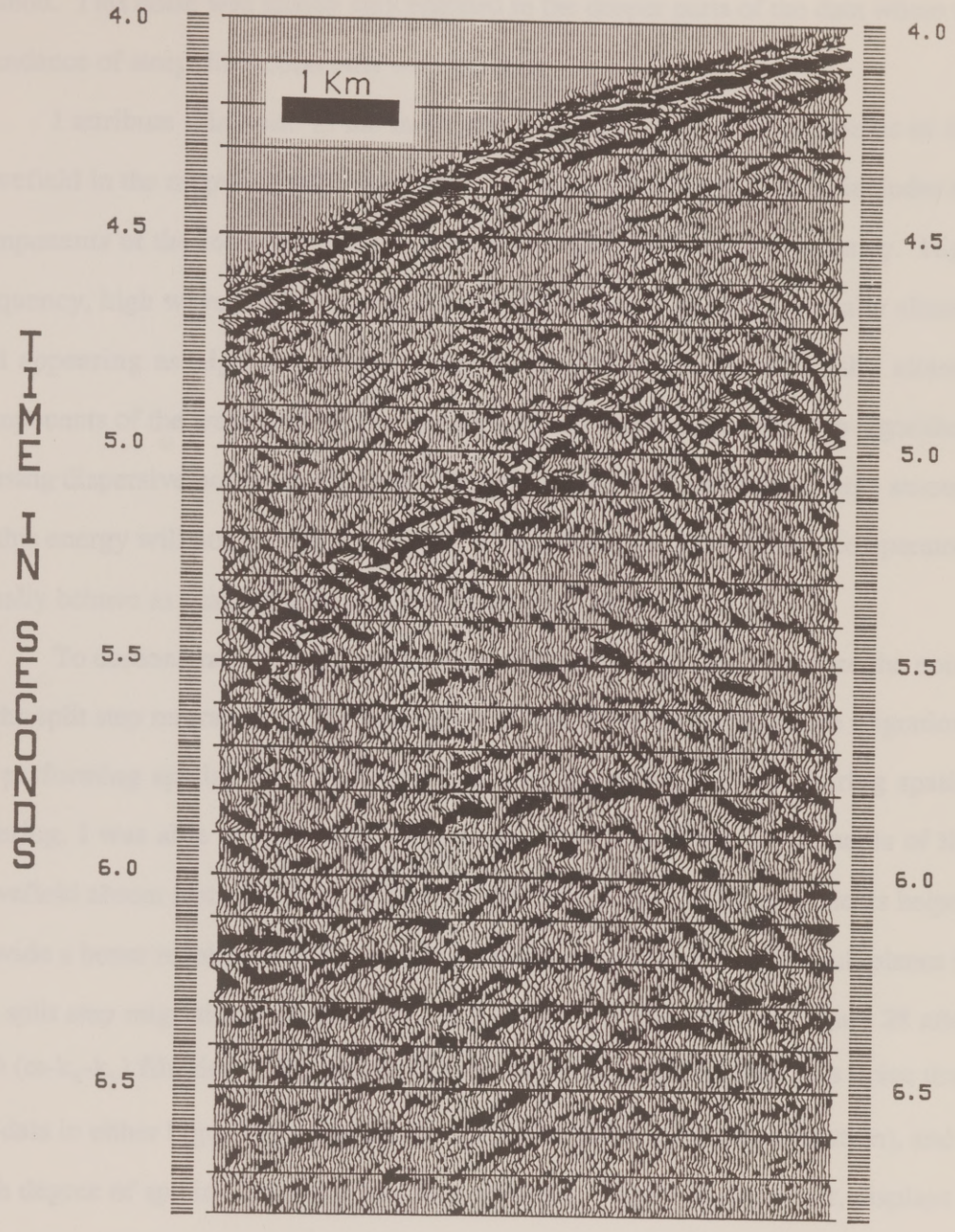

Figure 29. Seismic data from the same area as in Fig. 28, after 3-D finite difference depth migration. Frequencies from 8-48 Hz were migrated using 80 meter migration intervals and 8 meter sampling intervals. The data were subsequently converted to two-way travel-time.

method. This noise was mostly concentrated in the deeper parts of the data where an abundance of steep diffraction tails were present.

I attribute this noise to the inclusion of spatially aliased components of the wavefield in the migrated split step results. Split step Fourier migration includes all components of the recorded wavefield up to the specified cut-off frequency. High frequency, high wavenumber events are always in danger of being spatially aliased and appearing as high frequency, lower wavenumber events. Spatially aliased components of the wavefield will be improperly migrated by the split step algorithm, causing dispersive noise. In the case of finite difference algorithms, a large amount of this energy will not be migrated at all. This is because finite difference operators usually behave as spatial high-cut filters (Berkhout, 1981).

To demonstrate proof of the above conjecture, I was able to reduce the noise in the split step migrations to the same level as that in the finite difference migrations by performing spatial filtering of the split step migration results. During spatial filtering, I was able to save high wavenumber, low frequency components of the wavefield absent from the finite difference data; these wavefield components helped provide a better resolution of sharply discontinuous structures such as fault planes in the split step migrations. Figures 30 and 31 show the same data as Figure 28 after 3-D (ω-k_x-k_y) filtering. The data in Figure 30 include significantly less noise than the data in either Figure 28 or Figure 29 (the finite difference depth migration), and a high degree of spatial resolution has been retained. Figure 31, however, displays a greatly reduced spatial resolution because of the use of a more severe frequency-wavenumber filter. In Appendix 2, I more thoroughly discuss spatial aliasing, and I

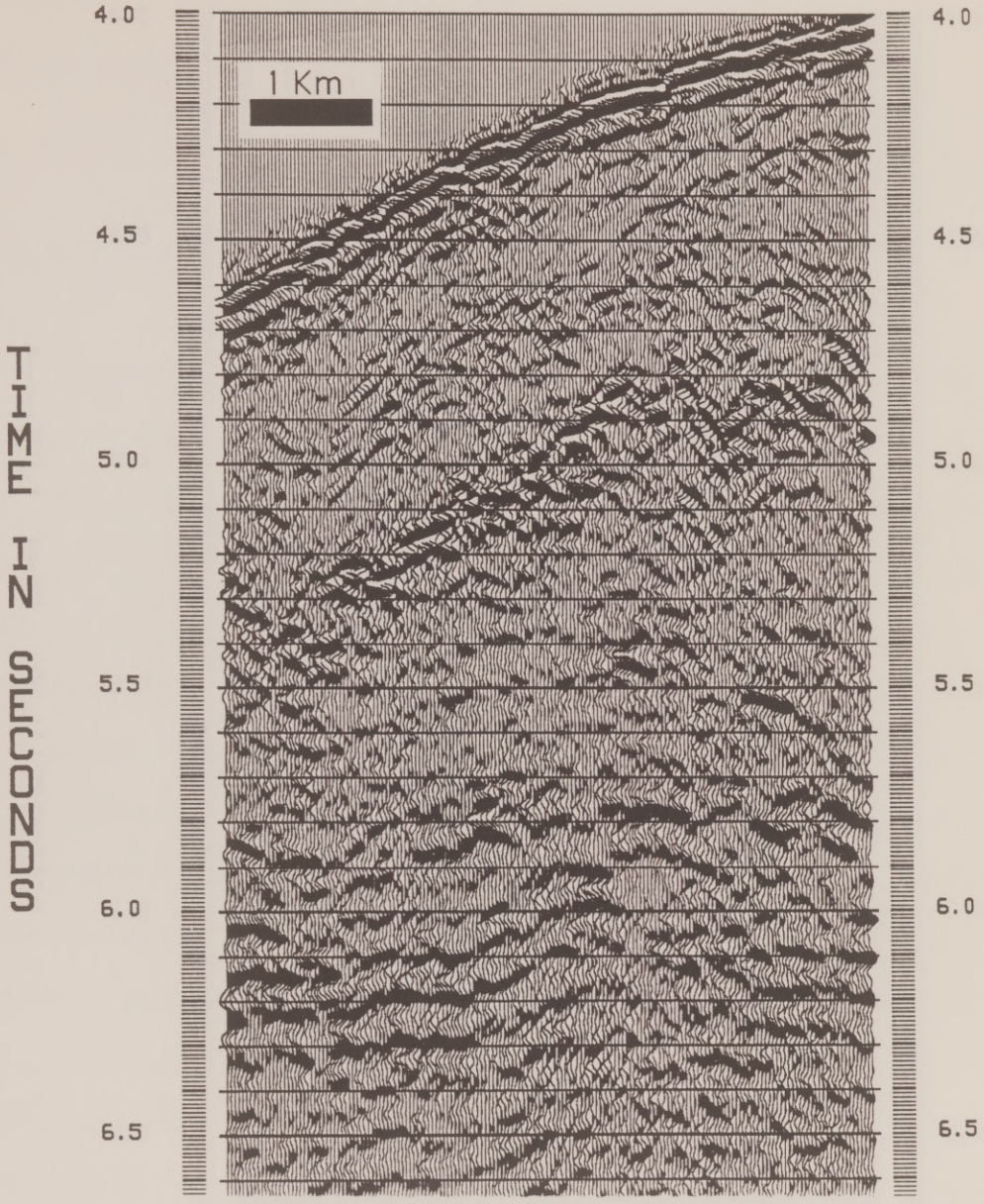

Figure 30. The same data as in Fig. 28, after 3-D spatial filtering in the ω-k_x-k_y domain.

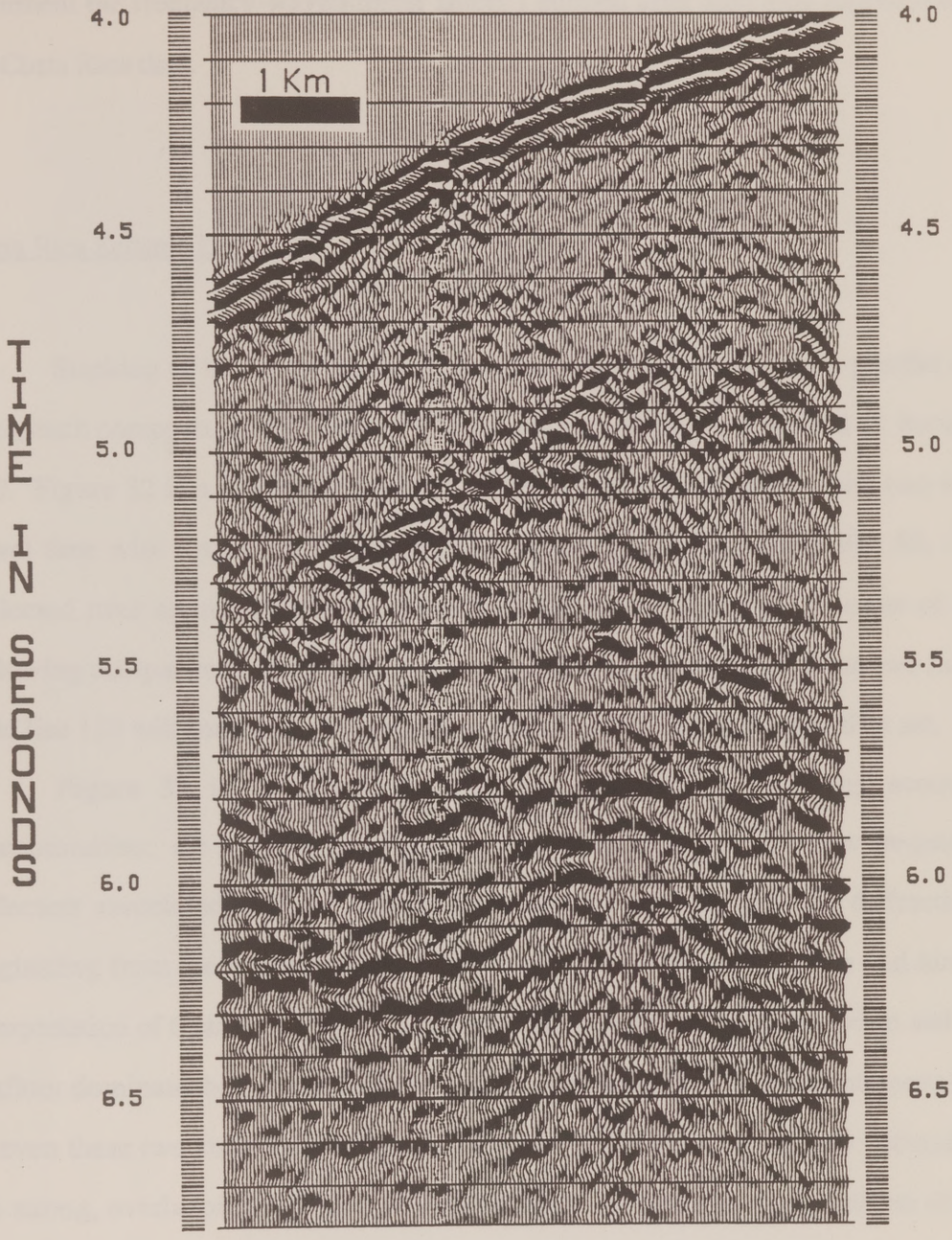

Figure 31. The same data as in Fig. 28, after 3-D spatial filtering in the ω-k_x-k_y domain. The spatial resolution is poorer than in Fig. 30 because the spatial and temporal bandwidths were more severely limited.

document the frequency-wavenumber filters I applied after split step migrations of the Costa Rica data.

Costa Rica Seismic Data

Stacking of the Costa Rica grid data reduced the data set to 170 parallel dip lines, each composed of 650 traces. The lines were arbitrarily numbered 41 through 210. Figure 32 is a display of line 122. The vertical axis represents the two-way travel time with respect to sea level. The middle swath line, swath line 50, was collected over approximately the same location as grid line 122, so most of the following comparisons of the grid and swath data sets will focus on these two lines. Grid line 122 will sometimes be referred to as the middle line of the grid data set.

Figure 32 is dominated by two surfaces exhibiting strong acoustic discontinuities: the seafloor and the top of the accretionary prism. Low frequency reflectors associated with the base of the prism are also present, but diffractions originating from the upper surface of the prism obscure these reflectors and hinder interpretation of their structure. In fact, diffractions from the top of the prism and the seafloor dominate the stacked section to such a degree that a structural interpretation of even these two surfaces is difficult; their rough surfaces are actually defined by the strong, overlapping diffractions they produce. As a result, the definition of the accretionary prism surface can only feebly surpass the observation that it is very rough. This surface appears to have a primary periodicity of about 6.5 km, but this

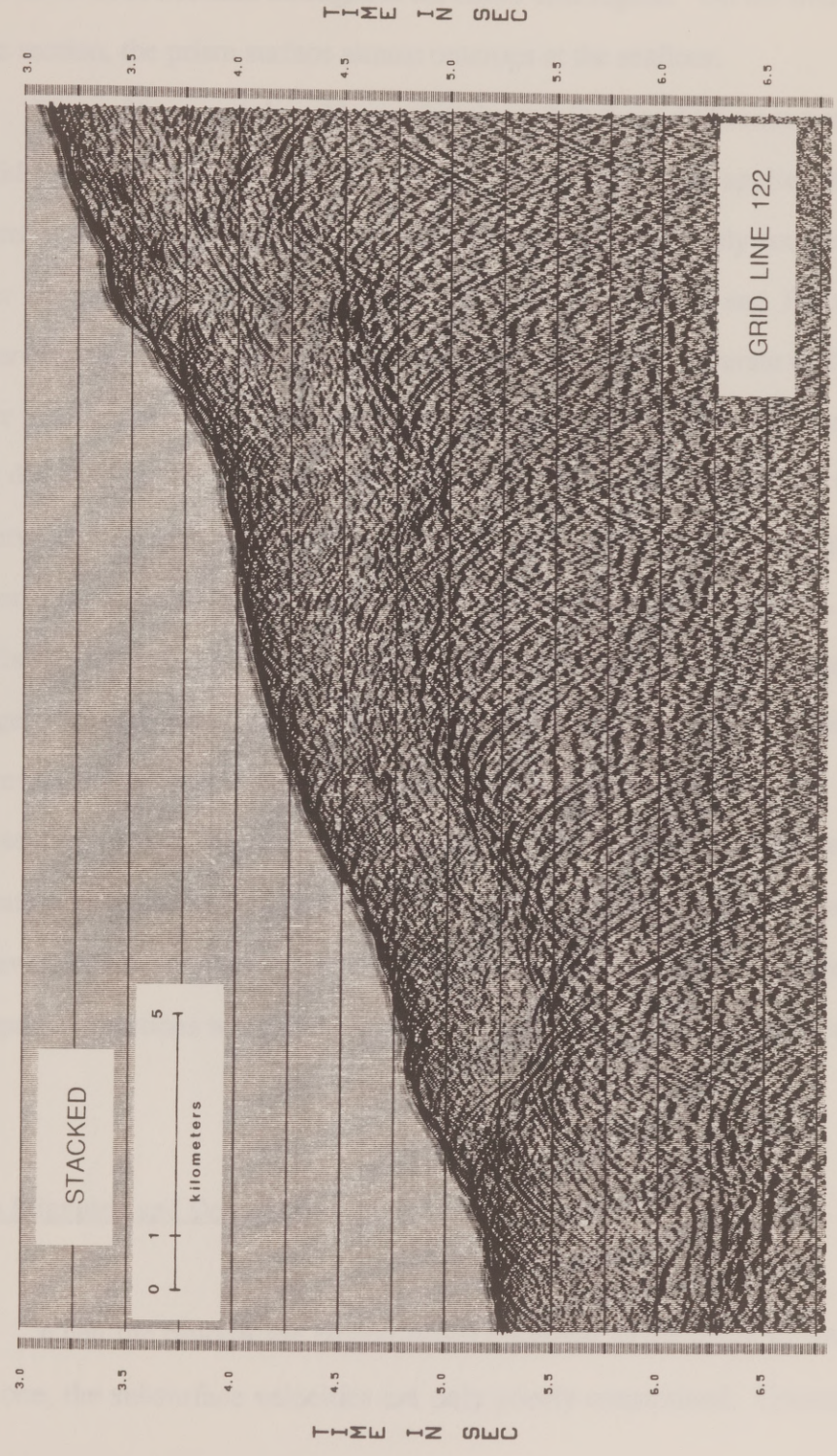

Figure 32. Stacked data from the middle bin line of the 3-D grid.

observation does not hold throughout the entire data region. On the trenchward side of the section, the prism surface almost outcrops at the seafloor.

Figure 33 was produced by performing a 2-D finite difference time migration of grid line 122. The time migration which produced Fig. 33 applies the 15° finite difference algorithm in two cascaded stages to achieve a relatively accurate result at a lower computational price than a 45° algorithm. Larner and Beasley (1987) conservatively estimate that two-stage cascaded migration is accurate to 27°, although better results are possible. Comparison of Figure 33 to Figure 32 shows that the most dramatic improvement in the image is due to the contraction of the diffractions. Observations of structures within the slope cover and the accretionary prism are no longer obstructed by the diffraction tails which cut through the data. Structural details of the seafloor are also clearly visible. At the surface of the accretionary wedge, the diffracted energy has been constricted to a more limited region. However, the surface is not properly focused and appears disordered. In the next two sections I will discuss the advantages of depth migration compared to time migration and 3-D imaging will be contrasted to 2-D imaging. It is worth noting, however, that in accretionary wedge environments, any migration procedure which collapses diffractions will significantly increase the interpretability of the data.

Time Migration and Depth Migration

When the ratio of the largest offset collected to the depth of interest is less than one, the subsurface velocities are only poorly constrained. Consequently, the

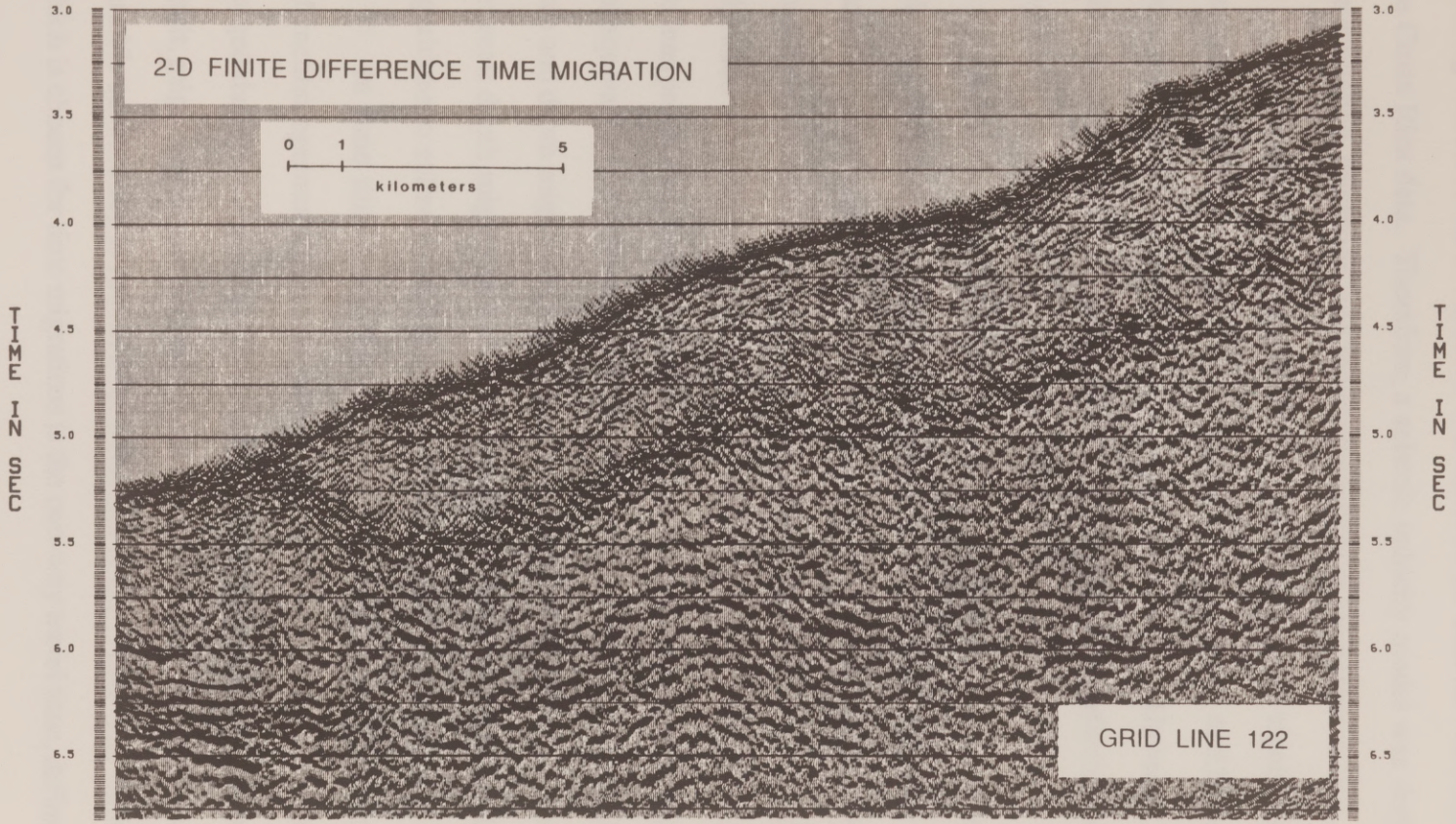

Figure 33. 2-D finite difference time migration of grid line 122. The velocity model used was produced by conserving the vertical time-depth relation implied by the interval velocity model that was used for all depth migrations in this thesis.

stacking velocities are not accurate indicators of the interval velocities in the region of the Costa Rica data. Therefore, a seismic velocity model was derived by iterative interpretation, migration, and focusing analysis of the poststack data.

Even with erroneous velocities, time migration can significantly improve the interpretability of the data. Velocities in error by as much as ±15 percent will often focus the data reasonably well (Parks and Hatton, 1987). However, uncertainties of this magnitude make a considerable difference in where reflectors are positioned in depth.

Because of the uncertainties inherent in developing interval velocity models, seismic interpreters frequently prefer to study migrated time sections instead of depth sections in the early stages of interpretation (Stolt and Benson, 1986). Once they derive a reasonably accurate velocity model, they can use it to perform a depth migration or to stretch a time migrated section to depth. In applying this philosophy, the interpreter must bear in mind that a migrated time section after depth conversion is not equivalent to a migrated depth section. There are fundamental differences in how time and depth migrations implement wave propagation theory. The main difference between depth migration and time migration algorithms is the ability of the depth algorithms to utilize the details of the velocity field during migration.

In time migration, the migration is carried out by the application of the diffraction operator discussed earlier. Because the thin lens term is neglected, the imaged data are not necessarily properly redatumed at each migration interval. As a result, migration across constant depth layers is no longer a natural operation, and a variable substitution is required for z (Hatton et al., 1986). The "natural coordinate" which is chosen for time migrations is the two-way travel time, defined by

$$\tau_n = \int_0^{z_n} dz \, \frac{2}{v} \quad . \tag{24}$$

Hubral (1977) introduced the concept of the "image ray", which defines the minimum-time travel path for the apex of a diffraction. He demonstrated that integral migration methods such as Kirchhoff migration always collapsed a diffraction to the image ray passing through the diffraction's apex; therefore the image of a diffractor will appear directly under the horizontal coordinate at which its image ray meets the surface. This is a serious deficiency, because for a velocity structure with lateral variation, the actual horizontal coordinate of the diffractor is not the same as the location where its image ray surfaces. Integral migration implementations are not covered here, but Larner et al. (1981) demonstrated that all time migration implementations share this failure because they are "founded on the assumption that, locally, the medium is horizontally layered (p. 738)." This assumption follows from neglecting the thin lens term. Without the thin lens term, the diffraction time surface for each image point is treated as a hyperboloid across each migration step. Diffractions are hyperbolic only if the velocity structure above the reflector is constant (Hubral and Krey, 1980). In a medium with lateral velocity variations, the shape of diffractions can deviate significantly from any idealized geometry.

In depth migration, imaging and positioning of reflectors are done concurrently so that the migration can realistically account for wavepath distortions through the overlying structure. Use of a depth migration algorithm is essential for

proper imaging of areas with severe lateral velocity variations, such as those that exist in accretionary wedge environments.

Figure 34 is a 2-D split step depth migration of the middle line of the grid, displayed after time conversion. The velocity model used in the migration was a laterally varying grid of interval velocities as a function of depth. The velocity model used in the 2-D time migration of Figure 33 was produced by conserving the vertical time-depth relation implied by interval velocity model. Identical filters were applied to both sections after migration.

Comparing the 2-D time and depth migrations, we observe that the reflectors are more sharply focused by the depth migration within the accretionary wedge. Overall, however, these reflectors are positioned similarly, and exhibit only minor differences. The most significant discrepancies between the two migrations occur where sharp velocity discontinuities have been interpreted, particularly at the upper accretionary prism surface. Figures 35a and 35b display blow-ups of this surface for each of the 2-D migrations. Improperly collapsed diffractions distort the character of the time migrated section (Fig. 35a) and give the surface an overmigrated appearance. Although these reflectors interfere with and cross each other on the 2-D depth migrated section (Fig. 35b), they do not exhibit the focusing problems of the time migrated result. In the slope cover, the continuity of the dipping reflector in the upper left part of the section is greatly improved in the depth migration.

Figure 36 is a coarse representation (in two-way time) of the interval velocity model we used to migrate the data. A linear vertical velocity gradient was applied inside the accretionary wedge. The velocity discontinuity at the surface of the accretionary wedge is consistent with both the reflectivity of the data and the inferred

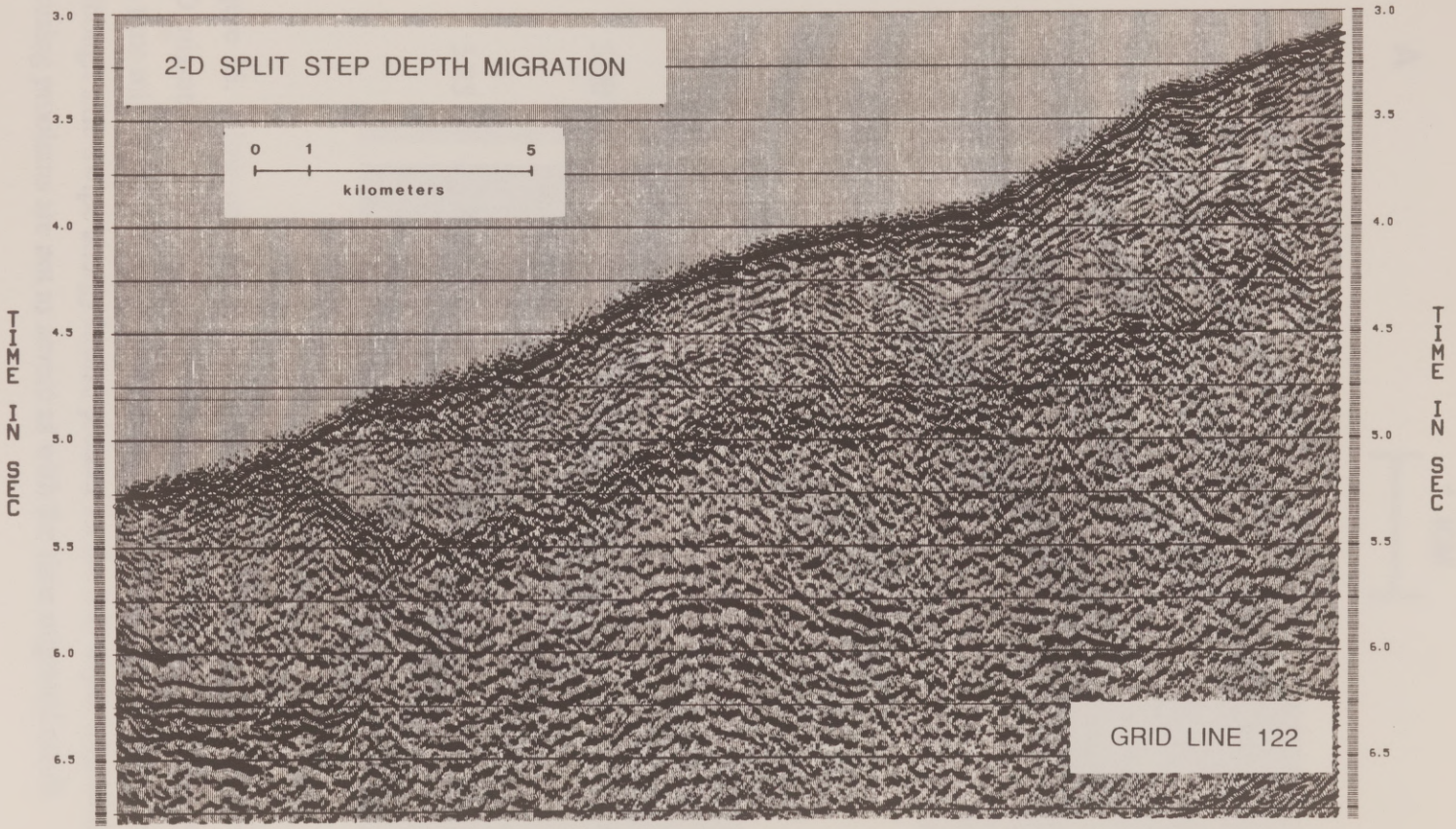

Figure 34. 2-D split step depth migration of grid line 122, displayed after time conversion. Filters applied to this section after migration were identical to those applied to the data in Fig. 33.

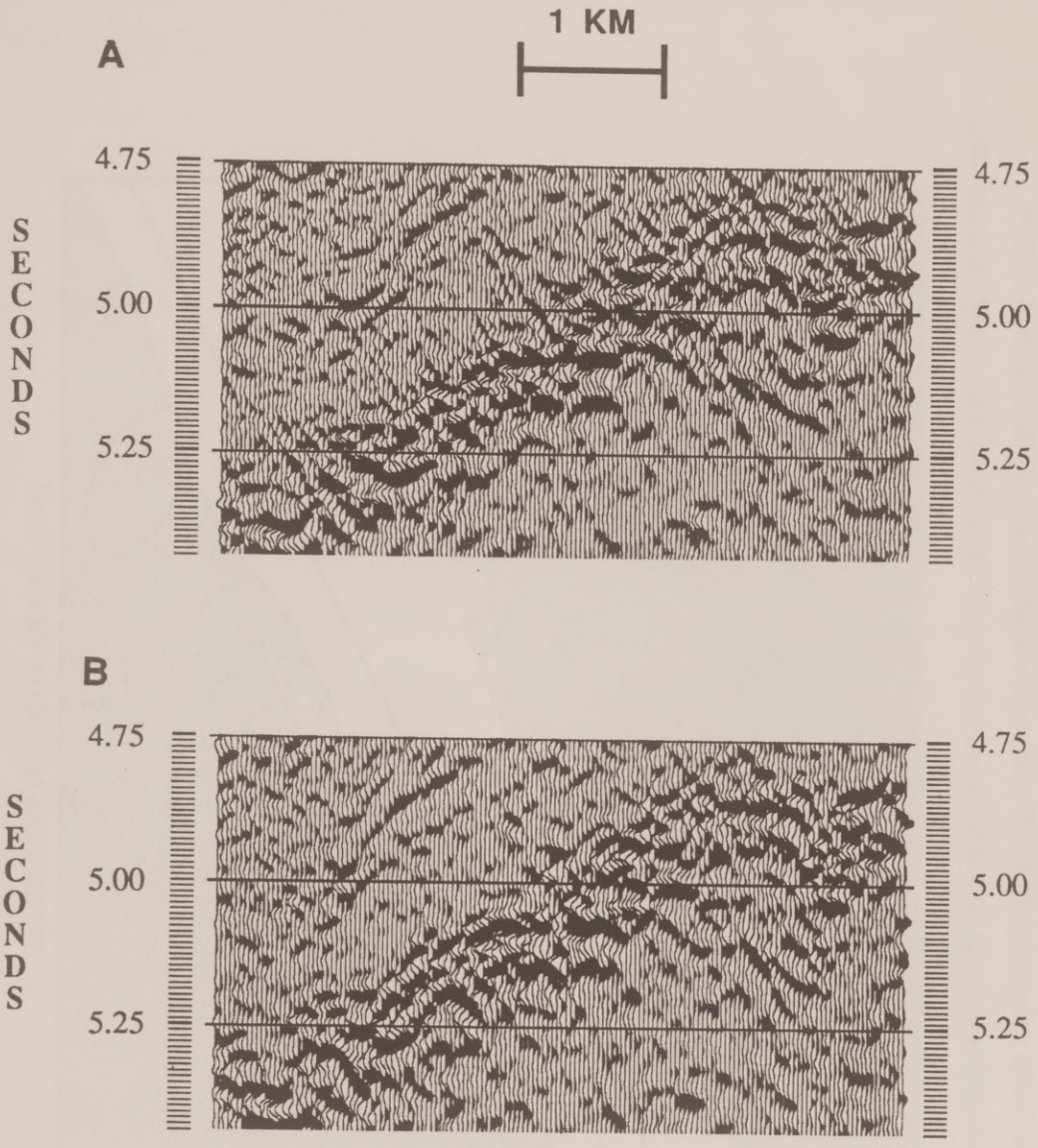

Figure 35. Blow-ups of the upper accretionary prism surface for each of the 2-D migrations. (A) Improperly collapsed diffractions distort the character of the time migrated section and give the surface an overmigrated appearance. (B) Although side-swipe energy is also present on the 2-D depth migrated section, focusing problems are not as severe as with the time migrated result.

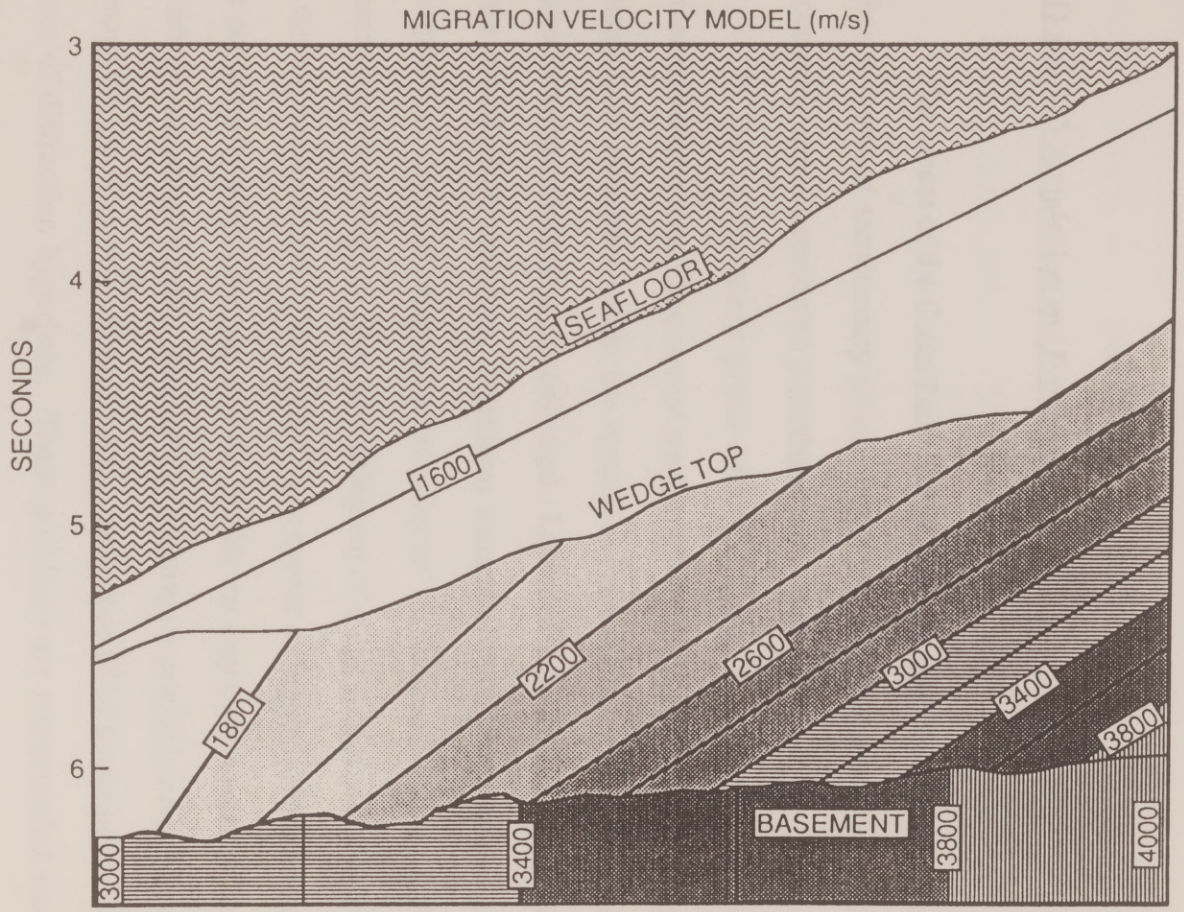

Figure 36. A coarse representation (in two-way travel-time) of the interval velocity model used to migrate the Costa Rica data. A linear vertical velocity gradient was applied inside the accretionary wedge.

geological structure. As the above example demonstrates, it is the presence of this rapid velocity gradient which made it absolutely necessary to utilize depth migration in imaging the Costa Rica data.

2-D and 3-D Acquisition and Processing

The aspect of the Costa Rica seismic survey which distinguishes it most from other surveys of accretionary prisms is the use of three dimensional acquisition, processing, and interpretation procedures.

In the accretionary prism offshore Costa Rica, the earth has a three dimensional structure. Because of structural variations in the strike direction, some energy from reflectors within the vertical collection plane is transmitted to out-of-plane locations where it is not collected. Likewise, "sideswipe" energy is collected from out-of-plane locations. Problems associated with sideswipe energy can be compounded by 2-D migration techniques (Stolt and Benson, 1986). Two dimensional migrations of lines containing out-of-plane energy will leave this energy in the migrated section. This "noise" may appear as interpretable structures which are not actually within the plane of the profile, or may even appear to be structures which do not actually exist. Attempts to construct a proper interval velocity model through the use of iterative migrations may be hampered by the inclusion of non-axial slices of diffraction hyperbola. These problems are compounded the more the subsurface in an area deviates from a two dimensional structure in the cross-line direction.

The mispositioning of reflectors by 2-D migration can also be subtle. Although 2-D migration of dip lines will result in a properly imaged section for two dimensional structures, the same is not true of strike lines collected across two dimensional structures. The inherent assumption of 2-D migration is that all structural variation occurs along the data section; that is, every 2-D line is assumed to be a dip line. The following example from Dobrin and Savit (1988) illustrates the problem inherent in performing 2-D migrations of data not oriented parallel to dip. A strike line collected over a planer dipping layer will record a horizontal reflector, as demonstrated in Figure 37a. Because no dip information is recorded for this reflector, its position after migration will be the same as before migration. However, the reflection was actually generated out of the plane of the section, and so the reflector has been migrated (or not migrated) to the incorrect depth. This is demonstrated in Figure 37b using comparisons of the reflector position after 2-D migrations of both strike and dip lines. As can be seen, the reflector underneath the position marked "X" has been correctly migrated up-dip to where it should belong on the dip line. (This demonstrates that lines from 2-D surveys should be tied at crossings before 2-D migration, as mis-ties will result after 2-D migration.)

With three dimensional coverage, no assumptions about the geometry of the reflectors are required. A true 3-D depth migration algorithm can position the reflectors collected within the grid to their correct spatial locations as determined by the velocity function. Diffraction surfaces are properly collapsed, improving the data quality and making a better structural interpretation possible. The availability of a 3-D data set, then, presents a clear superiority over 2-D coverage in terms of imaging

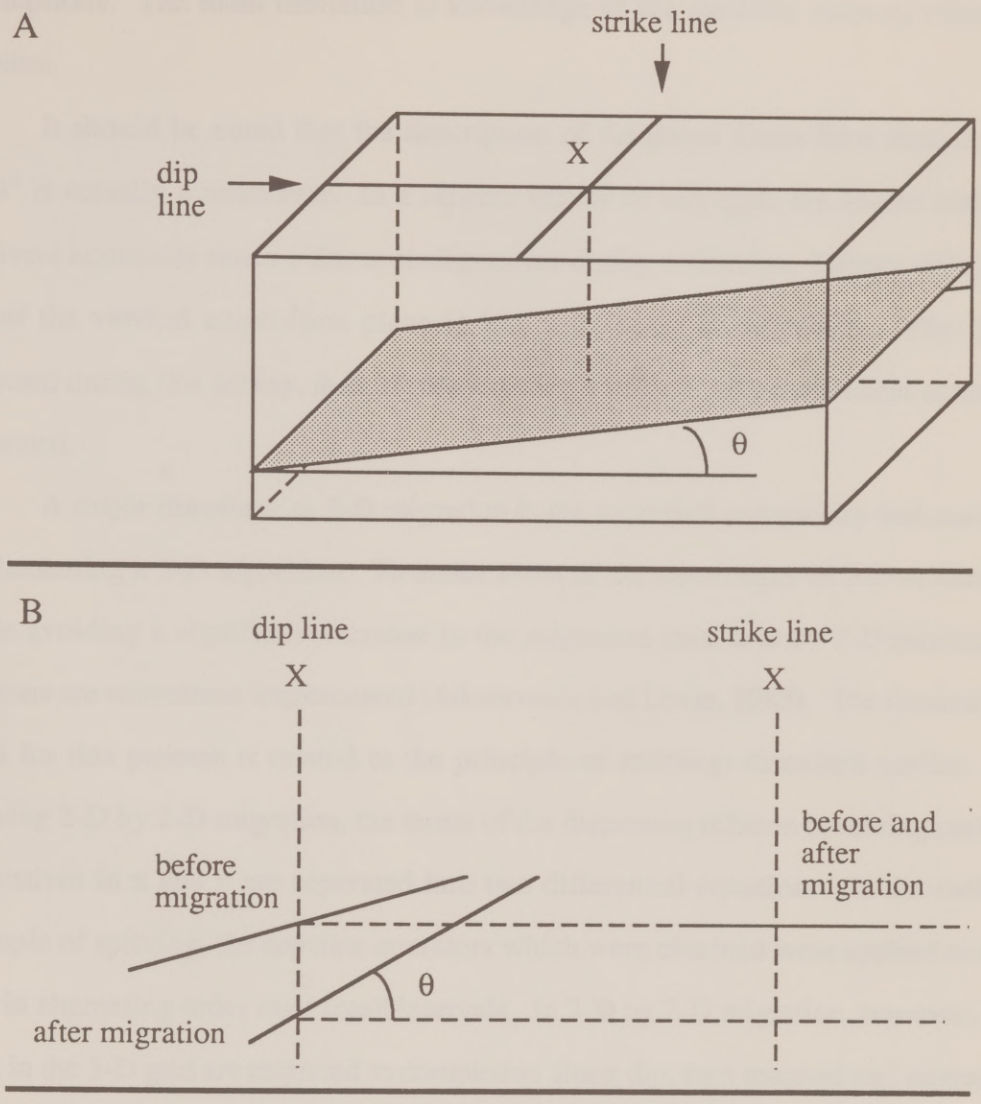

Figure 37. Example illustrating the problem with performing 2-D migrations of data not oriented parallel to dip. (A) A strike line collected over a planer dipping layer will record a horizontal reflector. (B) Comparison of the reflector position after 2-D migration of both strike and dip lines. On the dip line, the reflector underneath the position marked "X" has been correctly migrated up-dip to where it belongs. Because no dip information was recorded for the strike line, the reflector position after migration is the same as before migration. After Dobrin and Savit (1988).

assumptions. The main limitation is knowledge of the spatially varying velocity function.

It should be noted that the description of the dense Costa Rica data set as "3-D" is actually a misnomer. In a seismic survey of this type, the source and all receivers nominally retain a linear configuration during collection. Energy reflected out of the vertical acquisition plane is lost and cannot be recovered. The data collected during this survey, then, represents only a fraction of the wavefield actually generated.

A major drawback to 3-D migration is the increased complexity and cost of implementing a 3-D algorithm. To attain some of the advantages of 3-D coverage while avoiding a significant increase in the migration cost, 2-D by 2-D migration schemes are sometimes implemented (Jakubowicz and Levin, 1983). The theoretical basis for this process is related to the principle of splitting, discussed earlier. In deriving 2-D by 2-D migration, the terms of the dispersion relation involving partial derivatives in x and y are separated into two differential equations. In the earlier example of splitting, the separate operators which were obtained were applied to the data in alternating order over small intervals. In 2-D by 2-D migration, however, all lines in the 3-D grid are migrated to completion along dip, then resorted and migrated along strike. The full separation approximation is exact in the case of a constant velocity function, so in justifying its validity for a data set, the smoothness of the velocity model must be considered.

Figure 38 presents examples of various finite difference migrations in the vicinity of a mud volcano in the grid area. For reference, the upper left section is the stacked data in the region. The data in the upper right has been 2-D migrated.

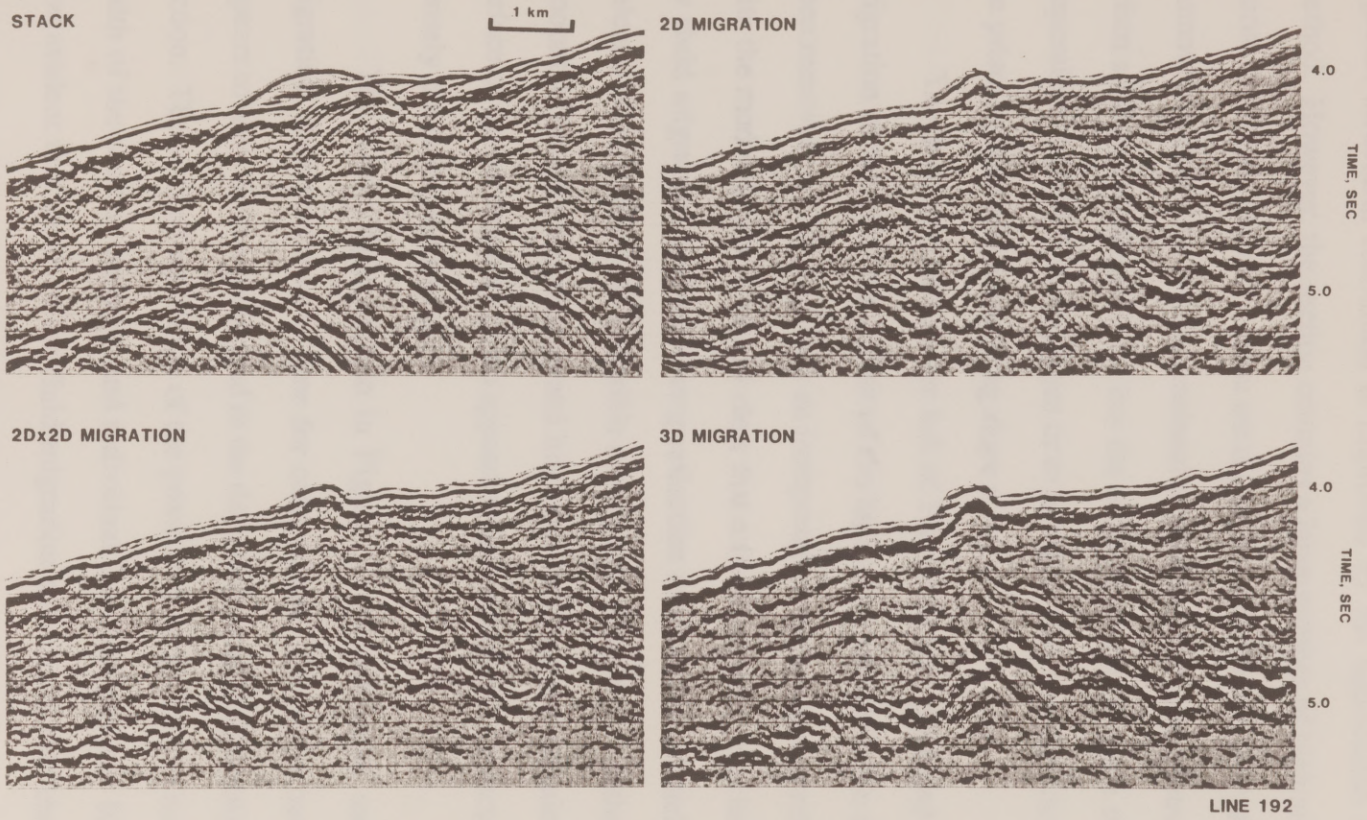

Figure 38. Examples of various finite difference migrations in the vicinity of a mud volcano in the grid area. (Upper left) Stacked data. (Upper right) 2-D time migrated data. (Lower left) 2-D by 2-D time migration of the grid data. (Lower right) Data migrated using a 3-D depth migration, then stretched to time for comparison.

Comparison of the two upper figures demonstrates once again that in complex data regions, structural resolution is improved by the application of *any* migration method. However, the section contains a large number of high angle events cutting across the slope sediments; these are diffraction tails from out of plane sources which cannot be removed by two dimensional migration. The general structural trend of the prism surface can be inferred, but the mixture of out-of-plane reflectors makes it impossible to identify fault planes or to interpret with any confidence the relation of the prism surface to the overlying slope cover.

The section in the lower left of Figure 38 was produced by a 2-D by 2-D migration of the grid data. Most of the high angle events in the slope section have been removed, which facilitates an interpretation of the dipping reflectors associated with the mud volcano. It is now clear that reflectors in the slope have been disturbed by fluid migration, and the strong reflection evident immediately below the mud volcano is interpreted as a possible conduit for fluid flow. Although a significant amount of out-of-plane energy and improper focusing still remain in the image, the surface of the accretionary prism appears to have a shingled character indicating it is a densely thrust-faulted surface.

The lower right section in Figure 38 was migrated using a 3-D depth migration, then stretched to time for comparison. All of the out-of-plane energy appears to have been repositioned in the data, leaving a significantly less complicated section. The vertical resolution of the prism surface has finally been reduced to the width of the seismic wavelet, and individual fault surfaces can be identified. It is now evident that some of the fluid migration associated with the mud volcano is

originating in the wedge and is migrating along fault planes and into the overlying slope sediments.

The above interpretive sequence is offered as an example of the superiority of 3-D imaging in complicated geological environments. In addition to the imaging advantages accrued through 3-D migration, dense 3-D coverage facilitates a more complete interpretation than is possible when coverage is limited to a single profile or an areally sparse set of profiles. The availability of a large set of closely spaced profiles reveals lateral relationships in the structure which would otherwise be unknown. Fault planes and sediment deposition patterns can sometimes only be accurately interpreted using dense 3-D coverage. The availability of a 3-D grid of data also allows for interpretation of the geology using constant depth or time slices. Non-vertical slices through seismic data can facilitate an understanding of the geology that is not evident in conventional vertical sections. Likewise, the interpretive process can be augmented by displaying the data on a computer workstation.

Data Density and Image Resolution

In considering the Costa Rica survey, the question naturally arises as to what data density would have been sufficient to obtain the resolution necessary for proper interpretation. In the third chapter of this thesis I discussed how the choice of binning parameters was primarily motivated by a need to equalize the fold over the survey area while retaining as much spatial resolution as possible. In the second

chapter I demonstrated that the navigation was sufficiently accurate to have supported collection at twice the cross-line density used. However, limitations in the collection period would have then allowed acquisition over only half the area actually covered. Similarly, if the data had been collected with a coarser line spacing, the survey could have covered more of the accretionary prism area. Limited acquisition time and the cost of data acquisition are fundamental concerns, and they make the question of required data density an important one.

In the Costa Rica 3-D data, I cannot investigate the question of a finer resolution without producing gaps in the coverage and reducing the signal-to-noise ratio by decreasing the fold. I can, however, easily look at coarser resolutions by discarding parts of the data, then migrating the reduced data set. I performed this study by producing two additional 3-D depth migrations of the Costa Rica grid data, one using every other line of the data, and one using every third line.

Figure 39 shows the middle line of the Costa Rica data set after 3-D depth migration of the middle 32 lines of data, which had a line spacing of 0.05 km. In comparing this migration to migrations using sparser data grids, I will concentrate on the structures in the two areas indicated by boxes. One of these areas encompasses a section of the upper accretionary prism and the interface between the wedge and the slope cover. The other area details a structure within the accretionary prism.

Figure 40a is an enlargement of the left boxed area in Figure 39. The prism in this area appears to be composed of a highly deformed block on the right which displays imbricate faulting and is truncated against an underthrusted, bowed unit with an upper surface at 3.8 km (see interpretation, Fig. 40b). Figure 41a displays the same area as Fig. 40a after 3-D migration using a line spacing of 0.10 km. The

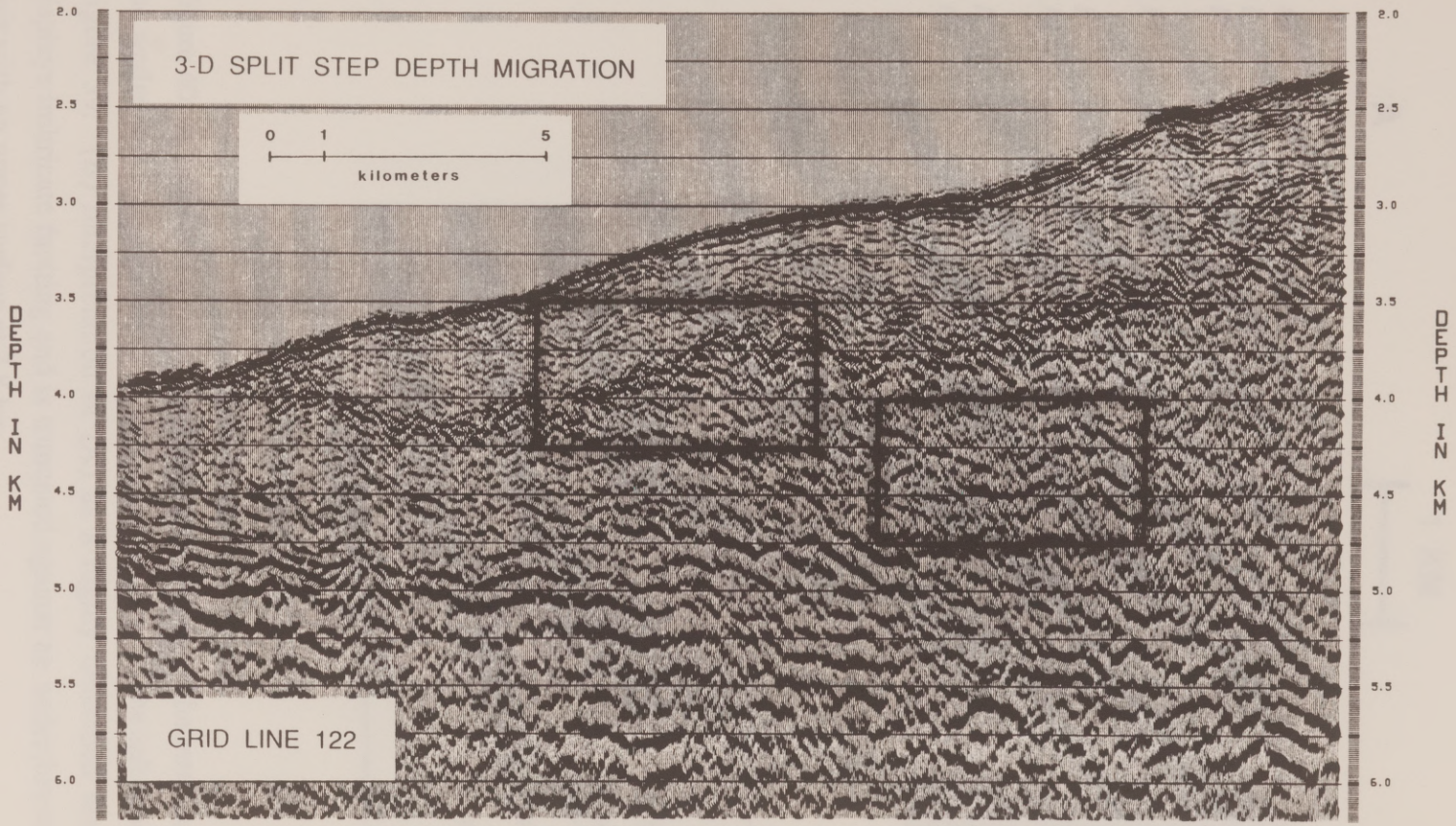

Figure 39. The middle line of the Costa Rica data set after 3-D depth migration of the middle 32 lines of data. Boxed areas will be examined more closely in the next several figures.

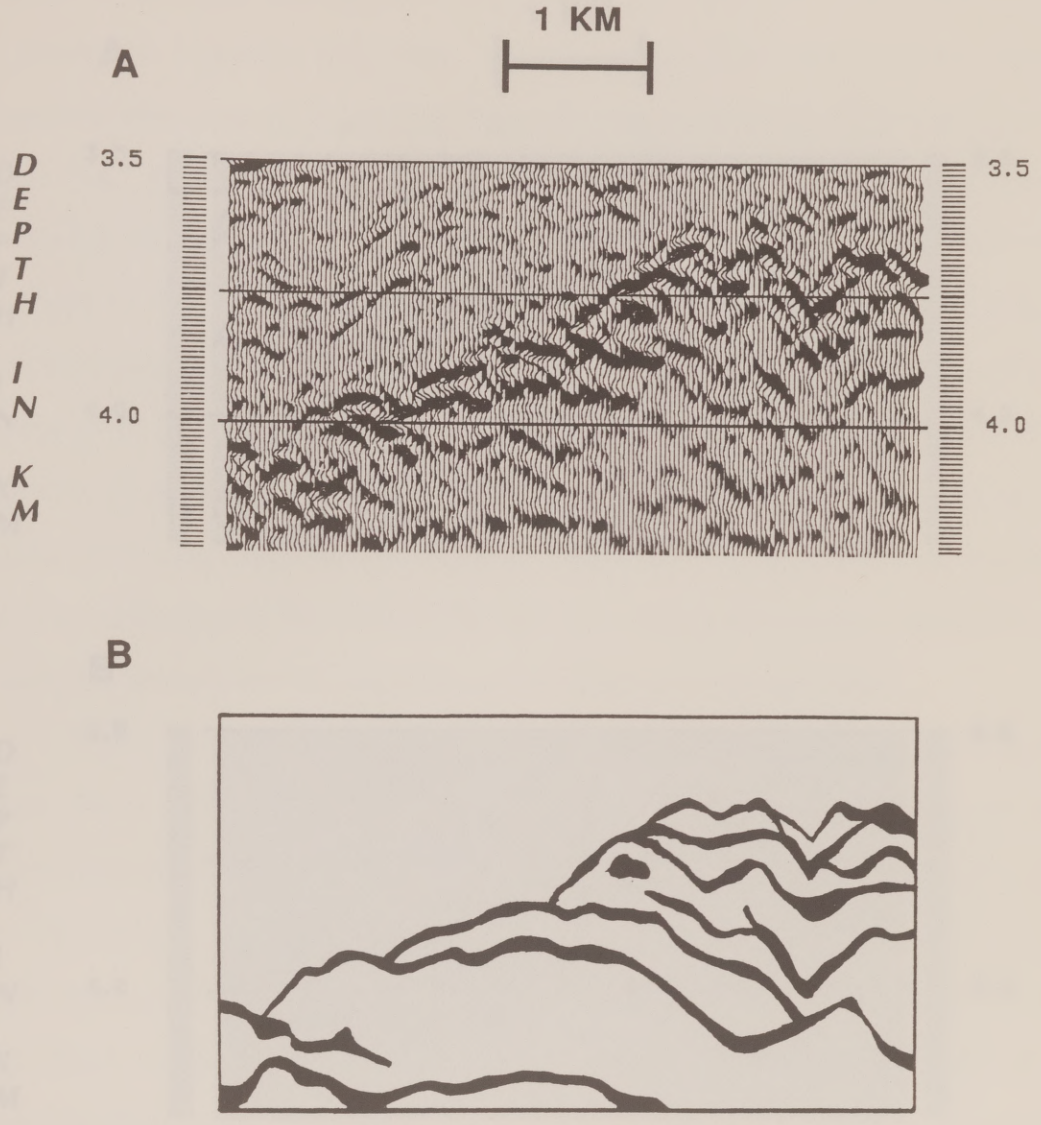

Figure 40. A section of the upper accretionary prism and the interface between the wedge and the slope cover. (A) An enlargement of the left boxed area in Figure 39. (B) Interpretation of (A) as a highly deformed block which displays imbricate faulting and is truncated against an underthrusted, bowed unit with an upper surface at 3.8 km.

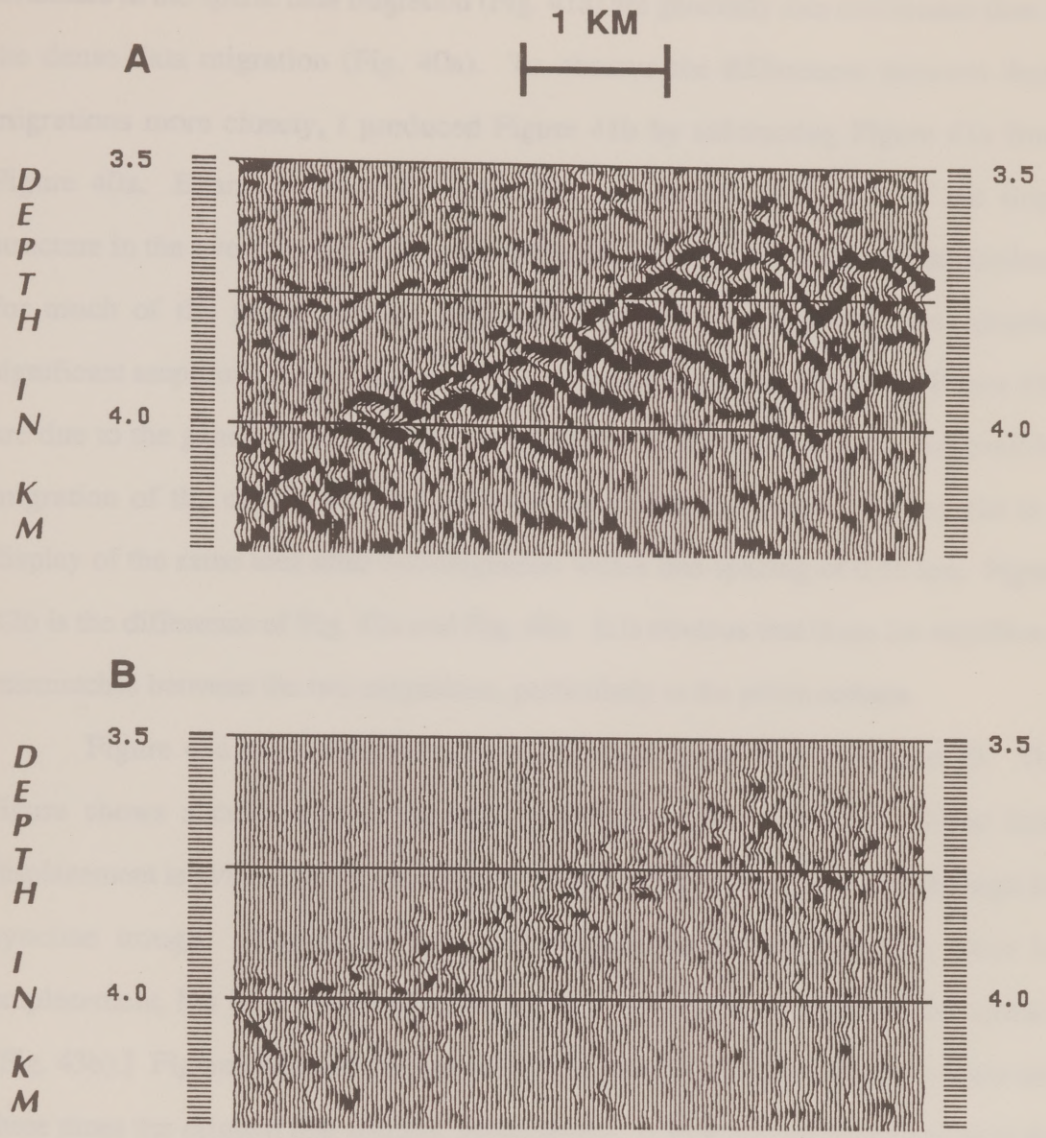

Figure 41. (A) The same area as Fig. 40a after 3-D migration using a line spacing of 0.10 km. The reflectors shown here are generally less continuous than in Fig. 40a. (B) Subtraction of Fig. 41a from Fig. 40a.

reflectors in the sparse data migration (Fig. 41a) are generally less continuous than in the dense data migration (Fig. 40a). To observe the differences between these migrations more closely, I produced Figure 41b by subtracting Figure 41a from Figure 40a. Examination of the difference plot shows that much of the slope structure in the two migrations is essentially identical. Differences are also minimal for much of the prism surface, although some parts of the reflectors display significant amplitude discrepancies. Most of the differences indicated by Figure 41b are due to the generally sharper focus and higher signal-to-noise ratio achieved by migration of the denser data set, particularly within the prism. Figure 42a is a display of the same area after 3-D migration with a line spacing of 0.15 km. Figure 42b is the difference of Fig. 42a and Fig. 40a. It is obvious that there are significant mismatches between the two migrations, particularly at the prism surface.

Figure 43a is an enlarged plot of the right boxed area in Figure 39. The figure shows a cross-section through a syncline / anticline pair. Some fault displacement is evident along the crest of the anticline, and possibly also through the syncline trough. [I interpret this as a remnant thrust sheet which, since its emplacement, has been underplated and shorten by high angle faulting and rotation (Fig. 43b).] Figures 44a and 45a are taken from the migrations using two times and three times the original line spacing, respectively. A progressive deterioration in the coherency of the reflectors is evident. Subtracting the plots of the sparse migrations from the plot of the dense migration shows the associated signal losses (Figs. 44b and 45b). The increased noise level in Figure 45b is particularly noticeable. As the line spacing became coarser, a higher percentage of the energy associated with prism

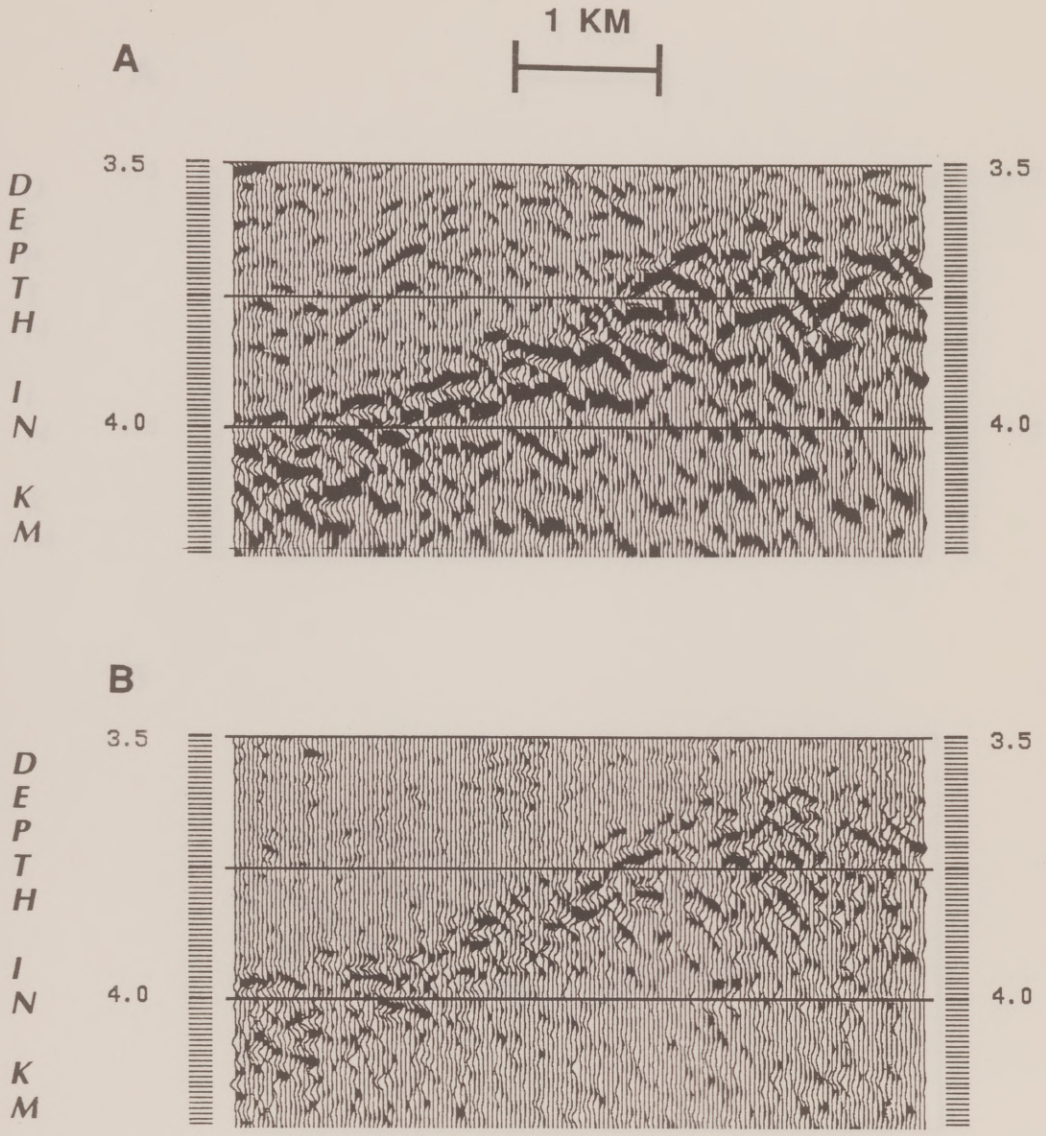

Figure 42. (A) The same area as Fig. 40a after 3-D migration using a line spacing of 0.15 km. (B) Subtraction of Fig. 42a from Fig. 40a. There are significant mismatches between the two migrations, particularly at the prism surface.

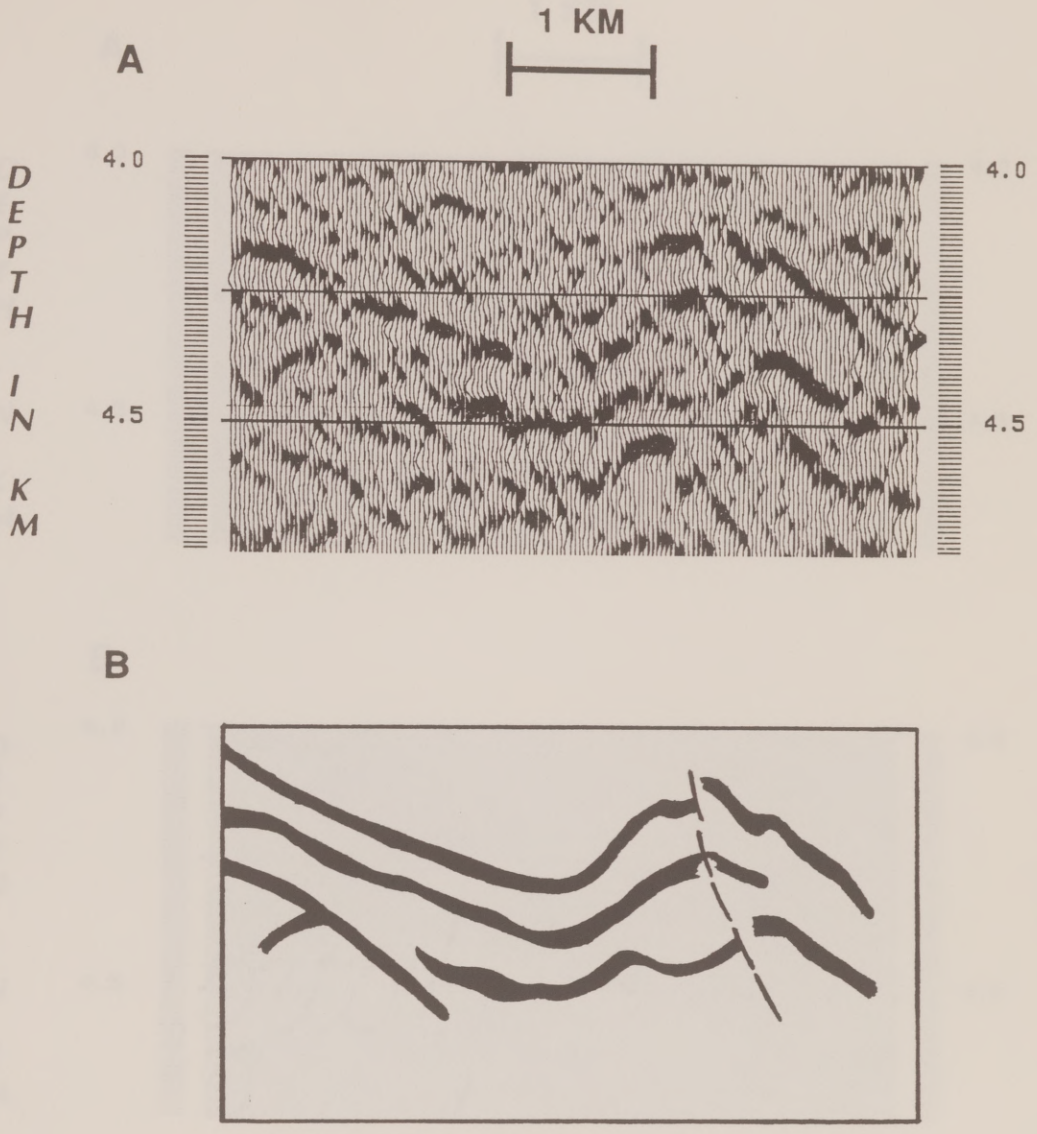

Figure 43. (A) An enlarged plot of the right boxed area in Fig. 39. Pictured is a cross-section through a syncline / anticline pair. (B) Interpretation of Fig. 43a as a remnant thrust sheet which, since its emplacement, has been underplated and shorten by high angle faulting and rotation.

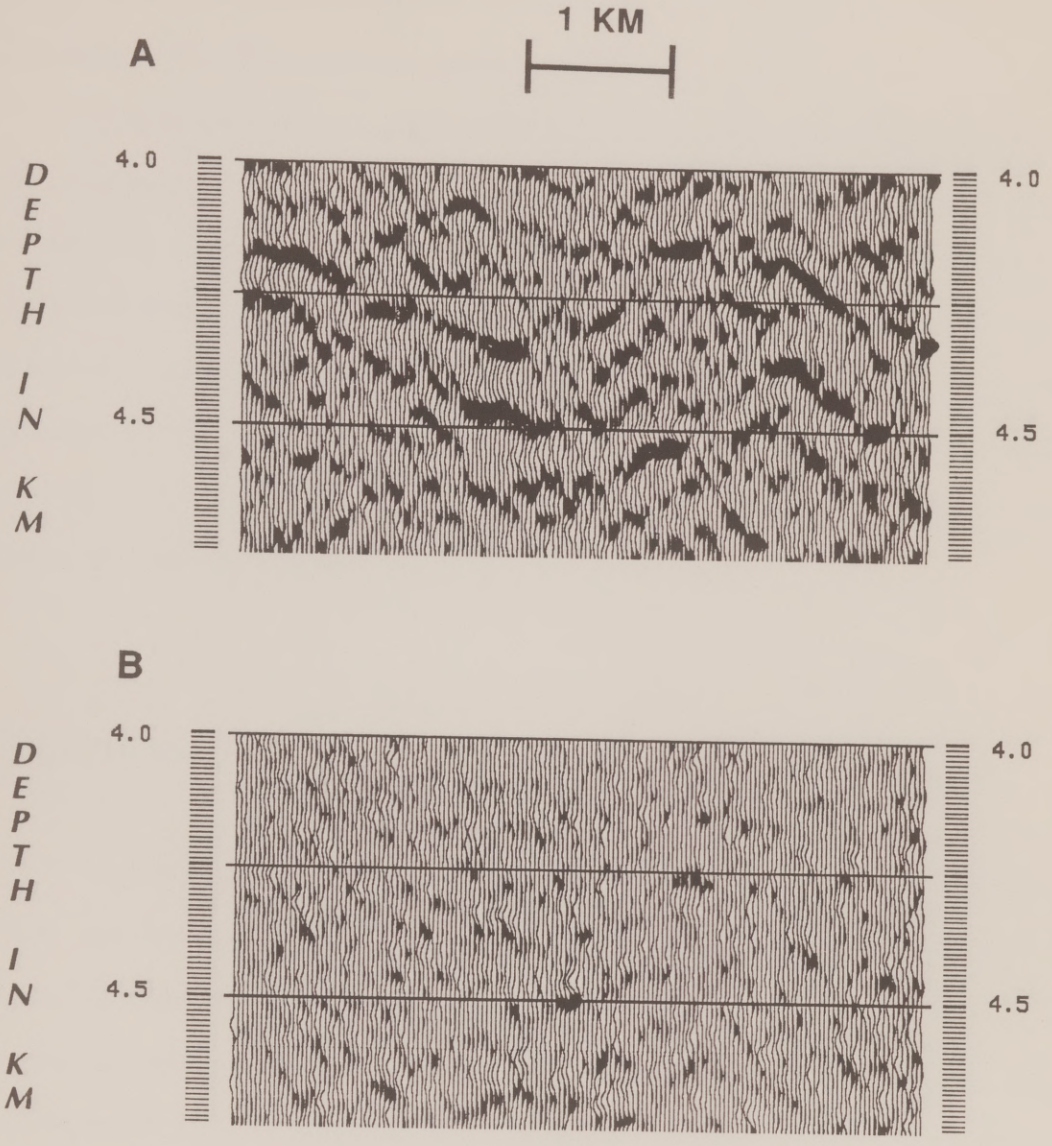

Figure 44. (A) The same area as Fig. 43a after 3-D migration using a line spacing of 0.10 km. (B) Subtraction of Fig. 44a from Fig. 43a.

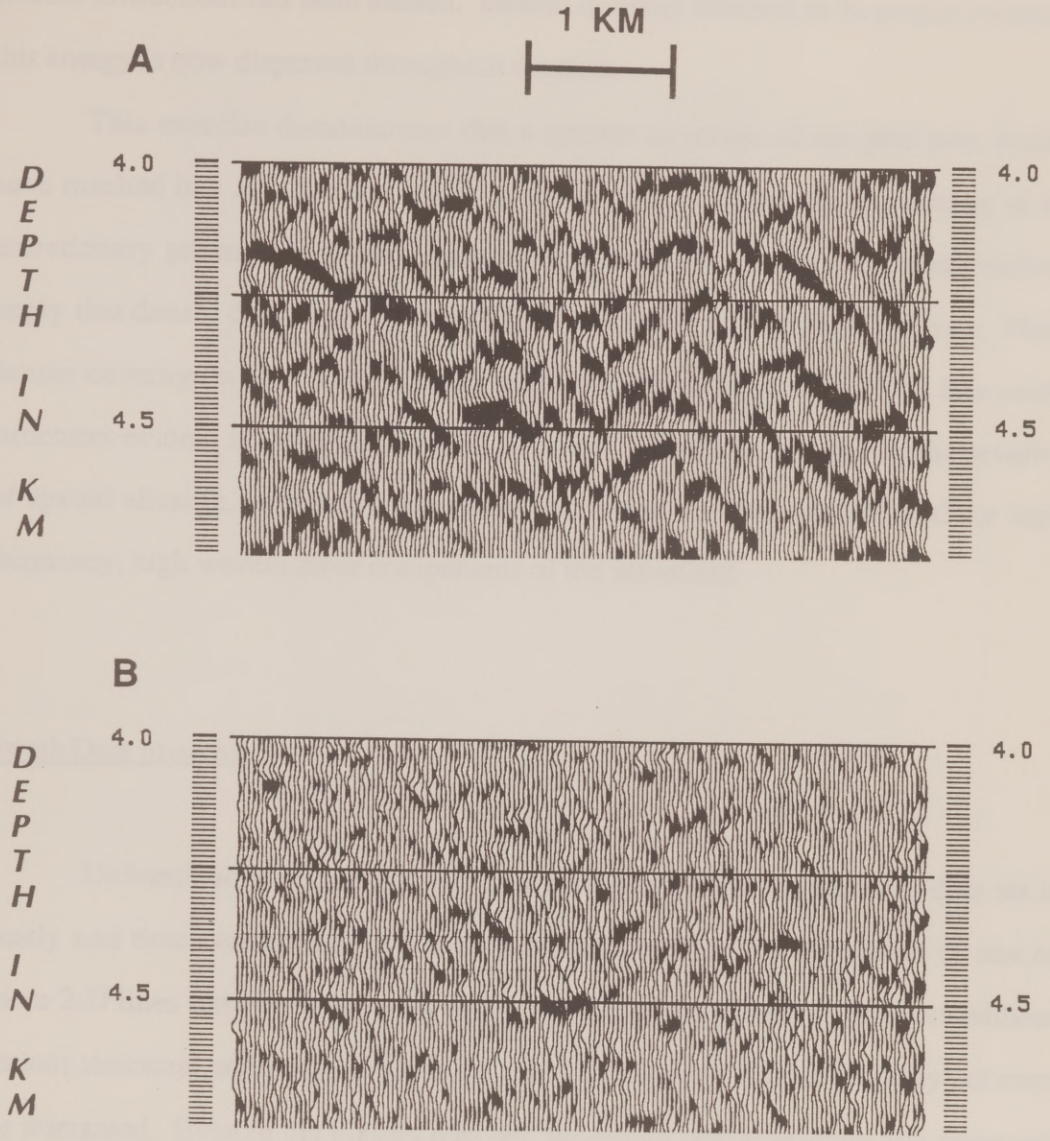

Figure 45. (A) The same area as Fig. 43a after 3-D migration using a line spacing of 0.15 km. (B) Subtraction of Fig. 45a from Fig. 43a. The increased noise content is particularly noticeable.

surface diffractions has been aliased. Instead of being returned to its proper position, this energy is now dispersed throughout the data.

This exercise demonstrates that a sparser coverage of the grid area would have resulted in a less focused image of the structure. Given the complexity of an accretionary prism, this is not a surprising conclusion. In fact, my observations imply that denser data coverage would have produced an even better image. First, denser coverage would have allowed more detailed observation of the fine-scale structures evident at the prism surface. Second, it would have lessened the severity of spatial aliasing, preventing the contamination which was experienced for high frequency, high wavenumber components of the wavefield.

Swath Data Imaging

Unfortunately, acquisition and processing of a three dimensional data set is costly and time consuming. A swath reconnaissance survey composed of one or more 2-D lines may in some cases be a cost effective alternative. In areas without serious structural variations along strike, three dimensional acquisition may not even be warranted. Even in the present data set, the strong lateral velocity and structural variations occur predominantly in the dip direction.

Figure 46 shows 33 km of swath line 50, the middle swath line, after 2-D migration. This line approximately overlies the middle grid line. The swath data were stacked and migrated with a trace spacing of 0.0167 km, giving the swath data nominally half the fold of the grid data. In producing the display, every two adjacent

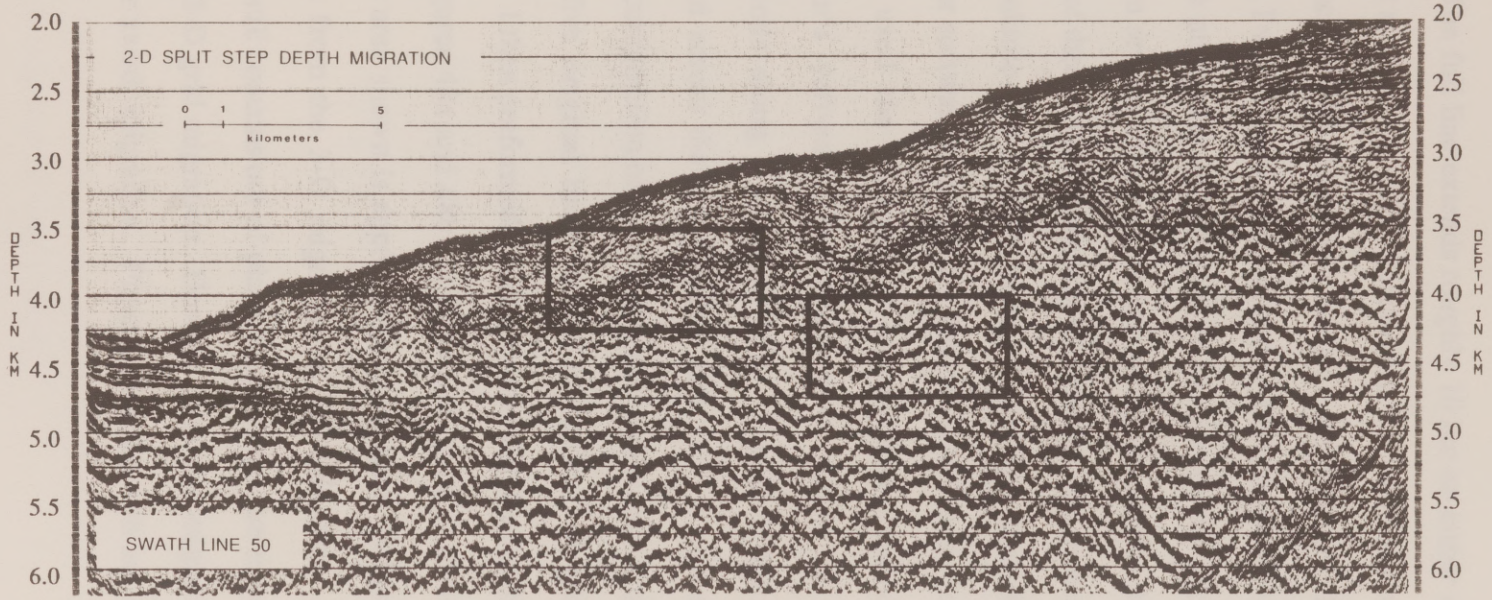

Figure 46. 33 km of swath line 50, the middle swath line, after 2-D depth migration. This line approximately overlies the middle grid line.

traces were summed so that the character of the section is similar to that of the grid displays. The full line extends roughly 10 km on either side of the display, but for the present study, I am only interested in the area shown. The two boxed areas in Fig. 46 enclose the same structures as the boxes in Fig. 39. As part of this discussion, I will compare the grid and swath images of these structures.

The proximity and parallel orientation of the middle five swath lines were exploited in several experiments attempting to enhance the swath image. The most ambitious of these experiments was the creation of a sparse three dimensional data set from the middle five stacked, unmigrated swath lines (Figure 47). I used CGG's Geovecteur software to resort the stacked swath data into cross-line CMP gathers, and then used the Geovecteur interpolation routine to produce new data. Geovecteur's software interpolates new traces on the basis of coherency investigations along a range of dips. For each dip investigated, a model is constructed across the interpolation interval. A new trace is then built from a weighted composition of the dip models. After resorting, eight new lines together with the five original lines formed a regular 3-D grid with a line spacing of 0.125 km. I then performed a 3-D split step depth migration.

Figures 48a and 48b are from 2-D and 3-D depth migrations of the swath data. The area shown is approximately the same as that shown in Fig. 40, which was taken from the 3-D migration of the grid data. Although the 3-D swath migration still contains out-of-plane energy, there are significant similarities between it and the 3-D grid migration. However, the grid migration result is better focused than either swath migration. Figures 49a and 49b are swath images of the same

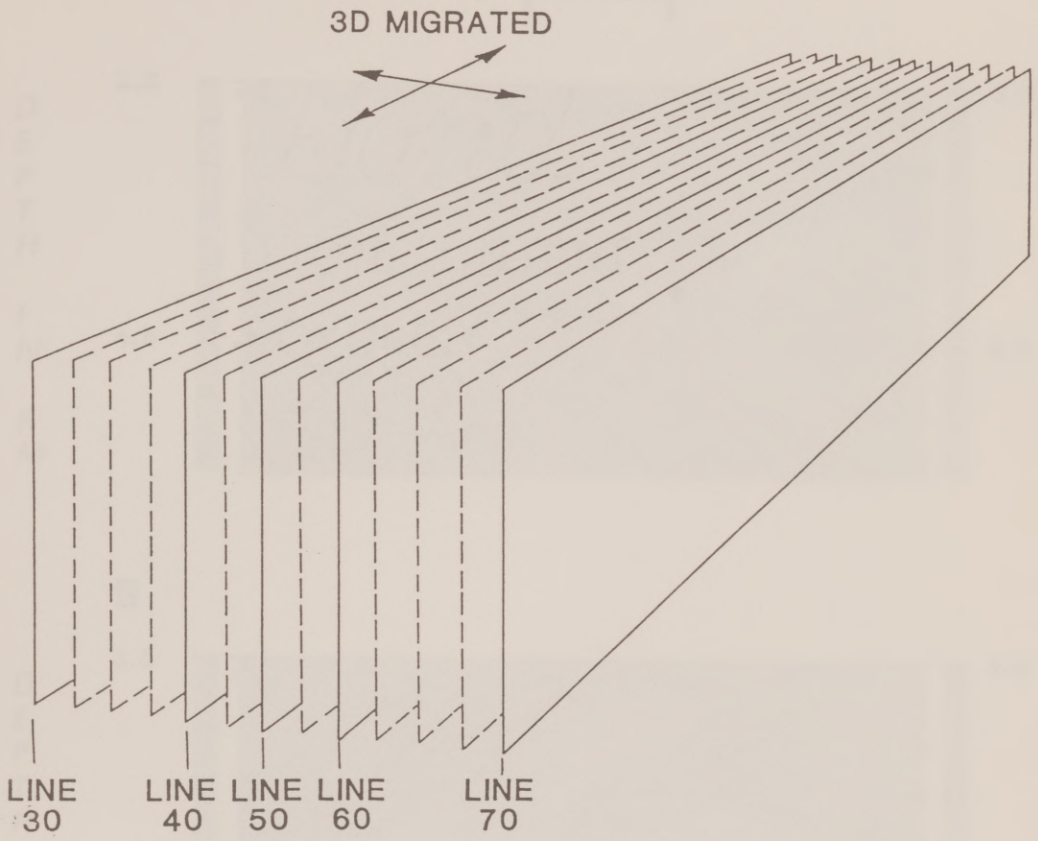

Figure 47. Schematic of 3-D swath migration process. The five center swath lines were interpolated so that the line spacing was 125 meters, and the data were 3-D migrated directly to depth.

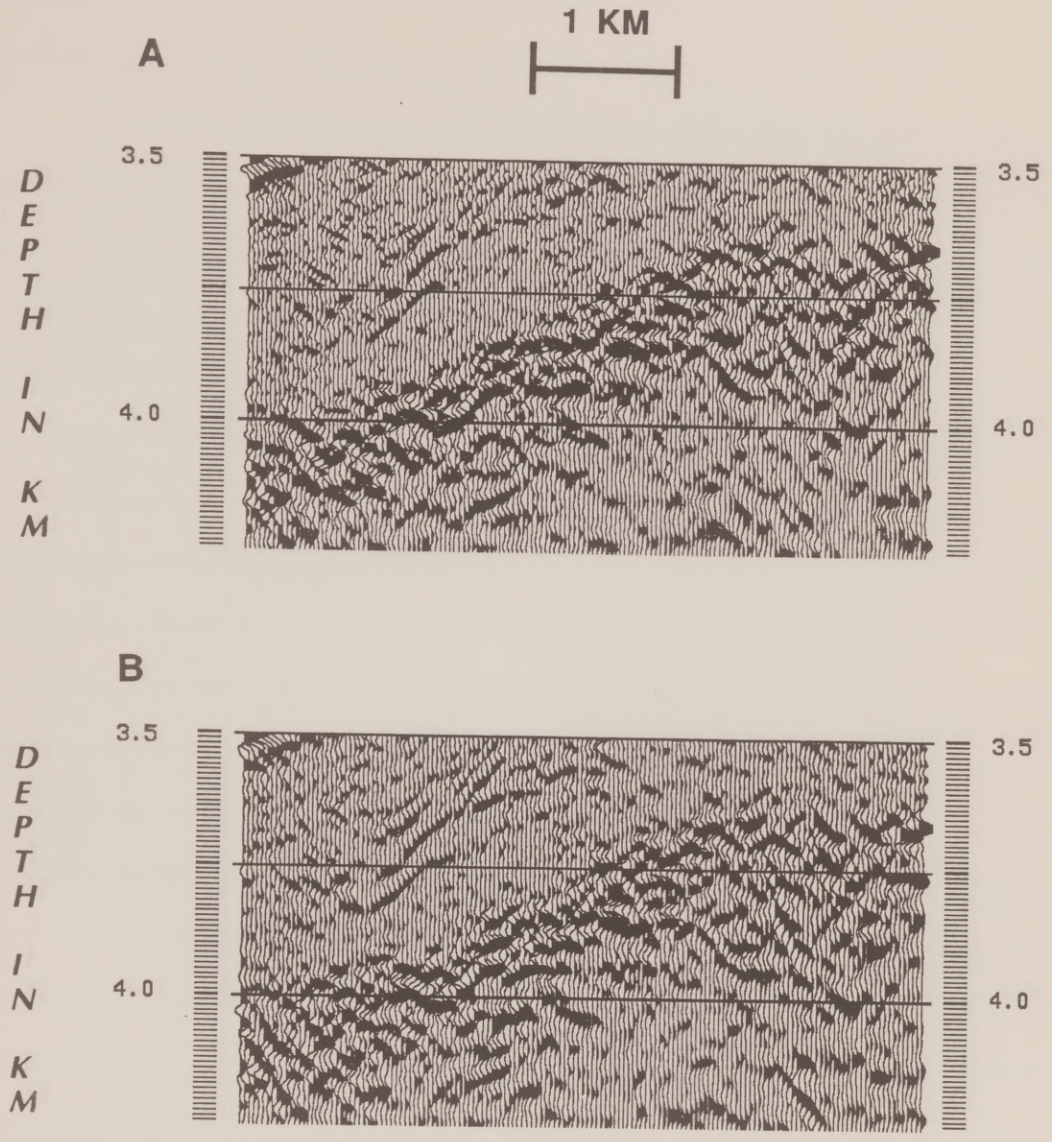

Figure 48. (A) 2-D and (B) 3-D depth migrations of the swath data. The area shown is approximately the same as that shown in Fig. 40, which was taken from the 3-D migration of the grid data. The 3-D swath migration has improved some reflector positions, but it still contains significant out-of-plane energy.

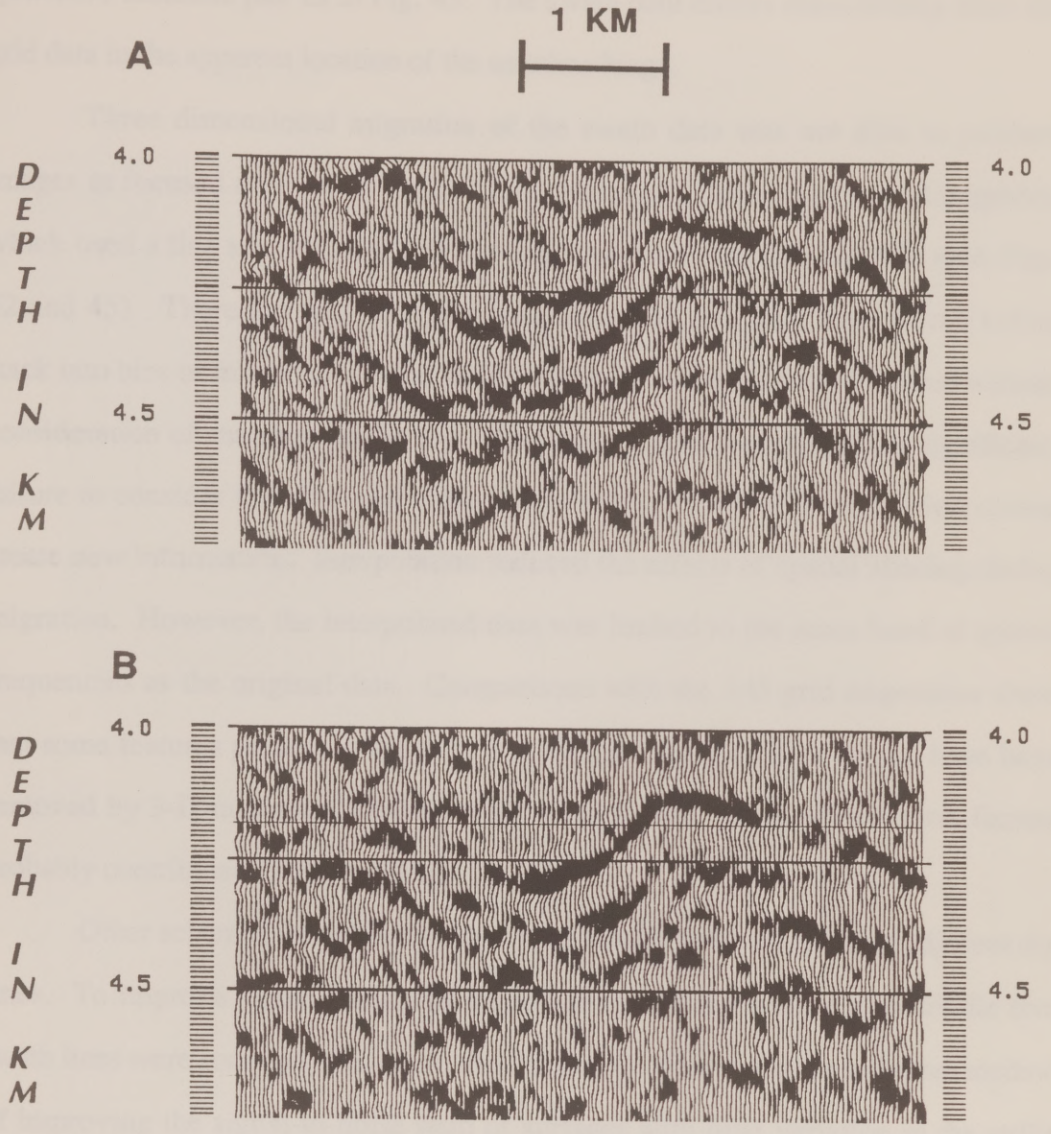

Figure 49. (A) 2-D and (B) 3-D swath images of the same syncline / anticline pair as in Fig. 43. The swath data differs considerably from the grid data in the apparent location of the anticline hinge.

syncline / anticline pair as in Fig. 43. The swath data differs considerably from the grid data in the apparent location of the anticline hinge.

Three dimensional migration of the swath data was not able to produce images as focused as those of the 3-D grid migrations, including the grid migration which used a line spacing of 0.150 km (e.g., compare Figs.48b and 49b with Figs. 42 and 45). There are two main reasons. First, the grid data were sorted before stack into bins of limited cross-line width, while the swath data were stacked without consideration of streamer feathering. Because streamer feathering was significant, failure to consider it introduced cross-line smearing. Second, interpolation cannot create new information. Interpolation reduced the effects of spatial aliasing during migration. However, the interpolated data was limited to the same band of spatial frequencies as the original data. Comparisons with the 3-D grid migrations show that some features present in the 2-D swath migrated data which should have been removed by 3-D migration were actually strengthened. Both of the above factors probably contributed to this problem.

Other schemes for enhancing the swath image involved stacking adjacent dip lines. To improve signal quality in the lower part of the section, the middle five swath lines were summed after stack, then migrated. This can be an effective method of improving the signal-to-noise ratio of surfaces with little variation in the strike direction. In this case, the operation did produce a modest improvement in portions of the basement reflector, but most of the image was degraded. Next the same five lines were summed together after individual depth migrations with the same velocity function. Figure 50b shows the result near the toe of the wedge where the slope cover pinches out. For comparison, Figure 50a is the 2D migration of swath line 50

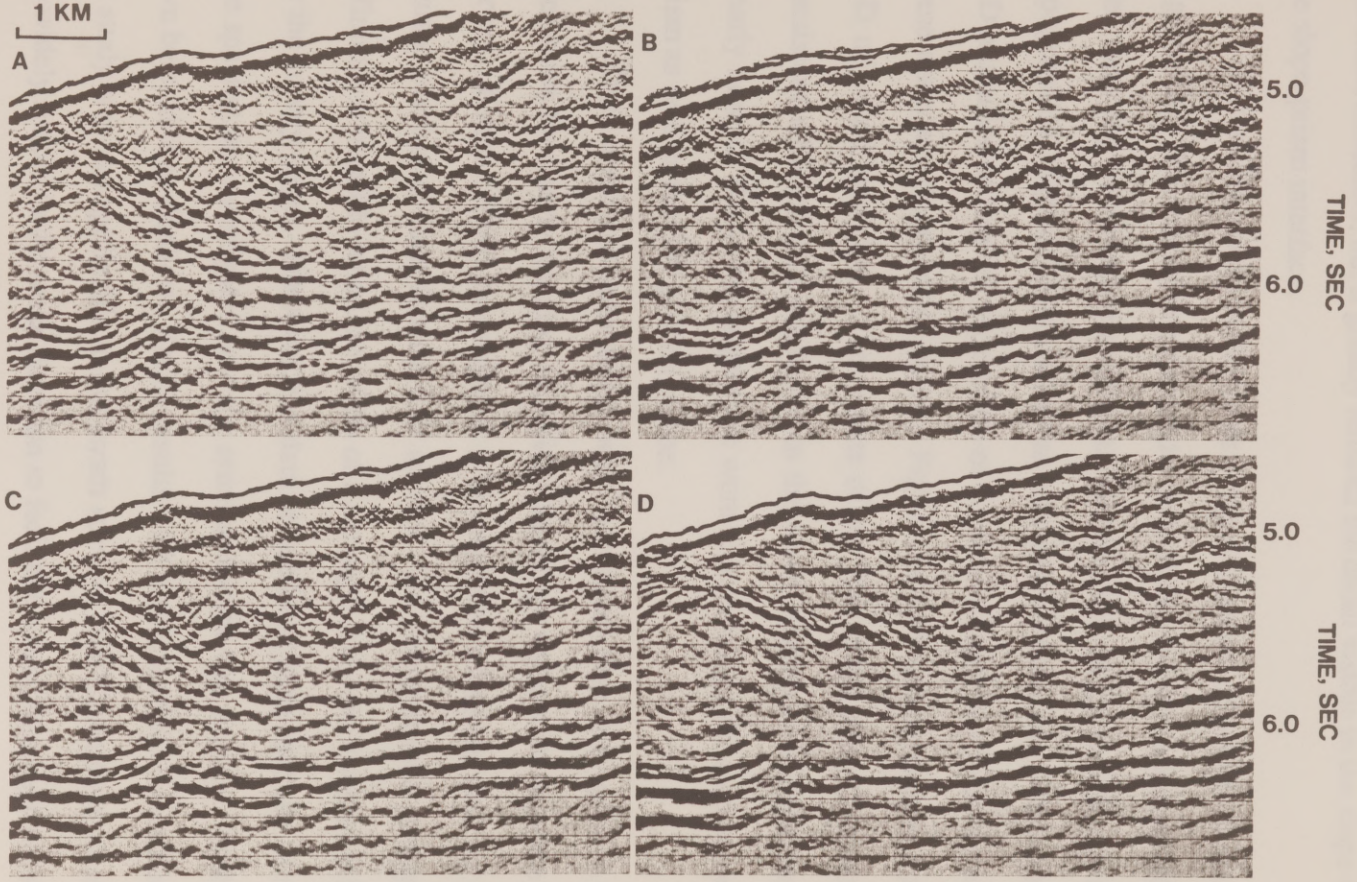

Figure 50. Examples of swath data processing techniques. (A) 2-D migration of swath line 50 near the toe of the wedge. (B) Summation of the five middle swath lines after 2-D migration. (C) 3-D swath migration in the same area as Fig. 50a. (D) The corresponding area of the 3-D migrated grid data.

in the same area. The summation operation greatly improved the continuity of the basement reflectors, but it greatly reduced the detail visible in the slope section and at the slope-prism interface.

Figure 50c displays the result of the 3-D swath migration in the same area as Figure 50a. This migration produced a better image of the basement reflector in this area than any of the other swath data migrations. In particular, the image of the topographical high in the basement has been sharply focused. When compared to the 2-D migration of line 50, the surface of the accretionary prism has been improved in some areas and degraded in others. Figure 50d is the corresponding portion of the 3-D migrated grid data. The results of the 3-D swath migration are reasonably consistent with the grid migration in the lower portion of the section. However, clearly none of the swath migrations were able to image the slope cover and upper prism as well as the 3-D grid migration.

Data configurations which were not tested here may offer a more viable alternative for clearly imaging complicated geology without the expense of a full 3-D survey. Krebs (1990) investigated 3-D migration of swath data by extracting a limited portion of data from a 3-D survey. He demonstrated that good seismic definition is possible when the width of a survey is only one-fourth the Fresnel zone for the survey target. However, the data he used had been spatially binned, and the line spacing he investigated was the same as for the full data set. Although I may have been able to duplicate Kreb's results with a subset of the Costa Rica grid data, his study was not applicable to the swath survey. The Costa Rica swath data were too widely spaced in the strike direction to facilitate spatial binning comparable to that of the grid data.

Chapter 5: Conclusion

This thesis examined the imaging potential of the UTIG 3-D Costa Rica seismic data. It presented a partial documentation of both the data acquisition and processing, with an emphasis on how each could be improved. With respect to data collection, the small scale structural complexities prevalent in the Costa Rica accretionary environment could have been better resolved with denser spatial sampling. To significantly improve the image of the 3-D data over that which has been produced to date would require the application of prestack processing techniques to alleviate the deficiencies inherent in CMP stacking.

Navigation

Accurate navigation is a necessity for a successful 3-D seismic survey. Navigation is important to both the data acquisition and processing. During acquisition, the performance of the ship's navigation system limits the effective density at which the data can be collected. Afterwards, errors in determining the streamer configuration degrade the spatial resolution of the processed seismic image.

In the second chapter, I demonstrated that the internal consistency of the primary navigation system was excellent for the Costa Rica experiment. Because the internal consistency included the effects of recursive filtering, it was difficult to assign a quantitative value to these statistics. However, recursive filtering increases

the navigation's response time for reflecting the ship's true motion. If the navigation had been overfiltered, the ability to steer the ship along a predetermined course would have suffered. Therefore, the ability of the *Fred Moore* to maintain its on-line position with a standard deviation of 11 meters was a reflection of both the ship's maneuverability and the accuracy of the navigation system.

A more formal measure of the consistency of the land based navigation was possible because of the availability of GPS navigation. I used the GPS data to independently measure the accuracy of the Maxiran navigation by assuming that neither system suffered serious problems due to grid wandering or distortion. Given these assumptions, statistical comparisons showed that the Maxiran measurements had an RMS uncertainty of not more than 5.1 meters. Based on these results, I conclude that the navigation probably would have allowed acquisition with a 50 meter line spacing (half the spacing that was actually used) without producing gaps in the acquisition grid. Because of limitations involving acquisition time and cost, however, the experiment would then have been confined to half of the area that was surveyed.

Although navigational accuracy was not a critical factor in the success of the swath data collection, the study of the swath navigation was instructive in demonstrating the importance of location to the success of the 3-D survey. In the future, this type of seismic survey will continue to be feasible only in limited areas unless global satellite navigation becomes available to general users on a continuous basis.

The streamer configuration was determined from the readings of magnetic compasses within the streamer. Errors in modeling the streamer curvature from

these measurements were not a significant problem since the streamer usually attained a linear configuration shortly after the ship came on-line. A previous study of these compasses demonstrated that they were capable of determining the streamer shape with cross-line errors of 5 to 10 meters when the magnetic declination was well known. However, an error in the magnetic declination correction can significantly effect the accuracy to which the streamer orientation is known. This is a problem that can be complicated by significant streamer feathering, like that which was experienced during the Costa Rica survey. Even taking these problems into consideration, though, it can still be reasonably assumed that most receiver positions were located within 20 meters of their true cross-line positions.

CMP Binning and Stacking

In binning the seismic data, it was important to maintain an even fold so that the signal-to-noise content was low throughout the stacked data. When a single trace of the stacked data has a higher relative noise content than surrounding traces, that noise will contaminate adjacent data during poststack migrations. It was also necessary to maintain an even fold for all offset representations so that the characteristics of the reflectors in the stacked data were consistent across adjacent traces. In the third chapter, I presented the results of studies that were employed to determine the optimum bin size and grid orientation for CMP binning of the data. In binning the seismic data, the goal was to maintain an even fold while also minimizing the bin size to retain a high spatial resolution. The parameters which were chosen for

the final binning grid defined rectangular bins which were 33 meters long in the dip direction and 50 meters wide along strike.

In discussing CMP binning, I also discussed the validity of stacking on the basis of CMP position. I examined a simplified geometry which was representative of the average seafloor depth and dip in the grid area and documented the differences in CMP positions and reflection positions for representative near and far offsets. With no streamer feathering, near and far offsets which shared the same source-receiver midpoint actually had seafloor reflection points which differed by almost two bin lengths in the dip direction. When consideration of a worst case scenario of 25° streamer feathering was included, the maximum separations were more than three bin lengths in the dip direction, and two and a half bin widths along strike. Variations in the angles of streamer feathering, then, may have significantly increased the spatial smearing caused by CMP binning of the data. It is difficult to apply this analysis to reflectors beneath the seafloor because of their more complex structure; however, these results still give a qualitative measure of the inherent deficiencies of CMP geometries. Although this type of error decreases with increasing depth, the thickness of the slope sediment in the grid area does not significantly decrease the CMP spatial smearing at the top of the accretionary prism.

The study of simple structural geometries demonstrated that the spatial smearing introduced into the Costa Rica 3-D data during CMP processing was much greater than that introduced by navigational inaccuracies. Alternate processing sequences incorporating either dip move-out and stack or a 3-D prestack migration would have introduced less spatial smearing into the data than was introduced by CMP processing.

Poststack Migration

The stacked Costa Rica seismic data were dominated by strong diffractions created by the rough surfaces of the seafloor and the slope sediment / accretionary wedge interface. Poststack migration was required to provide an interpretable image. Because of the complex structures in the accretionary prism and the complicated nature of the velocity field, it was necessary for the migration algorithm to accurately collapse diffractions in the presence of severe velocity perturbations.

In the fourth chapter I presented a short overview of poststack migration algorithms and compared examples of the Costa Rica data after various poststack migrations. The physics of poststack data is described by the constant-density acoustic wave equation, although the wave equation must be modified so that it is consistent with the exploding reflector model. In the first section of the fourth chapter, I outlined derivations for both finite difference and phase shift implementations of migration, and I described the assumptions implicit in both methods. Comparisons of finite difference and split step depth migrations showed that the phase shift operator did a better job of removing high-angle diffractions from the data despite the approximate representation of the velocity model employed by its diffraction term. Because the split step operator retained all spectral contributions during migration, the split step migration results displayed more severe spatial aliasing than the data which were migrated by finite difference methods. However,

by applying spatial filtering after split step migration, I was able to reduce high frequency, high wavenumber noise in the final image.

The next section of the fourth chapter reviewed migration implementations known as time migrations. The migrated results are usually displayed as functions of vertical two-way travel time rather than depth. Time migrations do not properly position reflectors in areas with laterally varying velocity structures because integral, phase shift, and finite difference time migrations all disregard ray bending within each migration interval. Although time migrations can provide a reasonably good image in areas where lateral velocities vary slowly, examples of time and depth migrations of the Costa Rica data show that, because of rapid velocity gradients, depth migration is needed for accurate imaging in this area.

Another requirement for proper imaging of the Costa Rica data was 3-D migration, which was necessary because of the three dimensional structure of the accretionary margin. In the third section of Chapter 4, comparisons of a variety of finite difference migrations demonstrated the advantages of properly accounting for 3-D variations during imaging. For the same data, 2-D, 2-D by 2-D, and full aperture 3-D migrations allowed progressively better interpretations of a mud volcano in the slope sediment above the accretionary wedge.

After establishing that 3-D depth migration was necessary to properly image and interpret the Costa Rica data, I examined the relation between data density and image accuracy. The image degradation suffered in going from a 0.05 km bin width along strike to a 0.10 km bin width was not nearly as bad as that introduced by increasing the bin width to 0.15 kilometers. This may have been indicative of the spatial smearing introduced by trace duplication during binning. However, the

increase in the severity of spatial aliasing was apparent with any increase in the bin width. This exercise demonstrated that a sparser coverage of the grid area would have resulted in a less focused image of the structure, thereby allowing a less accurate interpretation.

In the final section of the fourth chapter I discussed attempts to enhance the swath data images by peusdo three dimensional processing. The methods which I experimented with included 2-D migration and cross-line stack of the middle five swath lines, and the interpolation of a 3-D grid of seismic data from swath lines so that a full aperture 3-D migration could be performed on the interpolated grid. None of the swath data processing techniques were able to produce images as focused as those from the 3-D grid migrations. Even the grid migration using a line spacing of 0.15 km provided better spatial resolution than the 3-D swath migration. Reasons cited for this failure included smearing of the swath data during brute stack, and inaccuracies in the 3-D data interpolation technique.

Migration Velocities

In concluding this thesis, I would like to stress the importance of using correct migration velocities to obtaining a proper image. In comparing migration results, I implicitly assumed that the migration velocity function was correct, and that the resulting image was the best that the combination of seismic data and migration algorithm could provide. However, velocities were only weakly constrained during processing. For reasons of economy and time, most of the iterative migration

velocity analysis was performed using 2-D finite difference time migrations of the data. Image quality in the lower portions of the prism was insensitive to even gross changes in the deeper interval velocity structure. At the slope / prism interface, it was often not possible to confidently determine what velocity function provided the most focused image.

A better velocity model might produce an improved image after 3-D migration. In areas with little structural variation along strike, large offset data can provide excellent velocity control. Large offset data is typically collected using ocean bottom seismograms or hydrophones to record data as a ship approaches, then passes over its position. In the Nankai Trough accretionary environment, high resolution velocity estimates were obtained from large offset data collected along strike during two ship experiments (Stoffa et al., 1991b). The Nankai Trough accretionary region exhibits far less structural variability in the strike direction than is the case with the Costa Rica margin area. In the Costa Rica region, the results from large offset data would have been more adversely affected by the rough surface of the Costa Rican accretionary prism. However, such data would have been valuable even if they had only coarsely constrained the seismic velocities.

Another option for improving velocity estimates may lie in the use of iterative prestack migration. Faye and Jeannot (1986), describe a method of performing focusing depth analysis during prestack migration. The results of the focusing analysis can be used to update the migration velocity model before the next prestack migration iteration is performed. In future research, I plan to investigate iterative 2-D prestack migration as a means of obtaining a more accurate velocity model for subsequent 3-D poststack migration of the Costa Rica seismic data.

Appendix 1: Specifications for the University of Texas Recording System and Sound Sources as used in the Costa Rica Project

RECORDING SYSTEM

GUS 4200 Marine System:

- 96 MCS data channels, 90 dB gain ranging in 6 dB steps
- 16 auxiliary channels with full gain ranging for depth and waterbreak detectors, quality control testing, sonobuoy recording
- Fully demultiplexed recording in SEG-D at 6250 bpi
- 12 sec records at 4 msec
- Extended headers for logging peripheral data
- Filtering: low cut: out
  high cut: 86.5 Hz

DATA LOGGER

PDP 11/34 Based System for:

- Recording peripheral data on $^1/_2$" magnetic tape at 1600 bpi
- Navigation plotting
- Serial/parallel interfaces for supplementary navigation, gravity, magnetics or other input/output as required

SOUND SOURCES

Sources:

- Bolt 1900C air guns (20)
- Bolt 1500C air guns (6)

High Resolution Source Array:

- Volume: 1065 cubic inch tuned sub-arrays (2), six guns per array; 60, 78, 108, 150, 240 and 429 cubic inch each; only one array used at a time.
- Output: 25 bar-meters, 0-128 Hz, each array
- Bandwidth: ± 3 dB, 8-80 Hz
- Primary-to-bubble ratio: 7:1

Gun Fire Control:

- Aircon® III

Appendix 2: Spatial Aliasing and Spatial Filtering

In the fourth chapter, I mentioned that a consideration of spatial aliasing was important to discussions of data density and image resolution. In this appendix I document the subjects of spatial aliasing and spatial filtering more thoroughly, as well as documenting the spatial filters I applied after split step migrations of the Costa Rica data.

Spatial aliasing is a consequence of the discretization of the data in time and space. Variables that determine the threshold at which spatial aliasing becomes significant include the background velocity, the trace spacing along various orientations, and the apparent dip of geologic structures along those orientations. Spatial aliasing is most easily demonstrated in the frequency domain. To help in developing an intuitive understanding of spatial aliasing, I will first reiterate some of the relations between x-t space and k_x-ω space.

Given a set of monochromatic seismograms of identical phase in x-t space, the associated wavefield maps to the single point in k_x-ω space at (k_x=0, ω=constant). If the phase of each progressive seismogram is shifted by a regularly increasing increment, all of x-t space still maps to a single point in k_x-ω space. However, that point is no longer on the k_x axis, but is at some other constant wavenumber value.

Figure 51a shows a dipping reflector in x-t space. Like the monochromatic case cited above, the angle of incidence of the wavefield with the surface is a constant. Unlike the monochromatic case, the reflector contains all frequencies from

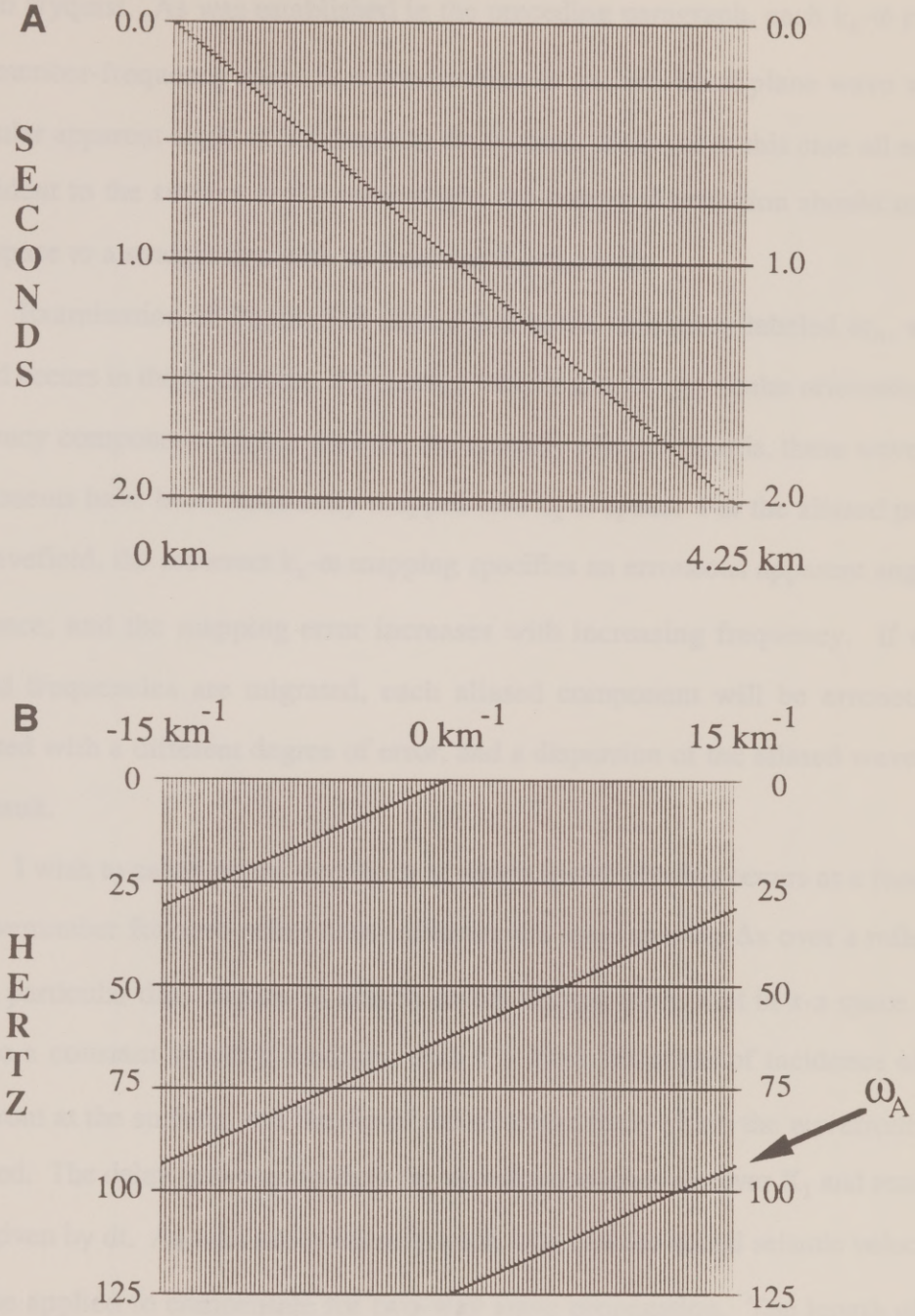

Figure 51. (A) A dipping reflector in x-t space. (B) The energy distribution of (A) in k_x-ω space. At the frequency labeled ω_A, wrap-around occurs in the k_x domain.

zero to Nyquist. As was established in the preceding paragraph, each k_x-ω pair in wavenumber-frequency space is representative of an individual plane wave with a particular apparent angle of incidence to the surface. Because in this case all energy is incident to the surface at the same angle, the energy distribution should map in k_x-ω space to a straight line with its origin at (k_x=0, ω=0).

Examination of Figure 51b shows that at the frequency labeled ω_A, wrap-around occurs in the k_x domain. For energy traveling at this particular orientation, all frequency components higher than ω_A are spatially aliased; that is, these wavefield components have been incorrectly mapped into k_x-ω space. For the aliased part of the wavefield, the incorrect k_x-ω mapping specifies an erroneous apparent angle of incidence, and the mapping error increases with increasing frequency. If these aliased frequencies are migrated, each aliased component will be erroneously migrated with a different degree of error, and a dispersion of the aliased wavefield will result.

I wish to calculate the frequency at which spatial aliasing occurs as a function of wavenumber for zero-offset data collected at a trace spacing Δx over a reflector with a particular dip. Figure 52 depicts an up-coming wavefront in x-z space. If I assume a constant velocity medium, then θ is both the angle of incidence of the wavefront at the surface, and the dip of the structure from which the wavefront was reflected. The delay between the time the wavefront reaches receiver X_1 and receiver X_2 is given by dt. As with poststack migration, one-half the actual seismic velocities must be applied to compensate for two-way wave propagation. The length of the stippled line segment in Figure 52, then, is given by (dt v/2). The relation between this distance and the angle θ is given by:

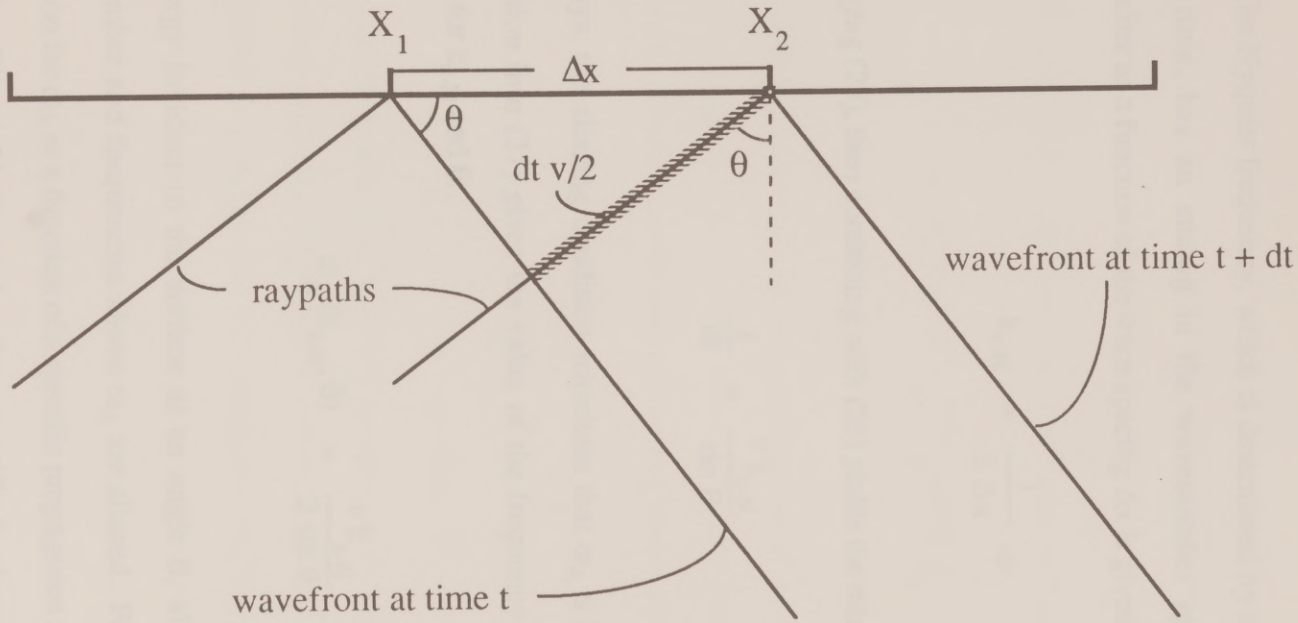

Figure 52. An up-coming wavefront in x-z space. For a constant velocity medium, θ is both the angle of incidence of the wavefront at the surface, and the dip of the structure from which the wavefront was reflected. The delay between the time the wavefront reaches receiver X_1 and receiver X_2 is given by dt.

$$\sin \theta = \frac{v\, dt}{2\, \Delta x} \quad . \tag{25}$$

The Nyquist frequency, which is determined by the sampling interval of the data in time, has an analog in the wavenumber spectrum. The maximum wavenumber as a function of the trace spacing Δx is given by

$$k_{x\text{-}N} = \frac{1}{2\, \Delta x} \quad . \tag{26}$$

Rearranging (25), then combining with (26) yields the relation

$$\frac{1}{dt} = \frac{v\, k_{x\text{-}N}}{\sin \theta} \quad . \tag{27}$$

As always, the aliasing condition stipulates that $\omega_A \leq 1 / (2\, dt)$. Introducing this information into (27) gives the value of the frequency at the threshold of spatial aliasing for $k_{x\text{-}N}$ and θ:

$$\omega_A\, (k_{x\text{-}N}, \theta) = \frac{v\, k_{x\text{-}N}}{2 \sin \theta} \quad . \tag{28}$$

For energy incident to the surface at an angle θ, all plane waves at Nyquist wavenumber and frequencies above ω_A are aliased. For convenience, I desire an expression for ω_A as a function of a specific propagation angle and any wavenumber. Reviewing Figure 51 shows that for a specific θ, aliased k_x-ω pairs form a line of

constant slope $[k_x/\omega]$, or alternatively, $[v/(2 \sin \theta)]$. At $k_x = 0$, the aliased frequency from a reflector with dip θ is given by

$$\omega_A (0, \theta) = \frac{v\, k_{x\text{-}N}}{\sin \theta} \quad . \tag{29}$$

From (28) and (29) the expression for an arbitrary wavenumber, $0 \leq k_x \leq k_{x\text{-}N}$, is

$$\omega_A (k_x, \theta) = \frac{v}{2 \sin \theta} (2\, k_{x\text{-}N} - k_x) \quad . \tag{30}$$

Although I derived (30) by consideration of a constant-velocity medium, it can also be applied to a medium whose velocity varies with depth. This is a consequence of Snell's law for laterally homogeneous layers, which can be written

$$\frac{2 \sin \theta_1}{v(z_1)} = \frac{2 \sin \theta_2}{v(z_2)} \quad . \tag{31}$$

The ratio which is conserved in (31) is the horizontal ray parameter of the wavefront. For a medium with a laterally variable velocity field, horizontal ray parameters are not constant during propagation, so spatial aliasing becomes a more complicated phenomena. Although I am presently concerned with a region which contains significant lateral velocity variations, I have avoided consideration of these variations. In the context of exploration seismology, it is usually reasonable to

assume a velocity function that only varies with depth, because velocity gradients are typically much more severe in the vertical direction.

To apply (30) to stacked seismic data, it is necessary to survey the data and determine the maximum horizontal ray parameter at which aliased energy presents a significant problem. This threshold ray parameter will be referred to as p_A, the ray parameter that defines the spatial filter. At each wavenumber, filtering can be applied to remove all frequencies higher than $\omega_A(k_x,p_A)$. This spatial filtering will remove some high frequency contributions from all reflectors in the data, including reflectors returning lower ray parameters than p_A (i.e., the filtering will remove some unaliased high frequencies from events with low dips). For this reason, it is advisable to avoid choosing an arbitrarily high value of p_A as the filter parameter. It is usually necessary to allow some aliased energy to remain in the data to insure a broad frequency band for imaging events with low dips.

The subjective nature of spatial alias filtering makes it desirable to apply filtering as a post-migration process. By doing this, the image enhancement qualities of various filters can be examined without remigrating the data at each iteration. Unfortunately, unless the data are migrated with a constant velocity, there is no simple relation between the stacked data and the migrated image. However, a constant velocity approximation can be used to attain the desired results.

Stolt (1978) demonstrated that constant velocity migration can be executed by a direct, nonrecursive mapping from k_x-ω space to k_x-k_z space by the following operation:

$$\tilde{\Psi}\,(k_x,\, z{=}0,\, \omega) \;\rightarrow\; \tilde{I}\left(k_x,\, k_z = \sqrt{4\,\omega^2 / v^2 \;-\; k_x^2}\,\right) \quad . \tag{32}$$

Using the explicit mapping relation in (32), equation (30) can be modified for k_x-k_z space to obtain

$$k_{z\text{-}A}\,(k_x,\, \theta_A) \;=\; \sqrt{\frac{1}{\sin^2\theta_A}\left(2\,k_{x\text{-}N} \;-\; k_x\right)^2 \;-\; k_x^2} \quad , \tag{33}$$

where θ_A is the threshold aliasing angle.

Equation (33) is only equivalent to (30) for data migrated using a constant velocity. Under this condition, the dispersion relation guarantees that the temporal frequency content of the stacked data is preserved by the velocity-scaled magnitude of the spatial wavenumber:

$$\omega \;=\; \frac{v}{2}\,\sqrt{k_x^2 + k_z^2} \quad . \tag{34}$$

In practice, Stolt migration is sometimes applied after stretching stacked data so that they approximate the response of a constant-velocity earth. In similar fashion, before applying equation (33) to migrated data, the data must be stretched so that they approximate the output of a constant-velocity migration. For convenience, I chose the inverse of the migration velocities as the stretching function, which is equivalent to stretching the depth section to vertical two-way travel time. After application of spatial filters, the data were then stretched back to depth. For 3-D migrated data, it

was necessary to apply spatial filtering in both the along-line and cross-line directions.

The spatial filters applied in Figures 30 and 31 used threshold dips of 0.50 sec/km and 0.70 sec/km, respectively. The filter was applied using a 10 Hz taper centered around each ω_A. All split step migration examples in this thesis following Figure 31 were displayed after application of 0.50 sec/km spatial filters.

BIBLIOGRAPHY

Berkhout, A. J., 1981, "Wave field extrapolation techniques in seismic migration, a tutorial," Geophysics, v. 46, p. 1638-1656.

Berkhout, A. J., 1984, Handbook of Geophysical Exploration, Section 1: Seismic Exploration, Vol. 12: Seismic Resolution, Geophysical Press, London, 228 p.

Bourgois, J., Azema, J., Baumgartner, P. O., Tournon, J., Desmet, A., and Aubouin, J., 1984, "The geologic history of the Caribbean-Cocos plate boundary with special reference to the Nicoya ophiolite complex (Costa Rica) and D.S.D.P. results (legs 67 and 84 off Guatemala): a synthesis," Tectonophysics, v. 108, p. 1-32.

Bracewell, 1976, The Fourier Transform and Its Applications, McGraw-Hill Book Company, U.S.A., 474 p.

Claerbout, J. F., 1970, "Course grid calculations of waves in inhomogeneous media with application to delineation of complicated seismic structure," Geophysics, v. 35, p. 407-418.

Claerbout, J. F., 1976, Fumdamentals of Geophysical Data Processing, McGraw-Hill Book Co., Inc., New York, 254 p.

Claerbout, J. F., 1985, Imaging the Earth's Interior, Blackwell Scientific Publications, Oxford, 398 p.

Coltrin, D. G. Jr., Backus, M., Shipley, T. H., Cloos, M., 1989, "Seismic reflection imaging problems resulting from a rough surface at the top of the accretionary prism at convergent margins," Journal of Geophysical Research, v. 94, p. 17,485-17,496.

Crowe, J. C., and Buffler, R. T., 1983, "Regional seismic reflection profiles across the Middle America Trench and convergent margin of Costa Rica," Seismic Expression of Structural Styles - A Picture and Work Atlas, vol. 3, ed. by A. W. Bally, AAPG Studies in Geology, Tulsa, OK, p. 3.4.2-147.

Dobrin, M. B., and Savit, C. H., 1988, Introduction to Geophysical Prospecting (4th ed.), McGraw-Hill Book Company, New York, 867 p.

Faye, J.-P., and Jeannot, J.-P., 1986, "Prestack migration velocities from focusing depth analysis," Expanded Abstracts of the Technical Program, 56th Annual International SEG Meeting, Houston, p. 438-440.

Gazdag, J., 1978, "Wave equation migration with the phase-shift method," Geophysics, v. 43, p. 1342-1351.

Hatton L., Larner, K., and Gibson, B. S., 1981, "Migration of seismic data from inhomogeneous media," Geophysics, v. 46, p. 751-767.

Hatton, L., Worthington, M. H., and Makin, J., 1986, Seismic Data Processing, Blackwell Scientific Publications, Oxford, 177 p.

Hubral, P., 1977, "Time migration: Some ray theoretical aspects," Geophysical Prospecting, v. 25, p. 738-745.

Hubral, P., and Krey, T., 1980, Interval Velocities from Seismic Reflection Time Measurements, Society of Exploration Geophysicists, Tulsa, OK, 203 p.

Jakubowicz, H., and Levin, S., 1983, "A simple exact method of 3-D migration-theory," Geophysical Prospecting, v. 31, p. 34-56.

Jain, S., and Wren, A. E., 1980, "Migration before stack - procedure and significance," Geophysics, v. 45, p. 204-212.

Jubinski, P., 1985, "A test of the accuracy of a magnetic compass-based streamer location system," Twelveth Annual Offshore Technology Conference, Houston, p. 329-336.

Krebs, J. R., 1990, "Three-dimensional migration of swath surveys," Geophysics, v. 55, no. 9, p. 1251-1259.

Larner, K. and Beasley, C., 1987, "Cascaded migrations: Improving the accuracy of finite difference migration," Geophysics, v. 52, p. 618-643.

Larner, K., Hatton, L., Gibson, B., and Hsu, I., 1981, "Depth migration of imaged time sections," Geophysics, v. 46, p. 734-750.

Larner, K. and Hatton, L., 1977, "Abstract: Wave equation migration - two approaches," Geophysics, v. 42, p. 164-165.

Levin, Franklyn K., 1971, "Apparent velocity from dipping interface reflections," Geophysics, v. 36, no. 3, p. 510-516.

Levin, Franklyn K., 1983, "The effects of streamer feathering on stacking," Geophysics, v. 48, no. 9, p. 1165-1171.

Ligon, J. M., 1985, "NAVSTAR-GPS at-sea results," Marine Geodesy, v. 9, no. 2, p. 227-261.

Lowenthal, D., Lu, L., Robertson, R., and Sherwood, J., 1976, "The wave equation applied to migration," Geophysical Prospecting, v. 24, p. 380-399.

Moore, G. F., and Shipley, T. H., 1988, "Mechanisms of sediment accretion in the Middle American Trench off Mexico," Journal of Geophysical Research, v. 93, p. 8911-8927.

Moore, G. F., Shipley, T. H., Stoffa, P. L., Karig, D. E., Taira, A., Kuramoto, S., Tokuyama, H., and Suyehiro, K., 1990, "Structure of the Nankai Trough accretionary zone from multichannel seismic reflection data," Journal of Geophysical Research, v. 95, p. 8753-8765.

Moore, J. C., Orange, D., and Kulm, L. V. D., 1990, "Interrelationship of fluid venting and structural evolution: *Alvin* observations from the frontal accretionary prism, Oregon," Journal of Geophysical Research, v. 95, p. 8795-8808.

Parks, G., and Hatton, L., 1987, "Towards a systematic understanding of the effects of velocity model errors on depth and time migration of seismic data," First Break, v. 5, no. 4, p. 121-132.

Sattlegger, J. W., 1975, "Migration velocity determination: part I. philosophy," Geophysics, v. 40, no. 1, p. 1-5.

Shipley, T. H., and Buffler, R. T., 1987, "Continental margin of Costa Rica," Seismic Images of Modern Convergent Margin Tectonic Structure, ed. by R. von Huene, AAPG, p. 33-36.

Shipley, T. H., and Moore, G. F., 1986, "Sediment accretion, subduction, and dewatering at the base of the trench slope off Costa Rica: a seismic reflection view of the décollement," Journal of Geophysical Research, v. 91, p. 2019-2028.

Shipley, T. H., Houston, M. H., Buffler, R. T., Shaub, F. J., McMillen, K. J., Ladd, J. W., and Worzel, J. L., 1979, American Association of Petroleum Geological Bulletin v. 63, p. 2204-2213.

Shipley, T. H., Stoffa, P. L., and Dean, D. L., 1990, "Underthrust sediments, fluid migration paths, and mud volcanoes associated with the accretionary wedge off Costa Rica: Middle American Trench," Journal of Geophysical Research, v. 95, p. 8743-8752.

Silver E. A., Ellis, M. J., Breen, N. A., and Shipley, T. H., 1985, "Comments on the growth of accretionary wedges," Geology, v. 13, p. 6-9.

Sil'vestrov, S. D., Nevol'ko, M. P., and Kul'nev, V. V., 1986, "Methods for increasing the accuracy of user navigational determinations in the operation of differential global positioning systems," Cosmic Research, v. 24, no. 6, p. 643-653.

Stoffa, P. L., Fokkema, J. T., Freire, R. M. d. L., and Kessinger, W. P., 1990, "Split-step Fourier migration," Geophysics, v. 55, p. 410-421.

Stoffa, P. L., Shipley, T. H., Dean, D., Kessinger, W., Elde, R., Silver, E., and Reed, D., 1991a, "Three-dimensional seismic imaging of the Costa Rica accretionary wedge: field program and migration examples," Journal of Geophysical Research, submitted March 1991.

Stoffa, P. L., Wood, W. T., Shipley, T. H., Moore, G. F., Nishiyama, E., Botelho, M. A. B., Taira, A., Tokuyama, H., and Suyehiro, K., 1991b, "Deep water and high resolution expanding spread and split-spread marine seismic profiles in the Nankai Trough," Journal of Geophysical Research, submitted February 1991.

Stolt, R. H., 1978, "Migration by Fourier transform," Geophysics, v. 43, p. 255-267.

Stolt, R. H., and Benson, A. K., 1986, Seismic Migration: Theory and Practice, Geophysical Press Limited, London, 382 p.

von Huene, R., Aubouin, J., et al., 1980, "Leg 67: The deep sea drilling project Mid-America Trench transect of Guatemala," Geological Society of America Bulletin, v. 91, p. 421-432.

Waters, K. H., 1987, Reflection Seismology: A Tool for Energy Resource Exploration, John Wiley and Sons, New York, 538 p.

Westbrook, G. K., Ladd, J. W., Buhl, P., Bangs, N., and Tiley, G. J., 1988, "Cross section of an accretionary wedge: Barbados Ridge complex," Geology, v. 16, p. 631-635.

Yilmaz, Ö., 1987, Seismic Data Processing, Society of Exploration Geophysicists, Tulsa, OK, 526 p.

Yilmaz, Ö., and Claerbout, J. F., 1980, "Prestack partial migration," Geophysics, vol. 45, no. 12, p. 1753-1779.

The vita has been removed from the digitized version of this document.